Electromagnetic exploration inputs for the geotechnical schematization of dikes

Important note
To cite this publication, please use the final published version (if applicable).
Please check the document version above.

Electromagnetic exploration inputs for the geotechnical schematization of dikes

ELECTROMAGNETIC EXPLORATION INPUTS FOR THE GEOTECHNICAL SCHEMATIZATION OF DIKES

Proefschrift

ter verkrijging van de graad van doctor
aan de Technische Universiteit Delft,
op gezag van de Rector Magnificus prof. dr. ir. T.H.J.J. van der Hagen,
voorzitter van het College voor Promoties,
in het openbaar te verdedigen op maandag 22 januari 2024 om 10:00 uur

door

Juan CHAVEZ OLALLA

Master of Science in Civil Engineering, Technische Universiteit Delft, Nederland,
geboren te Quito, Ecuador.

Dit proefschrift is goedgekeurd door de promotors

promotor: Prof. dr. ir. T.J. Heimovaara
promotor: Dr. R. Ghose
copromotor: Dr. ir. D.J.M. Ngan-Tillard

Samenstelling promotiecommissie:

Rector Magnificus,	voorzitter
Prof. dr. ir. T.J. Heimovaara,	Technische Universiteit Delft
Dr. R. Ghose,	Technische Universiteit Delft
Dr. ir. D.J.M. Ngan-Tillard,	Technische Universiteit Delft

Onafhankelijke leden:

Prof. dr. F. Wellmann	RWTH Aaachen University, Duitsland
Prof. dr. H. Middelkoop	Universiteit Utrecht
Prof. dr. ir. E.C. Slob	Technische Universiteit Delft
Prof. dr. ir. M. Kok	Technische Universiteit Delft
Prof. dr. ir. C. Jommi,	Technische Universiteit Delft, reservelid

To my mother,
Ligia Carmita Olalla

CONTENTS

SUMMARY

Low-lying coastal and delta areas, such as the Netherlands, are increasingly susceptible to flooding due to climate change. As part of the adaptation measures to climate change, countries have to reinforce their water defenses. That is a challenging and expensive endeavor that requires efficient allocation of resources. The highly variable nature of the subsurface is a large source of uncertainty when determining reinforcement measures. This thesis applies electromagnetic exploration methods to reduce subsurface uncertainties in water defenses.

Within the myriad of electromagnetic methods available, this research focuses on magnetic-dipole electromagnetic induction (EMI) and direct-current electrical resistivity tomography (ERT). These methods were selected because their response is sensitive to the electrical resistivity of the subsurface, which correlates with other geotechnical properties. Moreover, these exploration methods are easily deployable and can cover large survey areas in a relatively small amount of time. Chapter 2 delves into the theoretical aspects of EM data acquisition in dikes, investigating the sensitivity of EM devices to capture subsurface features that are relevant for dike safety. It was shown that EMI devices with far-offset receivers can capture large-scale anomalies to a similar extent than ERT with the advantage of being orders of magnitude faster. Given the relatively short range of values of electrical resistivity in a dike setting, both EM methods perform poorly in the detection of small-scale adverse features, such as thin layers. Also, the salinity of the groundwater reduces the performance of EM methods to map subsurface heterogeneity.

In Chapter 3, a method is proposed to estimate the geometric variability of soil layers with the aid of geophysical tomograms. The geometry of soil layers is important in the analysis of macrostability and internal erosion of dikes. However, soil layer geometry can change locally at a scale smaller than conventional sampling intervals. Therefore, local changes can go undetected in the site investigation of water defenses. EMI and ERT tomograms were used to estimate the orientations of soil layers, which in combination with hard data from boreholes or cone penetration tests, allowed an accurate estimation of geometric variability with a reduced exploration effort. The method proposed in this thesis was applied to estimate the thickness of blanket layers in dikes. However, the applicability of the proposed technique is not limited to water defenses. Another possible application is the detection of bed-rock interface for foundation design. A common problem that limits the wide application of geophysical methods is the need for expert knowledge for the interpretation of geophysical images. By applying automated detection techniques, which are objective and reproducible, this limitation is overcome.

Chapter 4 demonstrates the value of high-resolution ERT in estimating spatial vari-

ability of properties within homogeneous soil units. Estimating internal variability is key in geotechnical analysis of not only water defenses, but of geotechnical infrastructure in general. The failure of geotechnical structures is directly related to the weakest strength path which is directly related to the internal correlation structure. Estimating internal variability with conventional site investigation methods is expensive, intrusive, and susceptible to measurement errors, i.e. nugget effect. Chapter 4 shows that high-resolution ERT can be an efficient alternative method to estimate spatial variability. The basic condition to such estimation is the existence of a relationship between geophysical and geotechnical properties at the point-scale. Chapter 4 shows how the point-scale relationship can be efficiently derived with common geotechnical site investigation data. Finally, a practical "rule of thumb" is proposed for designing the acquisition of ERT data in relation to the target correlation length.

An important contribution of this thesis is the proposal of quantitative and reproducible methods for characterizing subsurface heterogeneity in the context of water defenses. These insights are instrumental in reducing uncertainties and optimizing resource allocation for dike reinforcement. The integration of geophysical methods with other geotechnical site data enriches the understanding of the subsurface. Chapter 5 summarizes the main findings of this research in relation to the geotechnical schematization of dikes.

SAMENVATTING

Laaggelegen kust- en deltagebieden, zoals Nederland, worden steeds vatbaarder voor overstromingen als gevolg van klimaatverandering. Om dit tegen te gaan is het nodig dat landen hun waterkeringen versterken. Dit is een uitdagende en kostbare onderneming die een efficiënte toewijzing van middelen vereist. Bij de bepaling van de benodigde maatregelen per waterkering is de ondergrond een grote bron van onzekerheid. In deze scriptie worden elektromagnetische (EM) verkenningstechnieken toegepast om meer kennis over de ondergrond te vergaren en dus de onzekerheden met betrekking tot de ondergrond van de waterkeringen te verminderen.

Meerdere elektromagnetische verkenningstechnieken zijn mogelijk om de ondergrond te onderzoeken. Dit onderzoek focust op twee hiervan: magnetische-dipool elektromagnetische inductie (EMI) en gelijkstroom elektrische weerstandstomografie (ERT). Deze methoden zijn gekozen omdat ze gebaseerd zijn op de elektrische weerstand van de ondergrond, wat correleert met andere geotechnische eigenschappen. Bovendien zijn deze verkenningstechnieken eenvoudig inzetbaar en kunnen ze in relatief korte tijd grote onderzoeksgebieden bestrijken. Hoofdstuk 2 gaat in op de theoretische aspecten van EM-gegevensverzameling in dijken, waarbij de nauwkeurigheid van de EM-apparaten voor het bepalen van de relevante, ondergrondse kenmerken wordt onderzocht. Hier wordt aangetoond dat EMI-apparaten met een relatief grote afstand tot de ontvangers grootschalige afwijkingen in vergelijkbare mate kunnen vastleggen als dat mogelijk is met ERT. Het voordeel hierbij is dat de EMI velen malen sneller is dan de ERT maar dus wel een vergelijkbaar resultaat geeft. Gezien het relatief beperkte bereik van elektrische weerstandswaarden in een dijkomgeving presteren beide EM-methoden slecht bij de detectie van kleinschalige, ongunstige kenmerken, zoals bijvoorbeeld dunne lagen. Voor kustgebieden speelt ook dat het zoutgehalte van het grondwater voor verstoring zorgt en dus de toepasbare diepte van de methodes beperkt.

In hoofdstuk 3 wordt een methode voorgesteld om de geometrische variabiliteit van bodemlagen te schatten met behulp van geofysische tomogrammen. De geometrie van bodemlagen is belangrijk bij de analyse van macrostabiliteit en interne erosie van dijken. De geometrie van bodemlagen kan over korte afstanden significant veranderen, hierdoor is doorlopende informatie over de lengteas van de dijk extra waardevol omdat deze afwijkingen tussen conventionele boringen of sonderingen kan identificeren. EMI- en ERT-tomogrammen worden gebruikt om de oriëntaties van de bodemlagen te schatten. Met de harde gegevens uit boringen of sonderingen levert dit een nauwkeurige schatting van geometrische variabiliteit. Door het combineren met EMI- of ERT-tomogrammen kan het aantal benodigde sonderingen en boringen omlaag, waardoor dit dus een besparing van conventioneel grondonderzoek oplevert. De in deze scriptie voorgestelde methoden worden toegepast om de dikte van afdeklagen in dijken te schatten. De toe-

pasbaarheid van de voorgestelde techniek is echter niet beperkt tot waterkeringen. Een andere mogelijke toepassing is het detecteren van de top van lagen sterk genoeg om op te funderen. Een beperking van geofysische methoden, is de behoefte aan expertkennis voor de interpretatie van de geofysische beelden. Door geautomatiseerde detectietechnieken toe te passen, die objectief en reproduceerbaar zijn, worden deze methoden breder inzetbaar.

Hoofdstuk 4 toont de waarde aan van hoge resolutie ERT-gegevens bij het schatten van de ruimtelijke variabiliteit van eigenschappen binnen homogene bodemeenheden. Het schatten van interne variabiliteit is essentieel in de geotechnische analyse van niet alleen waterkeringen, maar van geotechnische infrastructuur in het algemeen. Het falen van geotechnische structuren staat rechtstreeks in verband met het zwakste sterktepad, dat op zijn beurt verband houdt met de interne correlatiestructuur. Het bepalen van interne variabiliteit met conventionele terreinonderzoekmethoden is kostbaar, indringend en vatbaar voor meetfouten, zoals het nugget-effect. Hoofdstuk 4 toont aan dat hoogwaardige ERT een efficiënt alternatief kan zijn om ruimtelijke variabiliteit te bepalen. De basisvoorwaarde hiervoor is het bestaan van een relatie tussen geofysische en geotechnische eigenschappen op puntenschaal. Hoofdstuk 4 laat zien hoe de puntenschaalrelatie efficiënt kan worden afgeleid met gangbare geotechnische terreinonderzoeksgegevens. Ten slotte wordt een praktische "vuistregel" voorgesteld voor het ontwerpen van de verwerving van ERT-gegevens in relatie tot de beoogde correlatielengte.

Een belangrijke uitkomst van deze scriptie is het voorstel van kwantitatieve en reproduceerbare methoden voor het karakteriseren van ondergrondse heterogeniteit bij waterkeringen. Deze inzichten zijn essentieel om onzekerheden te verminderen en dus een passende dijkversterking te kunnen ontwerpen die niet nodeloos conservatief is. De integratie van geofysische methoden met andere geotechnische terreingegevens verrijkt het begrip van de ondergrond. In hoofdstuk 5 zijn de belangrijkste bevindingen van dit onderzoek met betrekking tot de geotechnische schematisering van dijken weergegeven.

1

INTRODUCTION

1

1.1. INTRODUCTION

Climate change has increased the risk of social and economic losses in low-lying coastal and delta areas (IPCC, 2014). Although global agreements have been made to counteract the anthropogenic interference on climate (UNFCCC, 1997, 2015), countries need to implement adaptation measures to climate-proof their territories and thus protect the welfare of their citizens. The Netherlands is particularly susceptible to the effects of climate change, with approximately 60 percent of its territory at risk of flooding (Rijkswaterstaat, 2015). In response, the Delta Committee was commissioned to devise a long-term plan to protect the Dutch coast and the low-lying hinterland against the consequences of climate change. The Delta Committee proposed twelve recommendations to manage flood risk and ensure fresh-water supply for the short, mid, and long term (Veerman and Stive, 2008). Following the recommendations of the Delta Committee, a new safety standard for water defences has been in force since January 2017 (Jongejan, Kok, and Tanckzos, 2017).

The new standard applies a flood-risk approach as opposed to the previous standard based on the probability of exceedance. The flood-risk approach defines safety levels for dikes, i.e. maximum permissible probabilities of flooding, based on the consequences of a dike breach. Since the consequences of a dike breach vary according to the location of that breach, the flood-risk standard sets different safety levels between and within dike systems. The flood-risk standard and the guidelines for risk assessment (Water, 2017; Waal, 2018) were built on the Mapping Dutch Safety (VNK) project, which was the first nationwide flood-risk assessment of the Netherlands (Rijkswaterstaat, 2015). Dikes that do not comply with the new standard are added to the High Water Protection Program (HWBP) for strengthening. The HWBP is an alliance between the regional water authorities and the central government that aims to strengthen the dikes in the Netherlands to comply with the new flood-risk standard by 2050. This is an ambitious endeavor that requires an efficient allocation of resources. Therefore, more technical knowledge is required regarding loads, subsurface heterogeneity, and the reliability of flood defences.

The All-risk research program, which this research is part of, was conceived to expand on the existing technical knowledge of flood defences. All-risk is a collaborative initiative between five universities and over 30 diverse partners, including governmental bodies, research institutes, NGOs, and private sectors. The Dutch Research Council (NWO) sponsored the All-risk program, and its findings and methodologies are consolidated in the book "Towards Improved Flood Defences" (Kok, Arevalo, and Vos, 2022). The research in this thesis is concerned in particular with the study of subsurface heterogeneity. Among the many failure mechanisms known to affect dikes, macrostability and piping are especially sensitive to subsurface heterogeneity (Hicks and Spencer, 2010; Kanning, 2012). Subsurface heterogeneity is represented in geotechnical models of piping and macrostability through geotechnical schematizations. Schematizations are conceptual models of the subsurface to which geotechnical properties are assigned. Such schematizations carry uncertainties because of the mismatch between the scale of subsurface complexity and site investigation sampling. To illustrate, the complexity of the Holocene deposits in the Rhine-Meuse ranges from centimeters to kilometers (Hi-

jma and Cohen, 2011; Winkels et al., 2021). On the other hand, site investigation in dikes is carried out with local point data, e.g. boreholes and Cone Penetrations Tests (CPT), which are collected normally at 200-meter spacing and in exhaustive investigations at 50-meter spacing (ENW, 2012). In the end, the incompleteness of the data leads to uncertainty in geotechnical schematizations.

Innovative site investigation techniques are needed to reduce schematization uncertainties. Geophysical methods are a promising source of complementary information because they are non-invasive and map the subsurface in a horizontally-continuous manner. However, many aspects have limited geophysical methods in geotechnical practice, particularly in flood defences. One of the aspects is the plethora of geophysical methods and the expert knowledge required to use them. Another and perhaps more important aspect is related to the physical limitations of geophysical methods. Geophysical methods map the subsurface remotely, for example, with sensors located at the surface of the target. Therefore, geophysical images are approximate representations of the subsurface (Menke, 2018) as opposed to direct samples of it. In particular, geophysical tomograms smooth out the fine details of the subsurface (Day-Lewis, 2005). Consequently, the geophysical images contain large-scale features of the subsurface, i.e. the frequency content of the tomographic images is lower than that of the subsurface (Hubbard, Rubin, and Majer, 1999). A challenge in the geophysical exploration of water defences is obtaining geophysical data at the level of detail relevant for the stability analysis of dikes.

The research in this thesis is part of an effort to expand technical knowledge about water defences. This thesis aims to provide inputs for the geotechnical schematization of dikes through a subset of geophysical exploration methods, namely electromagnetic exploration. In the following sections of this chapter, an overview is given of the failure mechanisms in dikes related to subsurface heterogeneity and the specific subsurface features that have an impact on these failure mechanisms. Afterwards, an overview is given about the state of the art of the geophysical investigation of dikes. Finally, the aim and approach of this research are outlined.

1.2. FAILURE MECHANISMS RELATED TO SUBSURFACE HETEROGENEITY

The stability of dikes is susceptible to various failure mechanisms. In this research, piping and macrostability are of interest because they are sensitive to subsurface heterogeneity. Piping is a failure mechanism that occurs in impervious dikes lying on top of an aquifer (Figure 1.1). The difference in water level between the outer and inner side of the dike, H, induces groundwater flow, which under certain conditions causes erosion through a piping channel, hence the name. The eroded soil is transported to the inner side of the dike, forming a sand boil. A widely used mathematical model for piping is given by the Sellmeijer formula (Sellmeijer, 1988) which has since been fine-tuned based on experimental evidence (Sellmeijer et al., 2011). The Sellmeijer model consists of three

sub-failure mechanisms, namely uplift, heave, and piping. In uplift, the blanket breaks because the uplift force is larger than the resistance provided by the blanket weight. In heave, the hydraulic gradient over the blanket causes the outflow of sand particles into a sand boil. In piping, the hydraulic gradient over the dike forms a continuous channel that starts at the breaking point of the blanket and extends towards the outer side of the dike. Ultimately, the dike breaches due to the piping channel that formed due to internal erosion. The interplay between the geometry of the soil layers and their material properties determines the resistance of the dike against piping.

Macrostability is a failure mechanism caused by the lack of mechanical strength along a slip surface. Mathematical models for macrostability vary in complexity. For instance, in the Limit Equilibrium Method (LEM), the stability of different slip surfaces is tested as an equilibrium of forces (Bishop, 1955; Spencer, 1967; Van, Koelewijn, and Barends, 2005). The slip surface with the least stability is known as the critical slip surface and determines the stability of the dike. The shape of the slip surface varies according to the type of LEM method. For example, in the Bishop method (Bishop, 1955), the shape of the slip surface is circular. Meanwhile, in the Uplift Van method (Van, Koelewijn, and Barends, 2005), the shape of the slip surface is composed of circular and flat segments. Another approach to model macrostability is by implementing the equilibrium equations and the stress-strain constitutive relation with the Finite Element Method (FEM) (Griffiths and Lane, 1999; Smith, Griffiths, and Lee, 2014). In FEM, the failure surface is not assumed. Instead, it is the result of the analysis at failure. Regardless of the calculation method, the slip surface and, therefore, the macrostability of dikes depend on the geometric disposition of soil layers and the variability of soil properties within the layers.

Geotechnical schematizations are a central component in the stability analysis of dikes. Schematizations have to capture the complexity of the subsurface in the context of the failure mechanism under analysis, which is challenging because the subsurface is heterogeneous at different scales. Indeed, the Dutch subsurface is built up by sequences of gravely sandy aquifers alternated by confining clayey aquitards. The uppermost aquifer, which was deposited during the last glacial period (Pleistocene epoch), forms a nearly continuous sandy substrate. These deposits are overlain by the Holocene deltaic wedge which forms a heterogeneous confining layer. This layer is mostly composed of aquitard floodplain clays, clay-fine sand, dominated intertidal flats, and peats. However, it is dissected by (partly) isolated alluvial and tidal channel sand bodies (Bierkens, 1994; Weerts, 1996; Hijma and Cohen, 2011). These channel-belt sand bodies act as shallow-depth aquifers and locally occur directly underneath dikes. In addition, small-scale variability of sand bodies also occurs due to autogenic processes. Site investigation data does not capture the full complexity of the subsurface, nor is it necessary. Instead, geotechnical practitioners schematize the subsurface at the scale relevant for the stability analysis of dikes.

The Dutch subsurface has been largely investigated, and consequently, there is a large amount of information available in the form of boreholes, CPTs, geological maps, and geological models (Stafleu et al., 2011; van der Meulen et al., 2013). For flood-risk
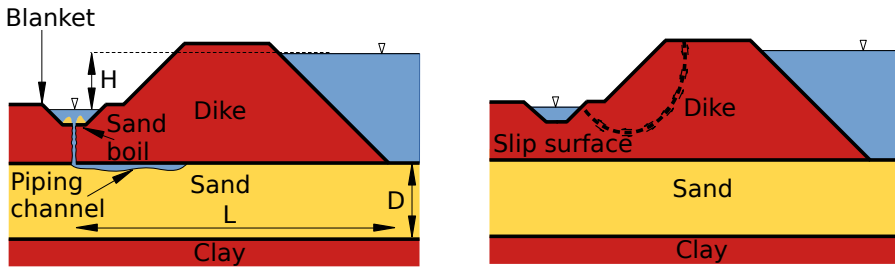
Figure 1.1: Schematic of the piping (left) and macrostability (right) failure mechanisms. In piping, the difference in ground water level, H, induces groundwater flow, which under certain conditions causes erosion through a piping channel. The eroded material is deposited in a sand boil. In macrostability, a mass of soil moves through a slip surface due to the lack of mechanical strength in the soil material.

calculations, that information has been interpreted by experts into a list of likely subsurface scenarios for all the primary water defences in the Netherlands, known as the WTI-SOS scenarios (Hijma and Lam, 2015). The WTI-SOS scenarios constitute the starting point for geotechnical schematizations in the Netherlands as they do not depend on the failure mechanism under analysis. The current Dutch schematization guideline (Kruse and Hijma, 2015) provides a systematic approach to schematize the subsurface for geotechnical calculations. The guideline refines the WTI-SOS scenarios by incorporating local site investigation data and failure mechanisms. Since the relevance of a geological scenario or subsoil layer depends on the failure mechanism under analysis, a list of typical subsurface features relevant for the stability analysis of dikes is summarized in Figure 1.2. Table 1.1 elaborates on the manner the subsurface features in Figure 1.2 are relevant for piping and macrostability. The challenge is to determine the existence, dimensions, and variability (vertical and horizontal) of such subsurface features.

1.3. GEOPHYSICAL METHODS AND HETEROGENEITY

Conventional site investigation methods, i.e. CPTs and borehole drillings, sample the subsurface in detail, yet locally. CPT samples are normally collected at a spacing of 200 m along the main dimension of dikes (ENW, 2012). Meanwhile, piping and macrostability are sensitive to subsurface features smaller than that sampling interval (Kruse and Hijma, 2015). Even short sampling intervals can fail to detect relevant subsurface features. For instance, when the horizontal boundary of a sand body intersects with a dike, isolated sand bodies smaller than 25 m often occur, which can have an important effect on the stability of a dike (Kruse and Hijma, 2015). The mismatch between site investigation density and actual subsurface variability leads to schematization uncertainties. To illustrate, the probability of detecting a soil layer of horizontal size b with a CPT interval d is b/d. Thus, the probability of detecting a 25 m feature with a 50, 100, and 200 m sampling interval is 50, 25, and 12.5 percent, respectively. Therefore, important subsurface features are easily missed with conventional site investigation. Moreover, measuring the internal variability of soil units requires an unpractical number of CPTs (Gast, Vardon,

1
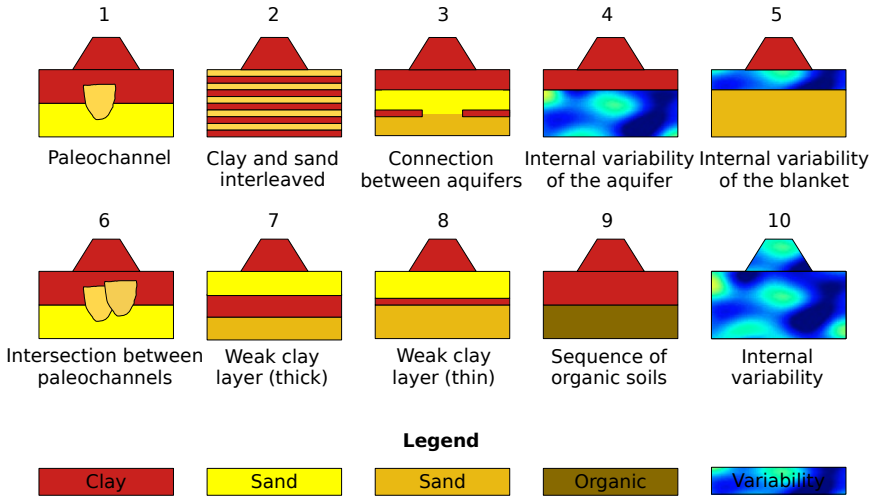
Figure 1.2: Typical subsurface scenarios relevant for the stability analysis of dikes.

and Hicks, 2021). Although schematization uncertainties are compensated with safety factors in geotechnical practice (ENW, 2012), large uncertainties result in uneconomical designs or unnecessary reinforcement of existing structures. Therefore, it is paramount to reduce these uncertainties without intrusively sampling the subsurface. For this purpose, geophysical methods are a promising option because they map the subsurface in a horizontally-continuous manner.

Geophysical methods have been widely used for the investigation of dikes with varied success Dezert et al. (2019). In the past decade, the extensive list of case studies reported in the literature has been summarized in guidelines for geotechnical practitioners (Fauchard and Mériaux, 2007; Royet et al., 2013; Hickey et al., 2015). Comparisons of geophysical methods for dike inspection have also been reported in the literature. For instance, Niederleithinger, Weller, and Lewis (2012) evaluated resistivity, electromagnetic, seismic, and ground radar methods in search of sand bodies, such as case 1, 2, and 6 in Figure 1.2. A similar comparison of geophysical methods was carried out by Inazaki (2007). Both studies reported similar findings. The overarching conclusion of these studies is that resistivity methods, such as Electrical Resistivity Tomography (ERT) are the most cost-effective for detecting anomalies, especially sand bodies. Other methods, such as Multiple Amplitude Surface Waves (MASW), show a good visual correlation with geological data, but fail to demarcate anomalies. Although geophysical data offer a new perspective on subsurface variability, it is clear from these studies, that most geophysical applications in dikes have been qualitative. That is, experts visually interpret the geophysical images together with other site investigation data.

Even though geophysics has been used largely in flood defences, there are no studies in the literature that focus on the quantitative interpretation of geophysical data for dike

	Subsurface scenario	Effect on failure mechanism
1	Paleochannel	P: Thickness reduction of the blanket layer P: Changes in grain size and hydraulic conductivity M: Uplift due to pore-water pressure
2	Clay and sand interleaved	P: Thickness reduction of the blanket layer P: Changes in grain size and hydraulic conductivity M: Uplift due to pore-water pressure
3	Connection between aquifers	P: Increment in aquifer depth
4	Internal variability of the aquifer	P: Erosion through locally weak sand
5	Internal variability of the cover layer	P: Reduced resistance to uplift
6	Paleochannel intersection	P: Thickness reduction of the blanket layer P: Changes in grain size and hydraulic conductivity M: Uplift due to pore-water pressure
7	Weak clay layer (thick)	M: Slip surface through weak layer
8	Weak clay layer (thin)	M: Slip surface through weak layer
9	Sequence of organic soils	M: Slip surface through the boundary
10	Internal variability of dike and subsurface	M: Local failure through weak regions

Table 1.1: Common geological features relevant for the geotechnical analysis of dikes. P and M stand for piping and macrostability, respectively.

investigation. However, this is crucial to make geophysical data more accessible and reproducible for geotechnical practitioners. Moreover, a quantitative interpretation would make explicit which part of the geophysical data is interpreted as geotechnical data and which part as noise. Niederleithinger (2015) evaluates the possibility of using geostatistics to interpret geophysical data, an approach which is commonly used in hydrogeophysics (Binley et al., 2015). Geostatistics requires formulating quantitative relationships between the target geotechnical property and the physical property of the geophysical survey. The relationships are, in most cases, empirical and site-specific. In the past, these relationships were derived from laboratory experiments, making them expensive and impractical for investigating dikes. The current development of site probing methods, such as seismic and electric CPTs, allows for a quick and site-specific formulation of empirical relationships. This opens the range of possibilities in terms of quantitative interpretation of geophysical data.
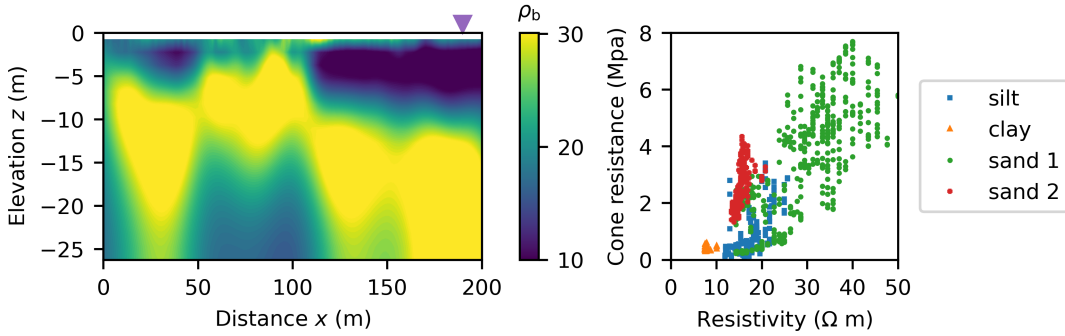
Figure 1.3: Typical geotechnical and geophysical data of a dike. An ERT tomogram is shown on the left. A scatter plot of the cone resistance versus the electrical resistivity is shown on the right. The scatter plot contains data of an electric CPT located at a distance of 190 m (inverted triangle in the left figure).

To elaborate on this idea, consider the real ERT tomogram of Figure 1.3 (left) and the electric CPT of the same site. Figure 1.3 (right) shows a scatter plot of the cone resistance versus the electrical resistivity measured with the electric CPT. Both the ERT tomogram and the CPT scatter plot reveal the presence of four distinct soil layers. The visual interpretation of soil layers from geophysical tomograms relies on an implicit assumption: a correlation exists between the geotechnical and geophysical properties. For example, the higher the sand content, the higher the electrical resistivity and cone resistance. Therefore, a CPT or an ERT tomogram can be used to identify soil layers. In the case of Figure 1.3, this assumption is quantitatively confirmed by the linear relationship observed between cone resistance and electric resistivity for the different soil layers. Looking further to the scatter plot, the data form four clusters, corresponding to the four layers present in the CPT. In this case, the electrical resistivity of the silty and clayey layers overlap in the scatter plot, but they are separated in physical space by the sandy layer. Therefore, the three soil layers are identifiable. Had it not been the case, these layers would not be discernible from each other even though they are different in terms of geotechnical properties. The resistivity variance and correlation within the clusters of Figure 1.3 suggest that geophysical exploration could be also used for the characterization of internal variability of the soil layers. Then, a relationship needs to be derived from the scatter plot for each cluster.

1.4. Motivation
Traditional site investigation methods capture the horizontal variability of the subsurface often insufficiently. The mismatch between subsurface variability and sampling results in schematization uncertainties for the stability analysis of dikes. Geophysical methods are a promising source of complementary information because they map the subsurface horizontally-continuously. Among the myriad of geophysical methods available for engineering applications, EM methods, including ERT, are the most popular due

to their easy deployability. Nevertheless, the literature is unclear regarding the performance of EM methods to map common subsurface features relevant for the geotechnical assessment of dikes. Also, the literature is unclear as to how to derive quantitative insights for the geotechnical schematization of dikes from geophysical data.

1.5. Main aim

The aim of this research is to contribute to the geotechnical assessment of dikes by giving geophysical inputs in their geotechnical schematization. Ultimately, better schematization will contribute to the optimal allocation of resources to climate-proof flood-prone territories. This thesis has two objectives:

- To assess the performance of EM exploration methods to map heterogeneity in dikes and their substrate

- To improve the interpretation and incorporation of geophysical images in geotechnical schematizations for safety assessments

The research in this thesis is carried out by combining synthetic and field studies.

1.6. Outline

The subsequent chapters address two main research questions:

- How does the effectiveness of electromagnetic methods compare when used to detect both geological architecture underneath dikes and man-made internal structure within dikes? (Chapter 2)

- How do electromagnetic methods impact the quantitative characterization of geological features, that is, geometry (Chapter 3), and internal variability (Chapter 4)

Two electromagnetic methods are compared, namely magnetic-dipole Electromagnetic Induction (EMI), and direct-current Electrical Resistivity Tomography (ERT). The methods were chosen as they are mature technologies for engineering applications.

The impact of EM methods in the quantitative characterization is assessed in terms of accuracy, and operational effort. The operational effort is defined by the reduction of invasive samples required and the accuracy of the characterization as compared to the truth defined by invasive sampling.

In Chapter 2, a synthetic evaluation of electromagnetic geophysical methods is carried out. The synthetic model is based on data derived from a real dike. Although the case study does not contain all the subsurface features of Figure 1.2, it is a realistic dike susceptible to macrostability failure. Therefore, the synthetic analysis gives insights into

1

the possibilities and limitations of electromagnetic exploration. In Chapter 3, a quantitative framework is developed for the incorporation of tomographic data to estimate the geometric variability of soil layers. In Chapter 4, a method is presented to estimate the small-scale internal variability of soil layers with geophysical tomograms. The particular case of direct-current ERT is analyzed. Finally, Chapter 5 provides a summary of the research findings and their implications for the geotechnical schematization of dikes.

2

EVALUATION OF ELECTROMAGNETIC (EM) METHODS FOR DIKE EXPLORATION

In Chapter 2, Electromagnetic (EM) methods are evaluated for the detection of geological features in a synthetic dike. The evaluated methods are direct-current injection and magnetic-dipole induction. The electromagnetic properties of the synthetic dike are derived from well-known constitutive relations. The variables considered in the evaluation are

- Material properties of the dike setting
- Design of the electromagnetic surveys
- Groundwater salinity

This chapter covers the theoretical aspects of EM data acquisition in dikes, which form the basis for subsequent discussions in this thesis. Moreover, this chapter gives an overview of the possibilities and limitations of EM methods to explore water dikes.

The contents of this chapter are in preparation to be submitted to the Journal of Environmental and Engineering Geophysics.

2.1. Introduction

Geophysical methods are a promising source of complementary information in characterizing subsurface heterogeneity for water defences. In recent years, many efforts have been aimed at developing and promoting geophysical exploration in water defences, which have been summarized in the literature as handbooks and technical reports (Fauchard and Mériaux, 2007; Royet et al., 2013; Hickey et al., 2015). Although these summaries have solid theoretical and experimental backgrounds, they lack a link to the geotechnical practice. To illustrate, Electrical Resistivity Tomography (ERT) is commonly labeled as recommended for mapping vertical layers. However, the effectiveness of ERT to detect vertical layers depends on the dimensions of the layers, depth, and resistivity contrast. The limits where such recommendations hold are not easy to determine. Although analytical solutions for ERT responses are available in the literature (Wait, 1982; Zhdanov and Keller, 1994), the complexity of the subsurface makes their application limited. Therefore, the literature is missing a description of the possibilities and limitations of geophysical methods for the exploration of dikes. This chapter builds that knowledge base with the aim of promoting the informed use of geophysical exploration technologies in the water defence sector.

Among the myriad of geophysical methods, Electromagnetic (EM) methods are often the first choice in subsurface characterization for geotechnical applications (Dezert et al., 2019). In addition to the information they provide in the horizontal direction, they are also easily deployable and therefore low-cost. Although the deployability varies from method to method, EM methods require relatively small amount of human and equipment resources to cover large areas (Binley et al., 2015). Two EM methods have proven particularly successful for geotechnical applications, namely direct-current Electrical Resistivity Tomography and magnetic-dipole Electromagnetic Induction (EMI) (Niederleithinger, Weller, and Lewis, 2012). Other EM methods have not been fully successful for several reasons. Ground Penetrating Radar (GPR) signals, for example, are attenuated in electrically conductive media which is characteristic of floodplain deposits. To illustrate, the upper-most layer of the Rhine-Meuse delta consists primarily of floodplain clays, intertidal flats, clay-fine sands, and peats (Winkels et al., 2021), which are associated to high electrical conductivity values (Weller, Slater, and Nordsiek, 2013; Revil et al., 2013). On the other hand, Induced Polarization (IP), despite of the similarity with ERT, requires a more intricate acquisition setup and longer acquisition times (Kemna et al., 2012). Thus, the low deployability of IP outweighs the possible benefits. In the end, ERT and EMI are more suitable for geotechnical applications because they are more easily deployable and less affected by site conditions.

EM methods have been evaluated for characterizing the heterogeneity of water defences with varied success. For instance, Niederleithinger, Weller, and Lewis (2012) evaluated a variety of geophysical methods for dike inspection in a test site along the Mulde river in Germany. Among the methods used in that study, ERT proved successful in finding and delineating an anomalous sand body. Meanwhile, EMI was in agreement with major changes in soil composition, but it failed to delineate the boundaries of the same anomalous sand body. Even though both EM methods are primarily sensitive to the

same property, i.e. the electrical resistivity, ERT maps subsurface heterogeneity better than EMI (Inazaki, 2007; Fauchard and Mériaux, 2007; Royet et al., 2013; Hickey et al., 2015). Due to the variety of EMI devices used in these studies, the reported performance of EMI varies considerably. Indeed, the sensitivity of EMI to subsurface heterogeneity varies according to the design of the EMI device (see Boaga (2017) for an overview of commercial EMI devices). Therefore, it is important to understand the interplay between design features of EMI devices, i.e. frequency and coil spacing, in the context of dike exploration to determine whether EMI can be a cost-effective alternative to ERT.

The performance of ERT and EMI to map heterogeneity is also affected by the material properties of the geological setting and three-dimensional effects. In non-magnetic environments and for low frequency sources, ERT and EMI are sensitive only to the bulk electrical resistivity of the subsurface, which is an aggregate of the electrical properties of the pore space (Schön, 2015). Because of the interplay between electrical properties at the pore-scale, the bulk resistivity of geologically different sediments can overlap and therefore be indiscernible. Three-dimensional effects can also be important because some EMI devices have far-offset receivers. Nevertheless, EMI data are inverted with a one-dimensional assumption (Santos, Triantafilis, and Bruzgulis, 2011). In engineering applications, EMI data are not inverted with three-dimensional forward models possibly due to the prohibitive computational cost of three-dimensional EMI simulations. To sum up, the literature has not discussed the effect of heterogeneity and far-offset receivers in the EM exploration of dikes.

A variety of factors affect the performance of EM methods in the exploration of water defences. A quantitative understanding of the effect of these factors on the EM signals and images is important to further promote the informed use of EM methods in the water defence sector. I chose to use synthetic data to analyze these factors because it is flexible and the results can be validated. Therefore, this chapter evaluates ERT and EMI for the characterization of a synthetic, though realistic, dike setting. Three points are considered in this evaluation: (1) the material properties of the dike setting, including salinity of ground water, (2) the data acquisition design of the ERT and EMI devices, and (3) three-dimensional effects.
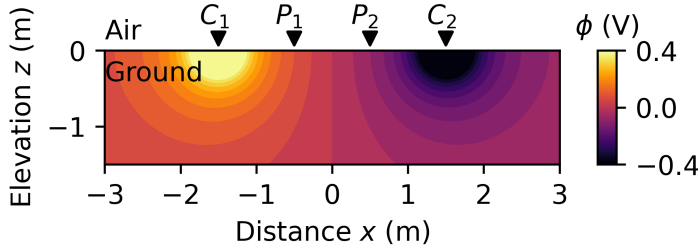
Figure 2.1: Schematic of an ERT measurement. The contours show the ground response, electric potential ϕ, of a homogeneous medium under two point sources of current of opposite polarity, C_1 and C_2. The response corresponds to an injected current $I = 1\,\text{A}$ and an homogeneous electrical resistivity $\rho = 1\,\Omega\,\text{m}$. C_1 and C_2 are current electrodes. The difference in electric potential is measured between the electrodes P_1 and P_2.

2.2. EM SIGNALS AND IMAGES

2.2.1. DIRECT-CURRENT ELECTRICAL RESISTIVITY TOMOGRAPHY (ERT)

The ERT method is based on the ground response, electric potential, to point sources of direct current. The injection and the measurement electrodes are commonly located at the surface of the medium. However, they can also be located inside the medium. In the case of metallic electrodes, the injection and measurement points are interchangeable. Thus, an electrode can be used to inject current or to measure electric potential. The ground response depends on the bulk electrical resistivity of the ground. For a point current source, the ground response is related to the bulk electrical resistivity, ρ by the equation

$$\nabla \cdot \frac{1}{\rho(x, y, z)} \nabla \phi(x, y, z) = -I\delta(x - x_\text{s})\delta(y - y_\text{s})\delta(z - z_\text{s}), \tag{2.1}$$

where ϕ is the electric potential, I is the source current, and δ is the Dirac-delta function centered at the location of the point source. Since the electrical conductivity is the inverse of the electrical resistivity $\sigma = 1/\rho$, both terms are used in this thesis to mean the same material property. Equation 2.1 represents the forward model for ERT. In reality, two sources of opposite polarity are needed to inject current into the ground. Also, two electrodes are needed to measure the electric potential difference. Thus, one ERT measurement requires four electrodes, a quadrupole. Figure 2.1 shows a schematic of the ground response in an ERT measurement. In the figure, C_1 and C_2 are current electrodes while P_1 and P_2 are potential electrodes. The total electric potential results from the algebraic sum of the electric potential for each point source. Finally, the electric potential difference between P_1 and P_2 is measured for each current injection.

An ERT measurement is represented by the apparent resistivity instead of the electric potential. The apparent resistivity is the resistivity of an equivalent homogeneous medium. In a homogeneous half-space, the ground response for a single point source is given by

$$\phi = \frac{\rho I}{2\pi r},$$

where r is the distance between the current and potential electrode. Thus, the electric potential difference between P_1 and P_2 becomes

$$\Delta\phi = \phi_1 - \phi_2 = \frac{\rho I}{2\pi}\left(\frac{1}{r_{C_1 P_1}} - \frac{1}{r_{C_2 P_1}} - \frac{1}{r_{C_1 P_2}} + \frac{1}{r_{C_2 P_2}}\right).$$

where $r_{C_i P_j}$ is the distance between injection point C_i and measuring point P_j. Thus, the apparent resistivity becomes

$$\rho_{\text{app}} = k\frac{\Delta\phi}{I}, \tag{2.2}$$

where

$$k = \frac{2\pi}{\left(\frac{1}{r_{C_1 P_1}} - \frac{1}{r_{C_2 P_1}} - \frac{1}{r_{C_1 P_2}} + \frac{1}{r_{C_2 P_2}}\right)}$$

is the geometric factor. In an ERT survey, the separation between electrodes or the array type is changed to detect different subsurface portions. Commonly used array types are dipole-dipole, Wenner-alpha, and Wenner-Schlumberger. The array type has a large influence on the sensitivity of the measurement. For example, the Wenner-alpha array is more sensitive to horizontal structures, while the dipole-dipole array is more sensitive to vertical structures (Loke, 2013). In this thesis, the python package pyBERT (Rücker, Günther, and Spitzer, 2006) was used to solve the forward model in equation 2.1.

2.2.2. MAGNETIC-DIPOLE ELECTROMAGNETIC INDUCTION (EMI)

The EMI method described in this section is based on the ground response, magnetic field, to a vertical magnetic dipole above the earth surface. The magnetic dipole is induced by a current source in the form of a coil through which alternating current flows at a given frequency. The geometric arrangement of the source and receiver coil determines the sensitivity of the signal with respect to subsurface heterogeneity. The ground response follows from the frequency-domain electromagnetic wave equation in the presence of a current source $\boldsymbol{J}_\text{s}$ (Mulder, 2006)

$$i\omega\mu_0\tilde{\sigma}(x,y,z,\omega)\hat{\boldsymbol{E}}(x,y,z,\omega) - \nabla\times\mu_\text{r}^{-1}\nabla\times\hat{\boldsymbol{E}}(x,y,z,\omega) = -i\omega\mu_0\hat{\boldsymbol{J}}_\text{s}(x,y,z,\omega) \tag{2.3}$$

where $\hat{\boldsymbol{E}}$ is the electric field, $\tilde{\sigma} = \sigma(x,y,z) - i\omega\epsilon(x,y,z,\omega)$, ω is the angular frequency of the current source, ϵ is the permittivity of the medium, μ_0 is the magnetic permeability of free space, and $\mu_\text{r} = \mu/\mu_0$ is the relative magnetic permeability of the medium. For non-magnetic materials, $\mu_\text{r} = 1$, and at low frequencies, $\omega\epsilon << \sigma$, the ground response is only a function of the bulk electrical conductivity $\tilde{\sigma}(x,y,z,\omega) = \sigma(x,y,z)$. The magnetic field $\hat{\boldsymbol{H}}$ is calculated with Faraday's law of induction in the frequency domain

$$\nabla\times\hat{\boldsymbol{E}} = i\omega\mu\hat{\boldsymbol{H}}. \tag{2.4}$$

Commercial EMI devices for engineering applications give the response as the ratio of the secondary magnetic field to the primary magnetic field H_s/H_p. The primary field is the coplanar free-space response measured at a distance s from a magnetic-dipole source of moment m

$$H_\text{p} = \frac{m}{4\pi s^3}. \tag{2.5}$$

Device	Frequency (kHz)	s_{HCP} (m)	s_{PRP} (m)	h (m)
GEM2	1-50	1.66	-	1.0
DUALEM-842	9	8.0, 4.0, 2.0	8.1 , 4.1, 2.1	0.2
DUALEM-421	9	4.0, 2.0, 1.0	4.1 , 2.1, 1.1	0.2

Table 2.1: Source-receiver configuration of the EMI devices used in this chapter.
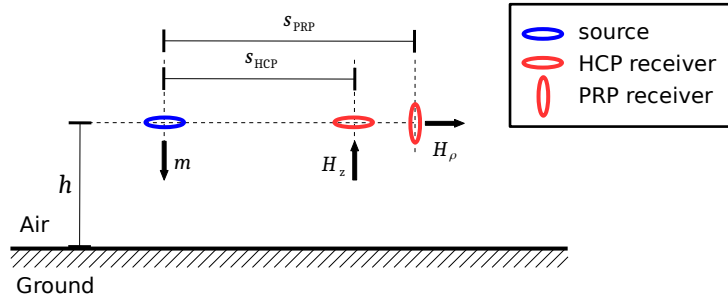

Figure 2.2: Schematic of the source-receiver configuration of magnetic-dipole EMI devices. A magnetic dipole with strength m generates an electromagnetic field. The HCP sensors detect the vertical component of the magnetic field, H_z. The PRP sensors detect the radial component of the magnetic field, H_ρ. The source and receivers are located above the ground at a distance h. The receivers are located at a distance s from the source.

Meanwhile, the secondary field is that reflected by the ground. This section considers Horizontal Coplanar (HCP) and Perpendicular (PRP) coils. The HCP receivers detect the vertical component of the magnetic field, H_z, while the PRP receivers detect the radial component of the magnetic field, H_ρ. Figure 2.2 shows a schematic of the source-receiver configuration of EMI devices. These configurations make the commercial devices analyzed in this thesis GEM2 (Huang and Won, 2000), DUALEM-421, and DUALEM-842 (Dualem Inc., Milton, ON, Canada). GEM2-like devices are considered frequency sounders because the separation between coils is constant, but the frequency can vary typically between 1 kHz and 50 kHz. DUALEM-like devices are considered geometric sounders because they have a constant frequency but many receiver coils. The source frequency of the DUALEM devices is 9 kHz, and the receivers are located at a distance of 4 m, 2 m, and 1 m for the DUALEM-421 and a distance of 8 m, 4 m, and 2 m for the DUALEM-842. Table 2.1 summarizes the source receiver-configurations of the EMI devices.

Regardless of the EMI device, solving equation 2.3 in three-dimensions is computationally expensive and becomes prohibitive for tomographic inversion. In this chapter, equation 2.3 is solved with a full three-dimensional approach (Werthmüller, Mulder, and Slob, 2019) to simulate EMI data acquisition. A one-dimensional approximation is made for tomographic inversion of EMI data. The one-dimensional approximation is based on the magnetic field showing cylindrical symmetry for a vertical magnetic dipole above a

flat ground surface and horizontal soil layers. Hence, the vertical and radial components have a semi-analytical solution. A derivation of that solution is presented in Ward and Hohmann (1988). In this section, only the solutions are presented. For the HCP receivers, the secondary field normalized with respect to the primary magnetic field (Equation 2.5) is given by

$$\frac{H_{\text{S}_{\text{HCP}}}}{H_{\text{p}}} = s_{\text{HCP}}^3 \int_0^\infty r_{\text{TE}} e^{-2\lambda h} \lambda^2 \text{J}_0(\lambda s) \text{d}\lambda. \tag{2.6}$$

For the PRP receivers, the ratio $H_{\text{s}}/H_{\text{p}}$ is given by

$$\frac{H_{\text{S}_{\text{PRP}}}}{H_{\text{p}}} = s_{PRP}^3 \int_0^\infty r_{\text{TE}} e^{-2\lambda h} \lambda^2 \text{J}_1(\lambda s) \text{d}\lambda. \tag{2.7}$$

In the above equations, r_{TE} is the transverse electric reflection coefficient, λ is the wavenumber, and J_i is the ith-order Bessel function of the first kind. The reflection coefficient,

$$r_{\text{TE}} = \frac{\lambda - \hat{u}_1}{\lambda + \hat{u}_1},$$

is a function of the wavenumber of the soil layer located at the air-ground interface, $\hat{u}_1$, which is calculated iteratively starting from the second-to-last layer ($n = N - 1$) at the bottom of the one-dimensional domain of N layers

$$k_n^2 = -\text{i}\mu_0\sigma_n\omega$$

$$u_n = \sqrt{\lambda^2 - k_n^2}$$

$$\hat{u}_n = u_n \frac{\hat{u}_{n+1} + u_n\tanh(u_n h_n)}{u_n + \hat{u}_{n+1}\tanh(u_n h_n)}$$

where h_n is the thickness of layer n, $\hat{u}_{n+1} = \sqrt{\lambda^2 - k_N^2}$ in the first iteration, and it is updated in each iteration

$$\hat{u}_{n+1} = \hat{u}_n.$$

2.2.3. TOMOGRAPHIC INVERSION

A tomogram is an approximate image of the subsurface, which is obtained through inversion (Menke, 2012). The inversion process consists in fitting the measured response of a geophysical survey, d, to the response of a forward model, f. The forward model describes the physical response of the geophysical method (Equation 2.2 for ERT and Equations 2.6 and 2.7 for EMI). The response of the forward model is a function of the spatial distribution of the geophysical property, $g(x, y, z)$, in the subsurface. Since the inversion process is described in terms of discrete variables, $g(x, y, z)$ is represented by the vector $\underline{g}$ in the following equations. The tomogram is then the spatial distribution $\underline{g}$ that minimizes the data functional

$$\Phi_{\text{d}}(\underline{g}) = (\underline{d} - f(\underline{g}))^{\text{T}}\underline{\underline{D}}^{\text{T}}\underline{\underline{D}}(\underline{d} - f(\underline{g})) \tag{2.8}$$

2

where $\underline{\underline{D}}$ is a weighting matrix that contains the correlation structure of the measurement errors. $\underline{\underline{D}}$ is often approximated as a diagonal matrix

$$\underline{\underline{D}} = \text{diag}(1/\underline{\epsilon}_d) \tag{2.9}$$

where $\underline{\epsilon}_d$ is the vector of repetition or reciprocal errors (Günther, Rücker, and Spitzer, 2006a; Friedel, 2003).

Many inverse problems in geophysics are ill-posed (Menke, 2012). A regularization term, Φ_g, is then added to the data functional Φ_d to remove ill-posedness. In this thesis, smoothness regularization is used to define the regularization term (Rücker, Günther, and Spitzer, 2006)

$$\Phi_g(\underline{g}) = (\underline{g} - \underline{g}_{\text{ref}})^{\text{T}} \underline{\underline{C}}^{\text{T}} \underline{\underline{C}} (\underline{g} - \underline{g}_{\text{ref}}) \tag{2.10}$$

where $\underline{\underline{C}}$ is a constraint matrix of first order derivative operators and $\underline{g}_{\text{ref}}$ is a reference model. In ill-posed inverse problems, a tomogram, $\bar{g}(x, y, z)$, is constructed by minimizing

$$\Phi(\bar{g}) = \Phi_d(\bar{g}) + \lambda \Phi_g(\bar{g}), \tag{2.11}$$

as opposed to Equation 2.8. The upper bar on $\bar{g}(x, y, z)$ is used to emphasize the fact that $\bar{g}$ is an approximation of the geophysical property $g(x, y, z)$. In Equation 2.11, λ is the regularization strength which defines the weight assigned to the regularization term Φ_g in the minimization process. The larger the value of λ, the smoother the tomogram. On the other hand, small values of λ lead to rough tomograms due to over fitting of the data functional Φ_d. The L-curve method (Günther, Rücker, and Spitzer, 2006a) was applied to pick optimum values for λ. The method consists in finding the point of maximum curvature of the plot Φ_d versus Φ_g. The minimization of Φ produces a tomogram, $\bar{g}(x, y, z)$, which is a smooth representation of the true spatial distribution of the geophysical property. In this case, the geophysical property $\bar{\underline{g}}$ is the electrical resistivity.

2.3. Dike model
2.3.1. Pore-scale relationships
The bulk electrical conductivity of a porous medium is an aggregate of the electrical properties of the pore fluids and the pore matrix. The bulk electrical conductivity is a complex quantity, but the conductivity that appears in Sections 2.2.1 and 2.2.2 is real-valued and represents the magnitude of the complex conductivity. Because the imaginary term of the conductivity is much smaller than the real term (Weller, Slater, and Nordsiek, 2013), I only consider the real component in this analysis. In other words, the real part of the bulk conductivity is assumed to represent the magnitude of the bulk conductivity. A widely used approach to model the real component of the complex conductivity, σ_b, is to add in parallel the conduction terms of the pore fluid and the solid matrix (Singha et al., 2015)

$$\sigma_b = \sigma_{el} + \sigma_{surf}. \tag{2.12}$$

The pore fluid component, σ_{el}, is caused by electrolytic conduction. The solid matrix component, σ_{surf}, is caused by the electromigration of charge in the electrical double layer that forms at the matrix-fluid interface, i.e. surface conduction (Weller, Slater, and Nordsiek, 2013). Electrolytic conduction is further modeled with Archie's law (Archie, 1942)

$$\sigma_{el} = \sigma_w \phi_s^m Sr^n \tag{2.13}$$

where σ_w is the conductivity of the fluid, ϕ_s is the porosity of the solid matrix, and Sr is the saturation. The exponent m is the cementation exponent, which describes the connectivity of the pore space. The larger the value of m the less connected the pore space. The exponent n is the saturation exponent, which is approximately equal to 2 for unconsolidated sediments (Singha et al., 2015). For the analysis in this chapter, σ_{surf} is considered as a given for different soil units. A synthetic soil unit in this study is defined by a porosity value ϕ_s, a cementation exponent m, and a surface conductivity value σ_{surf}.

2.3.2. Material properties of the soil units
A synthetic dike model was built to evaluate the EM exploration of dikes. The synthetic dike stems from the geotechnical model of a real dike stretch. The dike is located along the Lek river in the West of the Netherlands, near the village of Bergambacht. The dike at Bergambacht and the subsurface consist of a succession of soft soils, i.e. clays and peats (organic), lying on top of a sand layer. This composition is typical of dikes in the Rhine-Meuse Delta (Koelewijn, Hoffmans, and Van, 2004). The pore pressure in the sand layer, which is influenced by the water height in the river, makes the dike susceptible to macrostability failure due to uplift (Van, Koelewijn, and Barends, 2005). A full-scale uplift failure test was carried out in a stretch of the dike (Koelewijn, Hoffmans, and Van, 2004). Therefore, comprehensive site investigation data and a geotechnical schematization of the soil units were available to formulate a synthetic model.

The synthetic model aims to replicate the geometry and subsurface heterogeneity of the dike at Bergambacht. The synthetic model extends from a distance of −50.0 m to a distance of 200.0 m, and from an elevation of −17.0 m to an elevation of 5.0 m. The dike body extends from a distance of 25.0 m to a distance of 65.0 m, and from an elevation

of 0.0 m to an elevation of 5.0 m. The dike model extends to the right, far from the dike core, so that the synthetic evaluation of EM methods can also be carried out on the flat portion of the model without topographic effects. The model consists of nine soil units (A to I), which aim to represent the actual succession of soil layers found in the site investigation data, i.e. soft soils (units E to I) on top of a sand layer (unit A). Sand and silt layers (units B to D) were embedded in the soft soils. Figure 2.3 (top) shows the soil units of the synthetic dike model. The bulk electrical resistivity of each soil unit was calculated with Equation 2.12. The values of the pore-scale properties (ϕ_s, m, σ_{surf}) were chosen by matching the soil type of each soil unit with the soil type on published databases, such as (Weller, Slater, and Nordsiek, 2013). The intention was to formulate realistic pore-scale electrical values that lead to a realistic electrical resistivity model. In clayey soils, for example, the surface conductivity is high and the pore-space is poorly interconnected, despite having higher values of porosity. Therefore, the electrical conductivity of a clayey soil is higher than that of a sandy soil, which has low surface conductivity. Figure 2.3 (bottom) shows the electrical resistivity of the synthetic dike model, and Table 2.2 summarizes the electrical pore-scale and bulk properties of each soil unit.

The dike of Figure 2.3 appears to represent realistically the geological setting and the bulk electrical resistivity of an actual dike. The dike model contains geotechnical and geophysical features that are important to consider in the exploration of dikes. First, the bulk resistivity of distinct soil units shows, in some cases, similar values. The soil units are then indiscernible with EM exploration when they lie next to each other, e.g. soil units E and H. Second, sandy and silty units (B, C, and D) are embedded within the soft units (E to H). The hydraulic properties of sandy and silty units are different from that of the host medium and negatively affect the stability of dikes. Such units are a source of risk in geotechnical analysis because they are difficult to detect with conventional site investigation methods. Third, the soft-soil units (E to H) are notably different from the basal sand unit in terms of soil type and bulk electrical resistivity. However, it is important to note that both ERT and EMI techniques exhibit reduced sensitivity as depth increases. Specificaly, the depth of investigation of the EMI devices of Table 2.1 is lower than (15.0 m). Finally, the model contains thin horizontal units (C, D, and I) and relatively thin units (F). These units can be difficult to detect with EM exploration even though the material properties are different. The realistic values of material properties simulated in this dike model allow for a representative evaluation of EMI methods for the exploration of water defences.
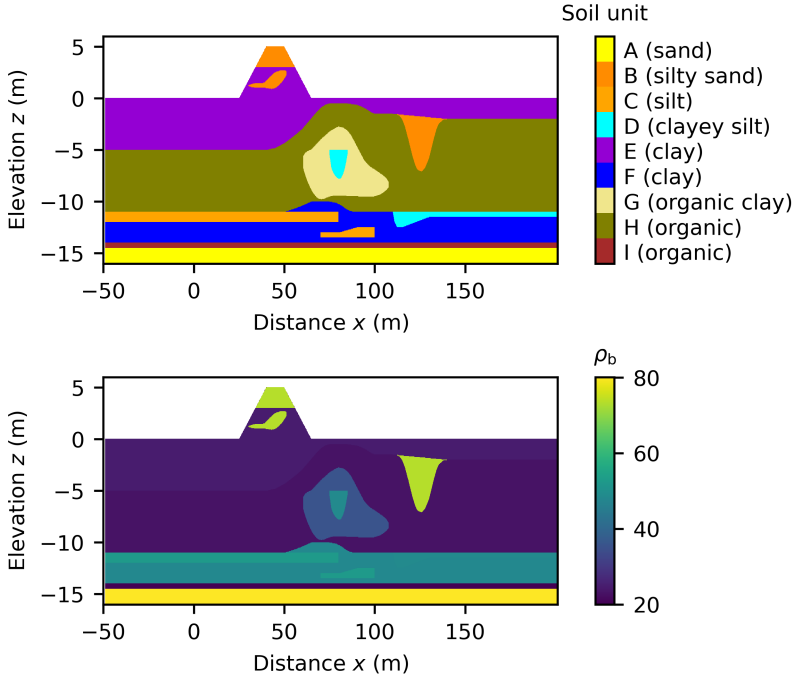
Figure 2.3: Synthetic dike model. The soil units, sorted by porosity, are shown in the top figure. The bulk electrical resistivity of the soil units is shown in the bottom figure. In general, the lower the porosity, the higher the electrical resistivity.

Unit name	Soil type	ϕ_s (-)	m (-)	σ_{el} (Sm^{-1})	σ_{surf} (Sm^{-1})	σ_b (Sm^{-1})	ρ_b (Ωm)
A	sand	0.25	1.50	0.008	0.001	0.009	112.4
B	silty sand	0.29	1.30	0.013	0.001	0.014	73.3
C	silt	0.34	1.80	0.009	0.010	0.019	52.5
D	clayey silt	0.35	4.50	0.001	0.020	0.021	48.6
E	clay	0.38	4.50	0.001	0.040	0.041	24.5
F	clay	0.41	4.80	0.001	0.020	0.021	48.0
G	organic clay	0.65	4.76	0.008	0.020	0.028	35.6
H	organic	0.74	1.30	0.043	0.001	0.044	22.9
I	organic	0.91	2.20	0.051	0.001	0.052	19.3

Table 2.2: Electrical pore-scale and bulk properties of the soil units of the synthetic dike. The electrical conductivity of water, σ_w and the saturation, Sr, were kept constant at $0.07\,\text{Sm}^{-1}$ and 0.95, respectively.

2.4. ERT synthetic survey

A synthetic surface-based ERT survey was carried out on the dike of Figure 2.3 by solving Equation 2.1 with the python package pyBERT (Rücker, Günther, and Spitzer, 2006). The ERT data was collected with a dipole-dipole and a Wenner-alpha configuration. The electrodes were laid out on the surface of the dike model starting from a distance of 0.0 m and with a separation of 1.0 m. A roll-along approach was used to simulate field data acquisition and to cover the extension of the model up to a final distance of 215.0 m. The roll-along approach consisted of 144 electrodes used at each station, e.g. the electrodes were located from a distance of 0.0 m to a distance of 143.0 m. Then, 36 electrodes were rolled to the right so that the position of the 144 electrodes shifted by 35.0 m. The electrodes were finally rolled until the position of the last electrode reached a distance of 215.0 m. Figure 2.4 shows the pseudo sections derived from synthetic ERT data using dipole-dipole and a wenner-alpha arrays. These pseudo sections provide approximate two-dimensional representations of the subsurface resistivity. The pseudo sections in 2.4 exhibit distortions with respect to the true model. These distortions are characteristic of the geometry of the electrode arrays (Loke, 1995). The pseudo sections also show that the dipole-dipole array delineate better the resistive soil unit B which is located inside the dike core and in the right part of the dike. The better delineation is expected since the dipole-dipole array produces more complex pseudo sections than the wenner-alpha array (Loke, 1995).

Current multi-channel ERT systems can optimize the acquisition of dipole-dipole data, such that, in the same time frame, a much larger number of dipole-dipole measurements can be acquired compared to wenner-alpha measurements. An important limitation to the dipole-dipole array is the susceptibility to environmental noise. In this synthetic data set, a limit of 5000 has been set to the geometric factor to prevent noisy measurements to affect the tomographic inversion. Prior to tomographic inversion, random-normally distributed noise with a standard deviation $\epsilon_d = \epsilon_{\text{base}} + \epsilon_\phi$ was added to the apparent resistivity data following the noise model of Friedel (2003). The model consists of a base noise level, $\epsilon_{\text{base}} = 0.5\%$, and a voltage-dependent noise level, $\epsilon_\phi = U_{\text{min}}/\Delta\phi$. The sensitivity of the ERT device, U_{min}, was picked as 50 μV, and $\Delta\phi$ was calculated from Equation 2.2 at a current $I = 0.4$ A. The Wenner-alpha measurements were primarily affected by the base noise level while the dipole-dipole measurements were affected by both types of noise. The acquisition parameters of the ERT data are summarized in Table 2.3.

2.5. EMI synthetic survey

A synthetic EMI survey was carried out on the dike of Figure 2.3 by solving Equation 2.3 in three dimensions with the python package emg3d (Werthmüller, Mulder, and Slob, 2019). The simulated the EMI devices of Table 2.1. It is worth noting that the synthetic data collection was limited to the flat part of the model located to the right of the dike core. This choice was driven by practical considerations; EMI devices must be maintained perpendicular to the surface, a requirement that becomes challenging to meet on
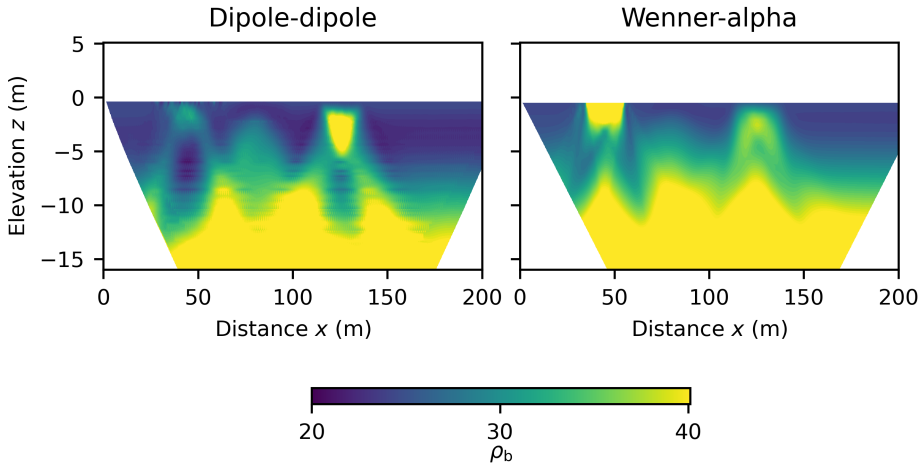
Figure 2.4: ERT noise-free survey data of the synthetic dike model collected with a dipole-dipole and a wenner-alpha array. The data is displayed as a pseudo section.

Parameter	Value
Electrode spacing	$1.0\,\mathrm{m}$
Number of electrodes	144
Roll-along electrodes	36
Number of rolls	2
Array type	Dipole-dipole and Wenner-alpha
Maximum geometric factor	5000

Table 2.3: Acquisition parameters of the synthetic ERT data. The data was collected with a roll-along approach.

2

sloped terrain. Consequently, the position of the source started at a distance of 70.0 m and ended at 190.0 m. The receivers were located at the right of the source with the separation specified in Table 2.1. The measurements consisted of the vertical (HCP) and radial (PRP) components of the magnetic field ratio H_s/H_p. Figure 2.6 shows the synthetic EMI data collected with each EMI device. Figure 2.6 also shows the EMI data simulated with a one-dimensional assumption (Equations 2.6 and 2.7). Prior to tomographic inversion, random-normally distributed noise was added to the EMI to simulate actual field conditions. The standard deviation of the noise (in parts per million) was considered to increase linearly for both receivers as a function of frequency (in Hertz) $\sigma_d = 0.02 f$. The value of the slope (0.02) was chosen because it simulated realistic noise levels for the EMI devices of Table 2.1. The data error, ϵ_d, which is needed to invert the EMI data (Equation 2.9), was calculated by dividing the standard deviation of the noise by the measured EMI response at each sensor $\epsilon_d = \sigma_d/(H_s/H_p)$.

2.5.1. GEOMETRIC VERSUS FREQUENCY SOUNDERS (EMI)

Figure 2.6 shows two features of the EMI data that are relevant for the exploration of dikes. First, the geometric sounders (DUALEM-842 and DUALEM-421) show a more pronounced variability in the measured response H_s/H_p than the frequency sounder (GEM2). The variability in the responses is associated with the variability in the electrical resistivity of the subsurface. To illustrate, units B, D, and G have a lower electrical resistivity than the background, so they are expected to cause a drop in H_s/H_p. The GEM2 captures the presence of unit B only at the higher end of operation frequencies. Meanwhile, the DUALEM devices capture unit B, and seem to capture units D and G with the far-offset receivers, as evidenced by a slight decrease in the H_s/H_p signal. The second relevant feature of the EMI data is the deviation in the response of the far-offset receivers. The three-dimensional response deviates from the one-dimensional response in the presence of unit B. Since the inversion of EMI data uses a one-dimensional forward model, deviations from the one-dimensional assumption add complexity to the interpretation of the data. The HCP receiver at 8 m shows the largest deviation with respect to the one-dimensional assumption. The deviation is visible in the HCP receiver as a vertical shortening and deformation of the response. In short, the pronounced sensitivity of the geometric sounders is favorable to detect adverse soil units at far-offsets, such as units B, D, and G, but the deviations from the one-dimensional assumption add complexity to the interpretation of the data.

In the range of electrical properties of unconsolidated deposits, such as those in Figure 2.3, geometric sounders are more effective in capturing heterogeneity because they enhance the signal-to-noise ratio without reducing the depth of investigation. To elaborate on this point, consider the response H_s/H_p of a homogeneous half-space. Figure 2.5 shows the quadrature response of the HCP sensors for the DUALEM-842 and the GEM2 devices. To maximize the sensitivity of the GEM2 to resistivity changes in unconsolidated deposits, it is necessary to operate it at the higher frequencies within its range. However, the gain in signal-to-noise ratio associated with a higher frequency is counteracted by a reduced depth of investigation as this is related to the skin depth (Huang,
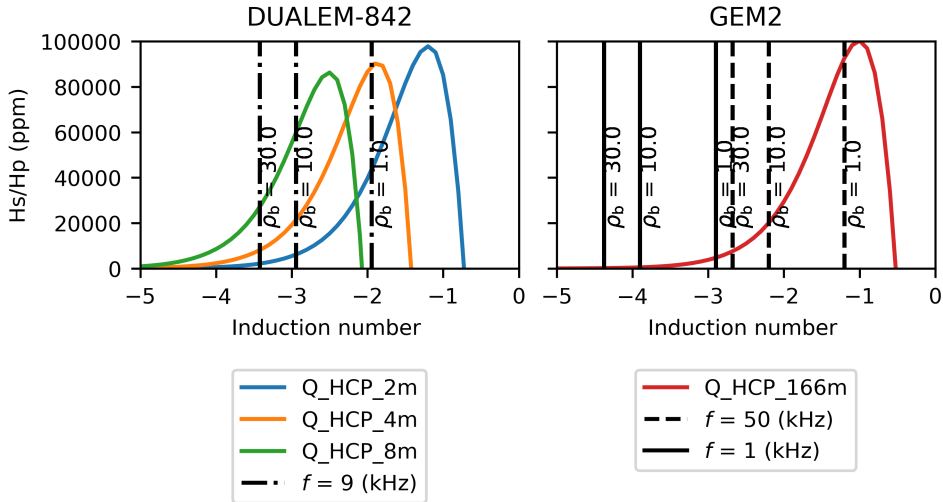
Figure 2.5: Response sensitivity of two commercial EMI devices, DUALEM and GEM2, as a function of induction number $(\sigma\mu\omega)^{1/2}s$. The DUALEM device achieves heightened response sensitivity by increasing the source-receiver separation, whereas the GEM2 device achieves a comparable result through an increase in frequency. The responses were calculated for a height of 0.2 m

2005). On the other hand, the DUALEM-type devices increase the sensitivity of the signal by increasing the source-receiver separation while keeping the frequency constant. Therefore, geometric sounders are more effective in mapping heterogeneity of unconsolidated deposits such as those modeled in this chapter. A possible drawback of geometric sounders is the one-dimensional assumption made in tomographic inversion.

2.5.2. THE PROBLEM WITH FAR-OFFSET RECEIVERS

The large source-receiver offset in some EMI geometric sounders, e.g. DUALEM-842, adds complexity to EMI data interpretation because their response deviates from the one-dimensional response. In the one-dimensional approximation and for conductivity values in the range of values presented in Table 2.2, conductive bodies cause a lift in the response, and resistive bodies cause a drop in the response. However, Figure 2.6 shows that the presence of a resistive body (unit B) does not cause the expected drop in the three-dimensional response for the HCP receiver at 8 m. The effect is more pronounced for larger values of source-receiver separation where the response seems counter intuitive. For example, unit B (resistive body), causes a lift in the response of a hypothetical HCP receiver at 12 m (dotted line in Figure 2.6). The response of the HCP receiver at 12 m is similar to the one-dimensional response due to the presence of a conductive body. Therefore, the interpretation of important subsurface features, such as paleochannels (unit B), becomes cumbersome with data of far-offset receivers. In that regard, full three-

dimensional forward models (Equation 2.3) could improve the interpretation of the EMI data.

2.6. DISCUSSION

2.6.1. COMPARISON OF ERT AND EMI GEOPHYSICAL IMAGES

The ERT and EMI data simulated in the previous sections were used to generate tomograms (Figure 2.7). The ERT tomograms show the subsurface from a distance of 0 m to a distance of 200 m, which includes the core of the dike. The EMI tomograms show the subsurface from a distance of 70 m to a distance of approximately 200 m. Thus, the EMI data does not show the core of the dike. An optimum regularization was found for each tomogram following the L-curve method (Günther, Rücker, and Spitzer, 2006b). The EMI tomograms benefited from applying a boxcar filter to remove the synthetic jitter in the raw data. These methodologies are common practice in EMI data processing and are known to reduce artifacts in EMI tomograms significantly (Lavoué et al., 2010; Delefortrie et al., 2019). The ERT tomograms show a more detailed picture of the subsurface than the EMI tomograms. In any case, the tomograms only show large-scale features (units A, B, D, G, and H).

The ERT tomograms show comparable results, but the dipole-dipole tomogram shows fewer artifacts than the Wenner-alpha tomogram. This result agrees with the fact that the dipole-dipole array is more sensitive to horizontal changes while the Wenner-alpha array is more sensitive to vertical changes (layered structures). The ERT tomograms cannot discern between units E and H even though they are close to the sensors. The difference in electrical resistivity of these two units is below noise levels. On the other hand, the electrical resistivity of Unit B (paleochannel) is significantly different from the background (units E and H). Thus, both ERT tomograms capture unit B. Unit B is also present in the dike core as two separate sand bodies. The tomograms show the presence of a sand body in the dike core, but the shape is not discernible. The ERT tomograms can also capture the more subtle presence of units D and G embedded in H, but the dipole-dipole tomogram delimits the shape of unit G more clearly. The basal sand layer (Unit A) is also visible in both ERT tomograms, but the shape is not horizontal as in the original model, which is a result of the subsurface complexity above the basal sand. Unit F is not discernible even though it is electrically different from unit H and unit A. The depth of unit F reduces its detectability, as is the case with the thin soil layers (units C, D, and I).

The features shown in the EMI tomograms differ considerably from device to device. In the GEM2 tomogram, unit B, the most prominent anomaly in the model, is barely detectable, potentially leading to ambiguity in field data interpretation. Units D and G are not distinguishable in the GEM2 tomogram. In contrast, the DUALEM-421 can capture unit B clearly, but units D and G are less visible. The most detailed tomogram was generated with the DUALEM-842 data although artifacts are visible on the sides of unit B. The DUALEM-842 tomogram captured three geotechnically-relevant features of the input model. First, the DUALEM-842 tomogram clearly captures the presence of unit B. Second, the DUALEM-842 tomogram indicates the presence of units D and G. Third,

the DUALEM-842 tomogram shows the presence of the basal sand (unit A), albeit with some influence from variability between the sensors and unit A, affecting its depth and shape. From a practical point of view, these three large-scale features are the same features captured in the ERT tomograms. Therefore, geometric sounders with far-offset receivers, such as the DUALEM-842, could be a cost-effective alternative to ERT for reconnaissance surveys.

2.6.2. EFFECTIVENESS OF EM METHODS IN SALINE ENVIRONMENTS

EM methods are effective at mapping subsurface heterogeneity because sandy soils tend to have distinctly higher electrical resistivity values than cohesive and organic soils. For instance, unit B in Figure 2.3 has a electrical resistivity of $73.3\,\Omega$m while the organic background (unit H) has an electrical resistivity of $22.9\,\Omega$m. In low salinity conditions, electrolytic conduction of sandy soils is much smaller than the surface conductivity of cohesive and organic soils. On the other hand, brackish water or sea water reduces the bulk electrical resistivity of soils which in turn could reduce the effectiveness of EM methods to map heterogeneity. In the presence of saline water, electrolytic conduction becomes dominant in sandy soils (see Equation 2.12) which reduces drastically the bulk electrical resistivity. For example, by increasing the electrical conductivity of water to the level of brackish water (0.5 S/m), the bulk electrical resistivity of unit B and H become $10.96\,\Omega$m and $3.27\,\Omega$m, respectively. At the salinity level of sea water (3.0 S/m), the bulk electrical resistivity of unit B and H become $1.84\,\Omega$m and $0.54\,\Omega$m, respectively. Higher levels of water salinity result in decreased electrical resistivity, which could hamper the effectiveness of EM exploration for two main reasons. Firstly, the contrast in electrical properties between different geological soil units is diminished. Secondly, interpreting EM data becomes more challenging since the electrical resistivity values do not conform to interpretation heuristics.

Saline water can make geotechnically-relevant subsurface features undetectable with EM exploration. To illustrate, Figure 2.8 (left) shows variations in bulk electrical resistivity at different levels of water salinity. The pore-scale properties used in Figure 2.8 (left) were the same as presented in section 2.3. The figure shows that the sand channel (unit B) in Figure 2.3 becomes indiscernible from the organic background (unit H) even though the soil units are vastly distinct from a geological point of view. The similarity in electrical resistivity arises from the implementation of a low cementation exponent at the pore-scale modeling of both units. Consequently, the values of electrical resistivity are comparable because electrolytic conduction becomes dominant. On the other hand, units D and G are visible in the organic background despite the varying levels of water salinity. Units D and G, which are comparable to units B and H in terms of porosity, are not affected as much by electrolytic conduction due to their high cementation exponent. In any case, the electrical resistivity contrast is reduced which reduces the effectiveness of EM exploration. The reduced contrast is further exacerbated in tomograms due to the smoothness involved in the inversion process. Figure 2.8 (right) shows the ERT tomograms of the dike model estimated at different salinity levels. Clearly, soil unit B is indiscernible from the background in the tomograms. Interestingly, clay units
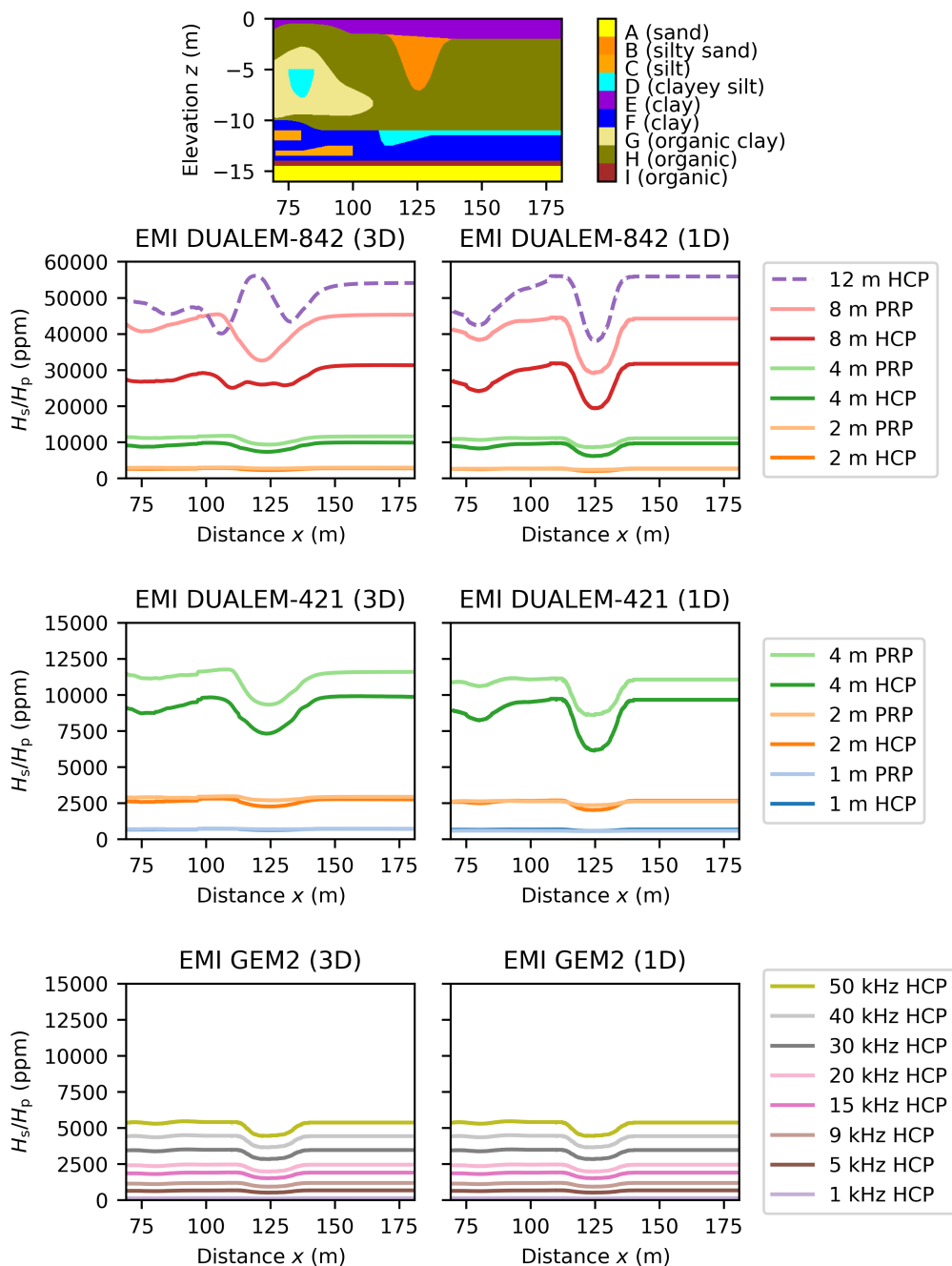
Figure 2.6: EMI noise-free synthetic data simulated with three EMI devices (DUALEM-842, DUALEM-421, and GEM2). The plots show the quadrature (imaginary) component of the ratio H_s/H_p. The left column shows the response calculated with a fully three-dimensional approach (Equation 2.3). The right column shows the response calculated with a one-dimensional approximation (Equations 2.6 and 2.7). The top row also shows the response of a hypothetical HCP sensor with a source-receiver separation of 12 m (far-offset). Dike model is added at the top for reference.
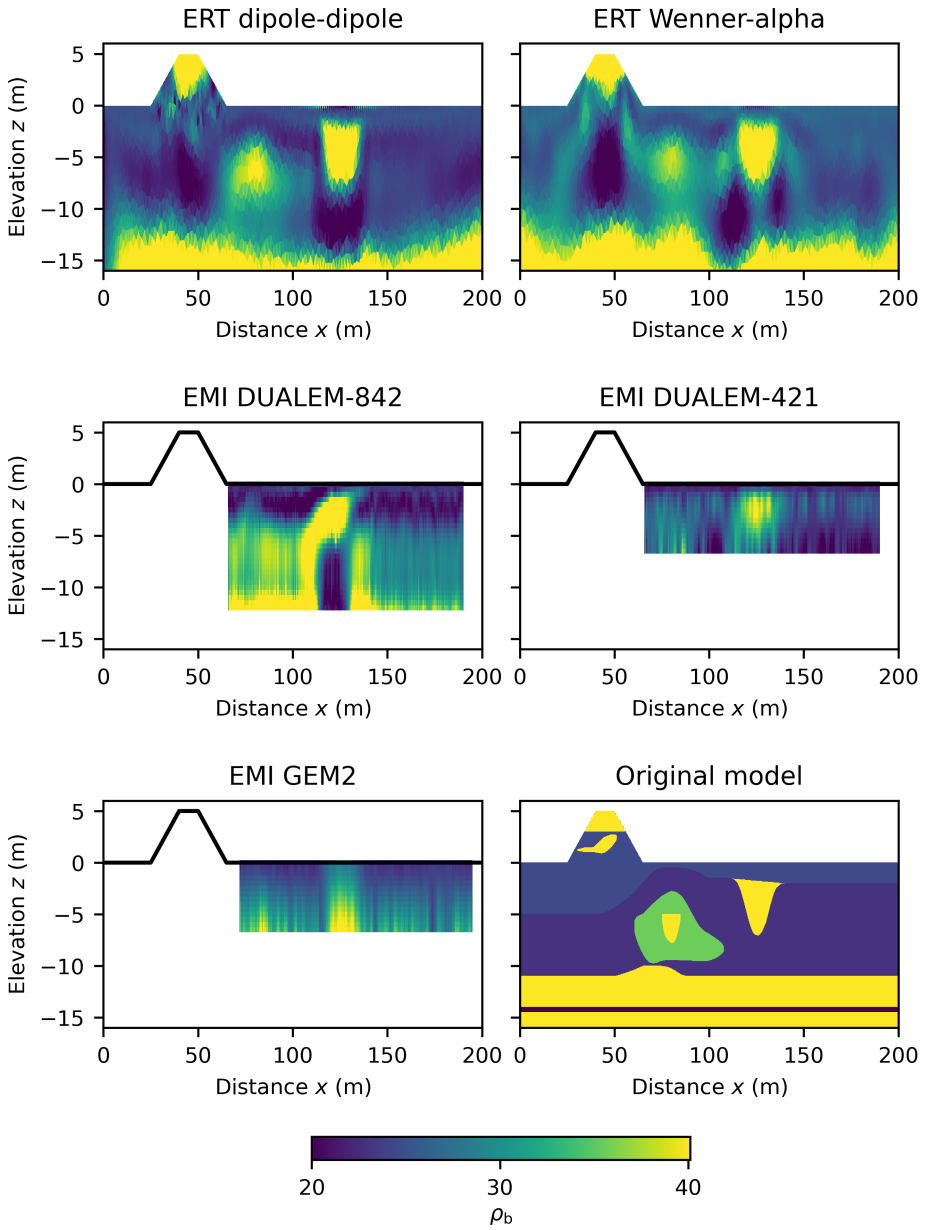
Figure 2.7: Comparison of EM tomograms of the synthetic dike model.

tend to have larger values of electrical resistivity in the presence of water salinity which flips the usual interpretation heuristics, that is, clayey soils become more resistive than sandy soils.

EMI is potentially a more effective tool to explore the subsurface in high-salinity environments as the sensitivity of EMI increases at low values of electrical resistivity. To illustrate, Figure 2.9 (left) shows the EMI H_s/H_p response at different salinity levels. The sensor data of Figure 2.9 (left) shows subsurface heterogeneity even though the contrast in electrical resistivity is low. The sand channel (unit B) is visible in the signal of all sensors, except the HCP-8m, as a drop in H_s/H_p. On the other hand, units D and H are visible in the signal as an increase in H_s/H_p. The EMI tomograms, which are not shown, are more difficult to make and interpret. In saline environments, a careful selection of sensor data is required to invert EMI data. The inphase response, which was previously not used, needs to be used in the inversion process. Figure 2.9 (right) shows the ratio of the quadrature to the inphase at different salinity levels. At low salinity levels, the quadrature is many times larger than the inphase. Thus, only the quadrature is required for inversion. As the electrical resisitivity increases due to salinity, the inphase increases. At the salinity level of sea water, the inphase is dominant at the HCP-8m sensor. In coastal areas, where water salinity is high, the effectiveness of EM methods to explore subsurface heterogeneity is greatly reduced.
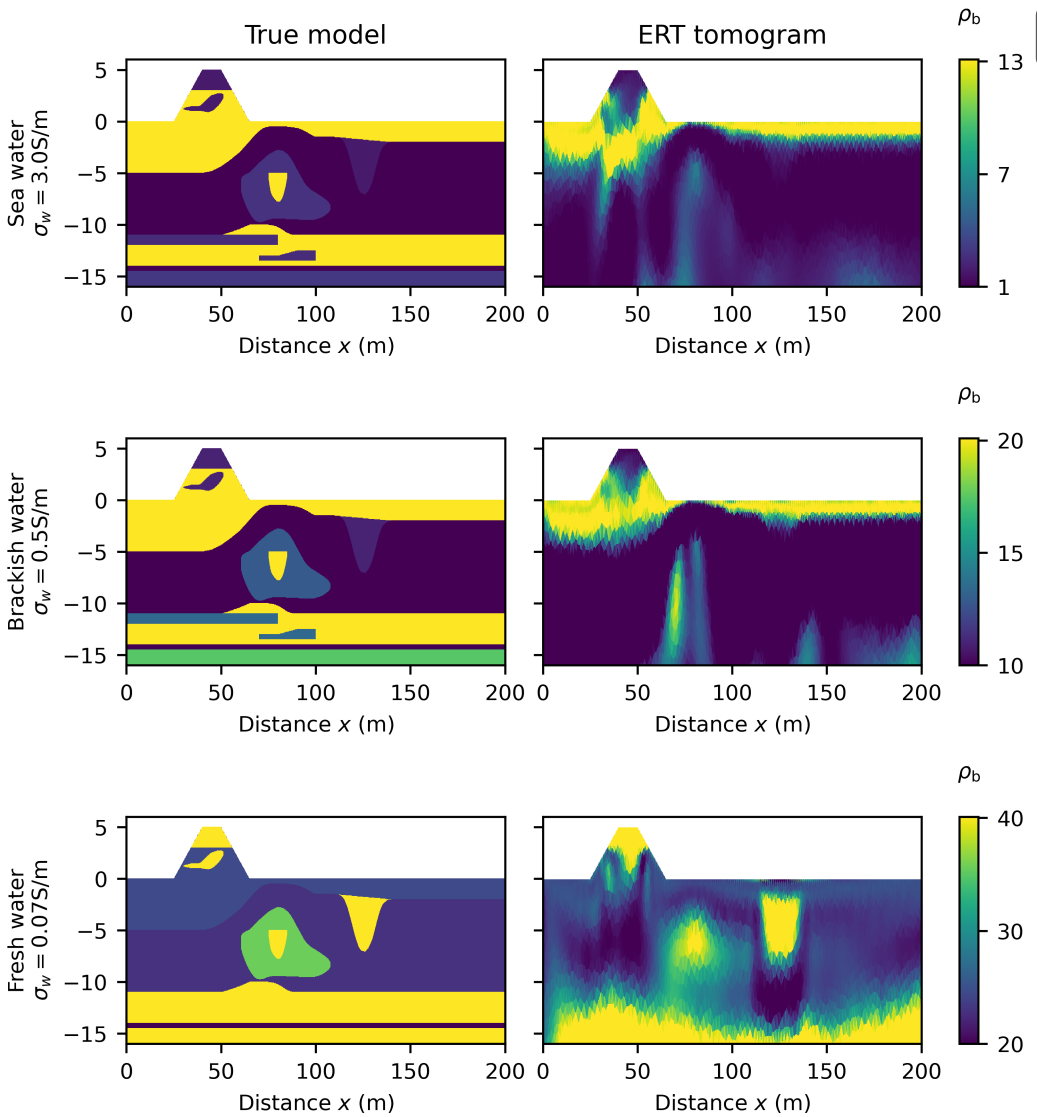
Figure 2.8: Influence of water salinity on bulk electrical resistivity ρ_b (left column) and the corresponding ERT tomograms (right column). Salinity levels increase from bottom to top, quantified by electrical conductivity σ_w.

2

Figure 2.9: EMI noise-free synthetic data simulated (three-dimensional equation) at different levels of water salinity with the acquisition setup of the DUALEM-842. Salinity levels increase from bottom to top, quantified by electrical conductivity σ_w.

2.7. CONCLUSIONS

The interplay of pore-scale properties results, in some cases, in overlapping material properties for vastly different geotechnical soil units. 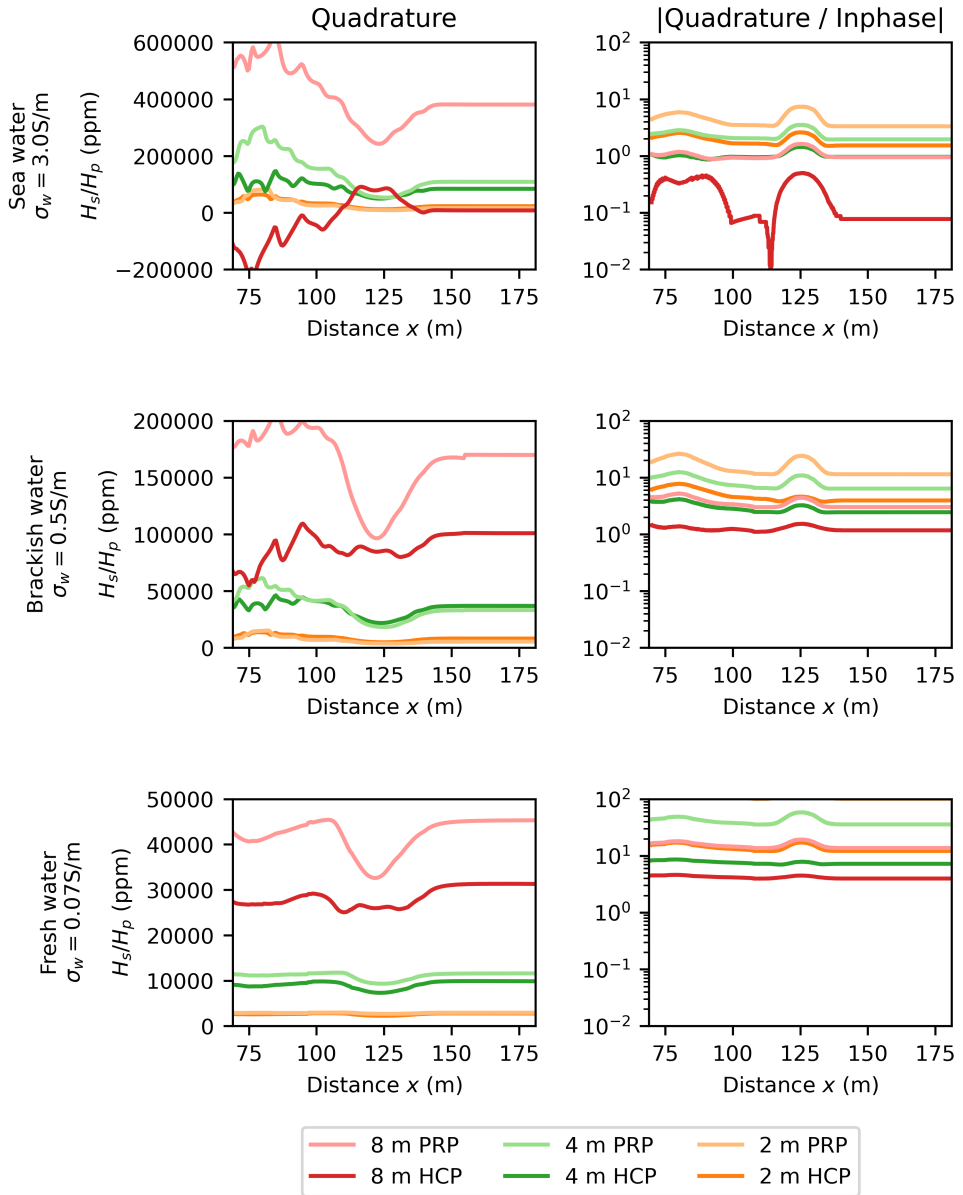Particularly, the electrical conductivity of clayey soils tends to overlap with that of organic soils because the high surface conductivity of clayey soils is comparable to the high electrolytic conductivity of organic soils. On the other hand, the soil units in a geological setting share common pore-scale properties, such as water salinity, so the expected range of bulk electrical conductivity values is limited. Therefore, small-scale features, such as thin layers, are not likely to be detected because they cannot drive a sufficiently large change in the physical response of the EM devices. Therefore, the practical utility of EM exploration in dikes is to detect large-scale changes in soil composition. A geotechnically-relevant application of EM exploration is then the detection of paleochannels (resistive bodies) embedded in soft soils (conductive bodies).

EMI geometric sounders with far-offset receivers are more sensitive to subsurface variability than frequency sounders. A primary feature of geometric sounders is that they enhance the signal-to-noise ratio without reducing the skin depth and the depth of investigation. Among the tested EMI methods, the geometric sounder with far-offset receivers, DUALEM-842, captured subsurface variability to a similar extent than ERT. Therefore, such a geometric sounder with far-offset receivers is a cost-effective alternative to ERT, at least for the detection of large-scale adverse geological features, e.g. paleochannels. Nevertheless, the interpretation of far-offset receiver data is complex because the response of these sensors deviates from the one-dimensional response used in data inversion. A three-dimensional inversion approach could aid the interpretation of far-offset receiver data by reducing tomographic artifacts.

Electromagnetic (EM) methods are effective tools for mapping subsurface heterogeneity, particularly due to the distinct differences in electrical resistivity values between sandy, cohesive, and organic soils. However, their effectiveness can be reduced in the presence of saline water because the contrast in electrical resistivity values is reduced. The impact of saline water on the electrical resistivity becomes evident in the models of the subsurface and even more in the EM tomograms. Notably, the sand channel, which was distinguishable from the organic background at low-salinity, becomes indiscernible at higher levels of water salinity. Moreover, the presence of saline water can lead to a change in the relative electrical resistivity values between different soil types. For instance, clayey soils, which were previously less resistive than sandy soils under low-salinity conditions, could become more resistive than sandy soils as the salinity level increases. Ultimately, this makes the interpretation of EM exploration data more challenging as the electrical resistivity values no longer conform to standard interpretation heuristics.

3

GEOMETRIC VARIABILITY OF SOIL LAYERS

In Chapter 3, a method is proposed to estimate the geometry of soil layers. The method combines local point data, i.e., data obtained from a CPT or a borehole log, and geophysical tomograms in a universal cokriging framework. To reduce subjectivity in the interpretation of tomographic images, an automated edge detection technique was used. The combined approach was applied to characterize two test sites where the presence of paleochannels locally change the geometry of soil layers. The results show that a combined approach enables the reduction of sampling efforts with an improved estimation of geometric variability.

The contents of this chapter have been published in the journal Georisk: Assessment and Management of Risk for Engineered Systems and Geohazards.

3.1. Introduction

Dikes form an essential part of the primary flood defences along the coast and major rivers in the Netherlands. Multiple failure mechanisms threaten the stability of these dikes. Hence, they are subjected to periodic reliability assessments (MinIM, 2016; Waal, 2018). In reliability assessments, a special focus lies on the geological schematization of the subsurface (Hijma and Lam, 2015). Characterizing geometric variability of soil layers is a key step within the geological schematization process. In the failure mode of macrostability, for example, the thickness of a weak layer determines the shape of the slip surface and the reliability of the dike. Geometric variability is also important for the reliability assessment of dikes in terms of piping. In clay-over-sand dikes, the thickness of the clay layer in the hinterland generates resistance against uplift which is the first phase of piping (Sellmeijer, 1988; Sellmeijer and Koenders, 1991).

The Dutch subsurface is notoriously heterogeneous. It is built up by sequences of gravely sandy aquifers alternated by confining clayey aquitards. The uppermost aquifer, which was deposited during the last glacial period (Pleistocene epoch), forms a nearly continuous sandy substrate. These deposits are overlain by the Holocene deltaic wedge which forms a heterogeneous confining layer. This layer is mostly composed of aquitard floodplain clays, clay-fine sand, dominated intertidal flats, and peats. However, it is dissected by (partly) isolated alluvial and tidal channel sand bodies (Bierkens, 1994; Weerts, 1996; Hijma and Cohen, 2011). These channel-belt sand bodies act as shallow-depth aquifers and locally occur directly underneath dikes. In addition, small-scale variability of sand body architecture also occurs which is the result of autogenic processes. Due to this complexity, it is challenging to characterize the geometric variability of soil layers with conventional site investigation methods. Methods, such as the Cone Penetration Test (CPT) and borehole drilling, sample the subsurface in detail, yet locally. In the Netherlands, CPT samples are normally collected with a spacing of 100 m (ENW, 2012). In the Dutch subsurface; however, the geometry of soil layers often varies on scales smaller than 25 m (Hijma and Lam, 2015). The mismatch between site investigation density and actual subsurface variability leads to schematization uncertainties. Although schematization uncertainties are compensated with safety factors (ENW, 2012), large uncertainties result in uneconomical designs or unnecessary reinforcement of existing structures. Therefore, it is of paramount importance to reduce these uncertainties without exhaustively sampling the subsurface. For this purpose, geophysical methods are a well-established option because they map the subsurface in a horizontally-continuous manner.

Even though geophysical methods provide valuable insights into the variability of soil layers, their use has been limited to the visual interpretation of geophysical images. Few attempts have been made to objectively derive information from geophysical data. For example, deterministic (Auken and Christiansen, 2004) and probabilistic (de Pasquale et al., 2019) inversion methods have been used to estimate the geometry of soil layers and material properties. Alternatively, Hsu et al. (2010) and Chambers et al. (2012) applied automated detection techniques to tomographic images in order to estimate the geometry of soil layers. The problem is that geophysical data are often

affected by instrumental drift, lateral heterogeneity, and lack of resolution (Delefortrie et al., 2019; Minsley et al., 2012). In such cases, the quantities estimated with these methods, e.g. geometry, though informative of the variability trend, are inherently inaccurate.

We propose a combined approach to estimate the geometry of soil layers. We combine the trend of geometric variability estimated from geophysical data with accurate data derived from boreholes. We use the potential field method (Lajaunie, Courrioux, and Manuel, 1997) to combine both data sets. The potential field method generates a geometric model of the subsurface via universal cokriging of the layer orientations and contact points between soil layers. We use the Laplacian edge detection technique to estimate soil interfaces from geophysical tomography. The layer orientations are then calculated as the dip angle of the tomographic interfaces. Thus, we use layer orientations derived from tomography and the contact points between soil layers obtained from directly sampling the subsurface. We test the approach with two electromagnetic geophysical methods that are widely used in the site investigation of dikes, namely Electric Resistance Tomography (ERT) and Electromagnetic Induction (EMI).

We first describe the proposed approach and the main steps behind it. We describe the technique to obtain layer orientations from tomograms, and the potential field method. Afterwards, we present a proof of concept of our approach with a synthetic two-layer model with internal variability. Our approach is then applied to two study sites. One site located in an alluvial environment across an old river channel and the other site located in a tidal environment along the longitudinal section of a dike. In both cases, the geometry of the upper layer is characterized.
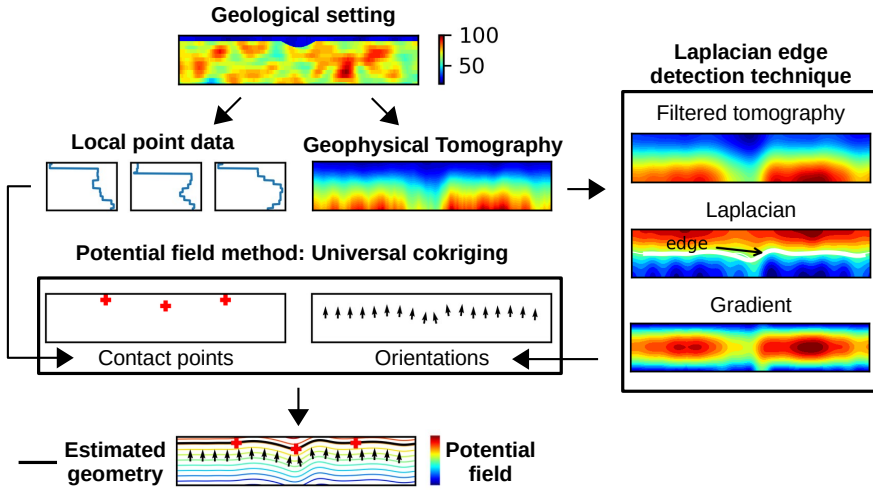
Figure 3.1: Schematic of the approach proposed to estimate the geometry of soil layers of a geological setting. The approach uses local point data and geophysical tomography. Local point data are used to derive the contact points between soil layers. Meanwhile, geophysical tomography is used to derive the orientations of the soil layers. The orientations are calculated from the edges detected in the geophysical tomography. The estimated geometry of the soil layers is obtained via universal cokriging of the contact points and the orientations.

3.2. METHODOLOGY

We propose a workflow to estimate the geometry of the soil layers of a geological setting (Figure 3.1). Local point data and geophysical tomograms are used as input in this workflow. Local point data, such as CPTs and borehole logs, are used to derive the contact point or interface between soil layers. ERT and EMI tomograms are used to derive the orientations of the soil layers. The orientations of the soil layers are calculated from the edges automatically detected in the tomographic images (Section 3.2.1). Finally, orientations and contact points are used to estimate the geometry of soil layers via the potential field method of Lajaunie, Courrioux, and Manuel (1997) (Section 3.2.2).

3.2.1. LAYER ORIENTATIONS

The Laplacian edge detection technique was used to automatically detect edges in the tomographic images. The edges in the tomograms were interpreted as the interfaces between soil layers. In the Laplacian edge detection technique, edges are defined at the zero-crossings of the Laplace operator applied to the tomogram

$$\nabla^2 m(x,z) = \frac{\partial^2 m}{\partial x^2} + \frac{\partial^2 m}{\partial z^2} = 0, \tag{3.1}$$

where $m(x,y)$ are the material properties of the medium represented in the tomogram i.e. electrical resistivity. Due to tomographic artifacts and geological complexity, fake edges and edges that are not of interest are also detected in the tomography. Thus, additional processing and interpretation are often needed. Processing with smoothing

and thresholding is effective in reducing the detection of fake edges (Mlsna and Ro-dríguez, 2009). Smoothing is effective in reducing the detection of fake edges caused by the small-scale components in the tomogram. An appropriate filter strength should be picked based on the frequency content of the tomographic images. On the other hand, thresholding removes edges that show a low tomographic gradient. From the remaining edges in the tomogram, the edges that correspond to the geological feature of interest are picked based on the geological interpretation of the tomogram. The final selection of tomographic edges is assumed to represent the trend of geometric variability of the soil interfaces. We represent this trend with the orientations of the edges (Figure 3.2a). The orientation is a unitary vector that is perpendicular to the soil layer. The orientations are calculated from the dip angle of the tomographic edges. In two dimensions the orientations become

$$orientation = -\sin(dip)\,\boldsymbol{i} + \cos(dip)\,\boldsymbol{j} + 0\,\boldsymbol{k}, \tag{3.2}$$

where the dip angle is calculated directly from the tomographic edges

$$dip = \tan^{-1}(\frac{\mathrm{d}z_{\mathrm{int}}}{\mathrm{d}x_{\mathrm{int}}}) \tag{3.3}$$

where x_{int} and z_{int} are the coordinates of the edges. The dip angle calculated from the tomographic edges is signed which defines the pointing direction of the orientation vector. Alternatively, the orientation vector can be defined in terms of dip and azimuth.

The performance of the edge detector depends on tomographic resolution. Resolution in turn depends on measurement physics, regularization, acquisition design, and physical contrast between soil layers. Lack of resolution in geophysical tomograms leads to poorly mapped regions of the subsurface where automated detection techniques do not perform well. In the regions where automatically detected edges are not informative, assumptions have to be in terms of the contact between soil layers or their orientations. The assumptions made in this part of the process have a large effect on the estimated geometric variability. The advantage of the potential field method (Section 3.2.2) is that these assumptions are made explicit. Therefore, the effects of these assumptions are quantifiable.

3.2.2. POTENTIAL FIELD METHOD: UNIVERSAL COKRIGING

The potential field method (Lajaunie, Courrioux, and Manuel, 1997) was used to combine tomographic orientations with contact points to estimate the geometry of soil layers. The method is based on universal cokriging and offers two main advantages, namely flexibility and objectivity. The method is flexible because it allows two non-collocated variables as input. In the present case, the contact points between soil layers are accurately known from CPTs and boreholes, but they are sparse. Meanwhile, the orientations of the soil layers are known in a horizontally-continuous manner from geophysical tomograms, but their location does not coincide with the contact points. The potential field method is also objective because it takes into account the input data sets explicitly.
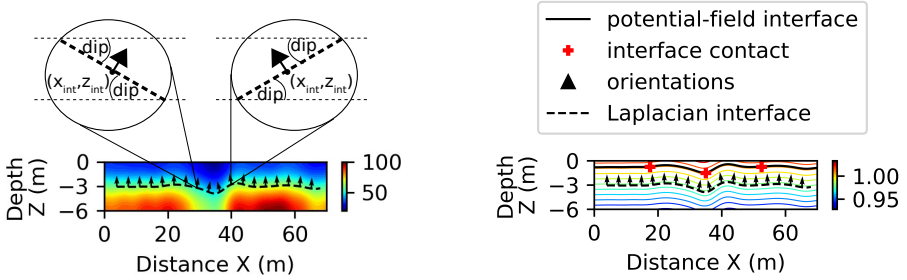
(a) Orientation of the soil layers (arrows) calculated from the dip of the edges (dashed line) detected in the geophysical tomography (contour plot).

(b) Potential field (contour lines) derived from the contact points between soil layers (crosses) and the tomographic orientations (arrows).

Figure 3.2: Tomographic orientations and potential field method.

Consequently, the effect of the data and the covariance model on the estimated geometry of the soil layers is quantifiable.

The method generates a potential field which is designated with the random function Z_1. The potential field represents a proxy to the time of formation. By this definition, the interface between two soil layers was formed at the same time. Also, the gradient of the potential field, $Z_2 = \nabla Z_1$, coincides with the orientations of the soil layers. The gradient points towards younger formations or later formation times. To formulate the cokriging system, the value of Z_1 and Z_2 needs to be known at certain locations. The gradient of the potential field, Z_2, is known from geophysical tomograms (arrows in Figure 3.2b). However, the value of the potential field is not known at the contact points (crosses in Figure 3.2b). Thus, it is convenient to replace the random function Z_1, which is not known at the contact points, by a new, known, random function defined as

$$Z_{1new}(x) = Z_1(x) - Z_1(x_0) = 0, \tag{3.4}$$

where x_0 is a reference contact point which belongs to the same interface as x. To illustrate, in Figure 3.2b, x_0 is the first contact point (leftmost red cross) so $Z_{1new}(x)$ is evaluated at the remaining two contact points. The choice of reference point has no influence in the cokriging estimation of the potential field $Z_1^*(x)$. The function Z_{1new} equals zero because the value of the potential field along an iso-surface is constant. The potential field method allows for any number of soil layers, but at least two contact points must be known per layer so that Z_{1new} is defined. The potential field is then generated via universal cokriging of Z_{1new} and Z_2. Because of the dependency between Z_1 and Z_2, the covariance and cross-covariance matrices are derived from a single covariance model, i.e., the covariance model of the potential field. The same is true for the drift functions. Following Varga, Schaaf, and Wellmann (2019), the cokriging system becomes

$$\begin{bmatrix} \mathbf{C}_{Z_{1\text{new}},Z_{1\text{new}}} & \mathbf{C}_{Z_{1\text{new}},Z_2} & \mathbf{U}_{Z_{1\text{new}}} \\ \mathbf{C}_{Z_2,Z_{1\text{new}}} & \mathbf{C}_{Z_2,Z_2} & \mathbf{U}_{Z2} \\ \mathbf{U}_{Z_{1\text{new}}}^T & \mathbf{U}_{Z_2}^T & \mathbf{0} \end{bmatrix} \cdot \begin{bmatrix} \boldsymbol{\lambda}_{Z_{1\text{new}},Z_{1\text{new}}} \\ \boldsymbol{\lambda}_{Z_2,Z_{1\text{new}}} \\ \boldsymbol{\mu}_{Z_{1\text{new}}} \end{bmatrix} = \begin{bmatrix} \mathbf{c}_{Z_{1\text{new}},Z_{1\text{new}}} \\ \mathbf{c}_{Z_2,Z_{1\text{new}}} \\ \mathbf{f}_{Z_{1\text{new}}} \end{bmatrix}, \qquad (3.5)$$

where $C_{Z_{1\text{new}},Z_{1\text{new}}}$, C_{Z_2,Z_2} are covariance matrices, $C_{Z_{1\text{new}},Z_2}$, $C_{Z_2,Z_{1\text{new}}}$ are cross-covariance matrices, $U_{Z_{1\text{new}}}$ and U_{Z_2} are drift functions, λ, μ are the cokriging weights, c are vectors which contain covariances and cross-covariances between the existing data points and the interpolation point, and $f_{Z_{1\text{new}}}$ is the vector which contains the drift function of $Z_{1\text{new}}$ evaluated at the interpolation point. The drift function and the relation between covariance and cross-covariance models are elaborated in (Lajaunie, Courrioux, and Manuel, 1997; Varga, Schaaf, and Wellmann, 2019). The potential field is estimated at any interpolation point in the domain from the cokriging weights

$$Z_1^*(x) = \sum_{\alpha=1}^{M} \boldsymbol{\lambda}_{Z_{1\text{new}},Z_{1\text{new}}} (Z_1(x_\alpha) - Z_1(x_0^\alpha)) + \sum_{\beta=1}^{N} \boldsymbol{\lambda}_{Z_2,Z_{1\text{new}}} Z_2(x_\beta) \qquad (3.6)$$

where M is the number of contact points minus the number of soil layers and N is the number of gradients which is a multiple of three. Although the contribution of $Z_{1\text{new}}$ in equation 3.6 is zero, $Z_{1\text{new}}$ contributes to the cokriging weights associated with Z_2.

The covariance models, which are needed to calculate the covariance matrices and vector in equation 3.5, can be derived experimentally or heuristically. Experimentally, the covariance models need to be derived from the orientation data (Aug, 2004; Chiles et al., 2004), for the potential field is a mathematical construction not known at the contact points. Since the relation between covariance models is known, the covariance models follow from the covariance model of the orientation data. Alternatively, a heuristic approach is often used to define the covariance models. Varga, Schaaf, and Wellmann (2019) assume a spherical covariance model for the potential field Z_1 where the variance and range of Z_1 define all the covariance and cross-covariance models in Equation 3.5. Default values for the variance and range of the covariance function are calculated based on the size of the model domain (Varga, Schaaf, and Wellmann, 2019). The estimation variance has no physical meaning when the covariance models are defined heuristically. In that case, the cokriging system can be solved in its dual form which improves computation efficiency (Goovaerts, 1997). The python package GemPy (Varga, Schaaf, and Wellmann, 2019) was used to apply the potential field method to the data presented.

Table 3.1: Parameters of the synthetic model.

Layer	Parameter	Value	Unit
Upper	Mean	10	$\Omega\,\mathrm{m}$
	Variance	2.25	$\Omega^2\mathrm{m}^2$
	Horizontal correlation length	5	m
	Vertical correlation length	0.5	m
Lower	Mean	40	$\Omega\,\mathrm{m}$
	Variance	36	$\Omega^2\mathrm{m}^2$
	Horizontal correlation length	5	m
	Vertical correlation length	0.5	m

3.3. PROOF OF CONCEPT

3.3.1. SYNTHETIC STUDY SITE AND DATA SIMULATION

The approach of Figure 3.1 was applied to a synthetic two-layer model with internal variability. The contact points between soil layers were obtained from sampling the subsurface at two locations. The orientations of the interface between soil layers were derived from three types of images, namely the true electrical resistivity model, an ERT tomogram, and an EMI tomogram. The geometry of the interface was estimated for each type of image with the potential field method. Finally, the estimated geometry was compared to the true geometry of the synthetic model.

Each layer of the synthetic model was simulated as a realization of a Gaussian random field via covariance matrix decomposition (Constantine, 2020). The random fields were characterized by an anisotropic covariance model

$$cov(x_1, x_2) = \sigma^2 \exp\left(-2\sqrt{\left(\frac{\tau_x}{\theta_x}\right)^2 + \left(\frac{\tau_z}{\theta_z}\right)^2}\right) \tag{3.7}$$

where τ_x and τ_z are the horizontal and vertical distances between the pair of points x_1 and x_2, σ^2 is the variance of the random field, and θ_x and θ_z are the horizontal and vertical correlation lengths, respectively. The parameters of the random fields are summarized in Table 3.1. The air-ground interface was considered flat and located at $z = 0\,\mathrm{m}$. The interface between the soil layers was located at

$$z(x) = \begin{cases} -0.75 - 0.75\sin(0.1\pi x - 3\pi) & \text{for } 30.0 < x < 40.0, \\ -0.75 & \text{otherwise.} \end{cases} \tag{3.8}$$

In this case, the position of the interface also corresponded to the thickness of the upper layer. The synthetic model served as the base for simulating geophysical data and also as a representation of a tomogram with perfect resolution. The ERT and EMI tomograms were constructed by simulating data acquisition on the synthetic model. The ERT tomogram was constructed with data simulated following a roll-along pattern. The EMI tomogram was constructed with EMI data simulated with the acquisition geometry of

Table 3.2: Parameters for ERT and EMI data simulation.

Method	Acquisition parameter	Value
ERT	Electrode separation	0.5 m
	Number of electrodes	72
	Number of electrodes rolled	36
	Number of rolls	2
	Array type	Wenner-alpha
	Total number of measurements	2088
EMI	Frequency	9000 Hz
	Separation from the ground	0.2 m
	Sampling spacing	0.5 m

the commercial device DUALEM-421. The simulation parameters for the ERT and EMI data sets are summarized in Table 3.2.

3.3.2. EDGE DETECTION: TRUE MODEL, ERT, AND EMI

Figure 3.3a shows the synthetic model and the Laplacian edge detection technique applied to it. The Laplacian of the true model shows a large number of zero-crossings which are a result of the internal variability within the soil layers. Meanwhile, the gradient shows high values at the location of the soil interface. The Laplacian and gradient magnitude sufficed to detect the interface between soil layers in the true model, so smoothing was not applied.

Figure 3.3b shows the edge detection technique applied to the original ERT tomogram. Visually, the ERT tomogram indicates the presence of two soil layers with internal variability. The zero-crossings of the Laplacian showed both true soil interfaces and fake edges. The fake edges arose from small-scale variability in the ERT tomography. Smoothing and thresholding were applied to improve the detection of edges in the tomogram. Figure 3.3c shows the ERT tomogram after a Gaussian filter with a standard deviation of 2.5 was applied. Although the filtered ERT tomogram was not visually different from the original tomogram, the small-scale zero-crossings were significantly fewer. Two geometrically similar edges were visible in the Laplacian of the filtered tomogram. The edge that corresponds to the soil interface was identified by thresholding the gradient magnitude.

Figure 3.3d shows the edge detection technique applied to the EMI tomogram. Visually, the EMI tomogram also indicates the presence of two soil layers. However, the contour plot of the unfiltered EMI tomogram resembles only roughly to the true interface geometry. Moreover, the Laplacian of the unfiltered tomogram is contaminated with small-scale zero-crossings, so the interface between soil layers is not visible. Thus, smoothing was applied. Figure 3.3e shows the EMI tomogram after a Gaussian filter with a standard deviation of 20.0 was applied. The remaining edge in the Laplacian is located

at the same position where the gradient magnitude is large.

3.3.3. Potential field: True model, ERT, and EMI

Figure 3.4a shows the potential field method applied to the data sets of the true model, the ERT, and the EMI tomograms. The data sets consist of contact points and orientations. The contact points between the soil layers were obtained from local point data of the subsurface, i.e., equation 3.8 sampled at $x = 23$ m and $x = 46$ m. The orientations were calculated as the dip angle of the Laplacian interfaces. The Laplacian interfaces are the edges detected with the Laplacian edge detection technique (Figure 3.3). They represent the interface between soil layers estimated with geophysical data only. The potential-field interfaces represent the interfaces estimated by combining geophysical data and local point data of the subsurface. The potential-field interfaces correspond to one of the contour lines of the potential field.

Figure 3.4b shows the error incurred by the Laplacian and the potential-field interfaces. The errors of the Laplacian and potential-field interface of the true model are negligible. Thus, sampling the subsurface is not necessary in the hypothetical case that the image of the subsurface is perfect. The added value of a combined approach for site investigation is visible when the image of the subsurface is approximate. In the ERT and EMI data sets, the error of the potential-field interface was smaller than that of the Laplacian interface. Thus, the combination of geophysics and local point data improved the estimation of geometric variability.
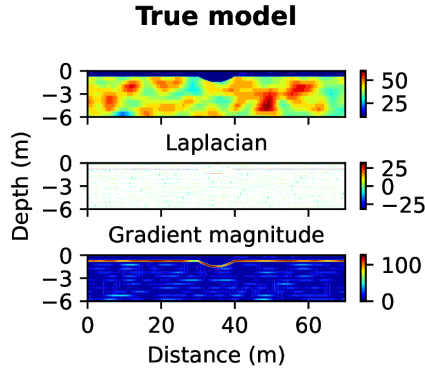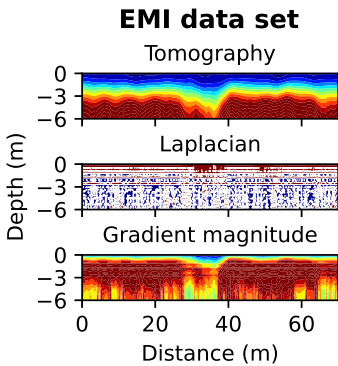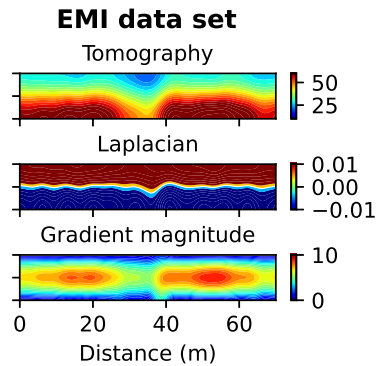
(a) Unfiltered synthetic model.
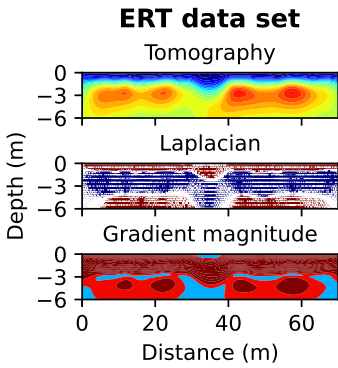
(b) Before filter.
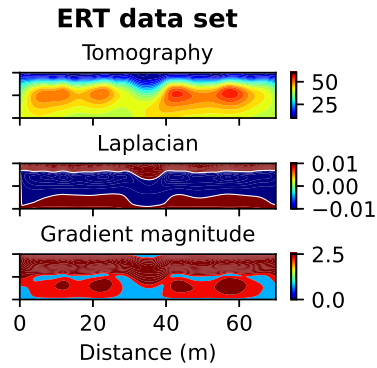
(c) After filter.

(d) Before filter.

(e) After filter.

Figure 3.3: Edge detection applied to three images of the subsurface, i.e., the true model, an ERT tomography, and an EMI tomography. The white lines represent the zero-crossings of the Laplacian operator.
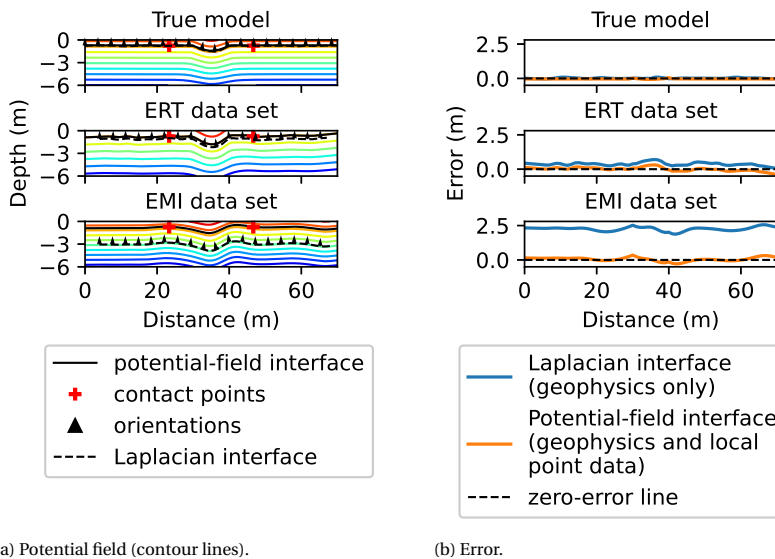
(a) Potential field (contour lines).   (b) Error.

Figure 3.4: Estimated interface geometry and error with the true model, ERT, and EMI tomography.

Table 3.3: Borehole data

Borehole ID	Distance (m)	Thickness (m)
BH0	168.00	-1.4
BH1	218.00	-1.5
BH2	81.16	-1.5
BH3	127.73	-0.8
BH4	177.90	-0.6
BH5	222.76	-0.9
BH6	273.94	-1.0
BH7	327.25	-1.1

3.4. APPLICATION IN AN ALLUVIAL ENVIRONMENT: MONTFOORT

3.4.1. STUDY SITE AND DATA COLLECTION

The case study site is located in the central-northern section of the Rhine-Meuse delta. In this alluvial environment, multiple paleochannels are present in the subsurface. These channels are visible in the present-day landscape as topographic ridges (Figure 3.5). Within this area, the Stuivenberg channel belt is the main topographic expression. Berendsen (1982) investigated comprehensively the geological development of the area. Additionally, Winkels et al. (2021) used local borehole data to gain insights into the internal build-up of the Stuivenberg channel belt and encasing sediments. Figure 3.5 shows an approximate lithological cross-section from Winkels et al. (2021). The cross-section shows the Stuivenberg paleochannel which mainly consists of sandy deposits. The channel is surrounded by clayey deposits and a Pleistocene sandy substrate. The geometric variability of the clay-sand interface was investigated at the location of the lithological cross-section. Since the clay layer is in contact with air, the depth of the clay-sand interface also represents the thickness of the clay layer.

The clay-sand interface was identified in boreholes from Winkels et al. (2021). The data set consisted of eight borehole cores (Table 3.3), each of which was sampled with a resolution of 0.1 m. The interface depths were determined by visual inspection. Tomographic images, collocated with the lithological cross-section, were created with ERT and EMI data. The ERT data were collected in spring 2018 with a Wenner-alpha array. The roll-along technique was used to cover the extent of the test site. The EMI data were collected in summer 2020 with a DUALEM-421 (Section 2.2.2). Table 3.4 summarizes the acquisition parameters for the ERT and EMI data. Clayey and sandy layers were recognized in ERT and EMI tomography by their value of electrical resistivity. In general, low values of electrical resistivity correspond to clayey layers while high values correspond to sandy layers.
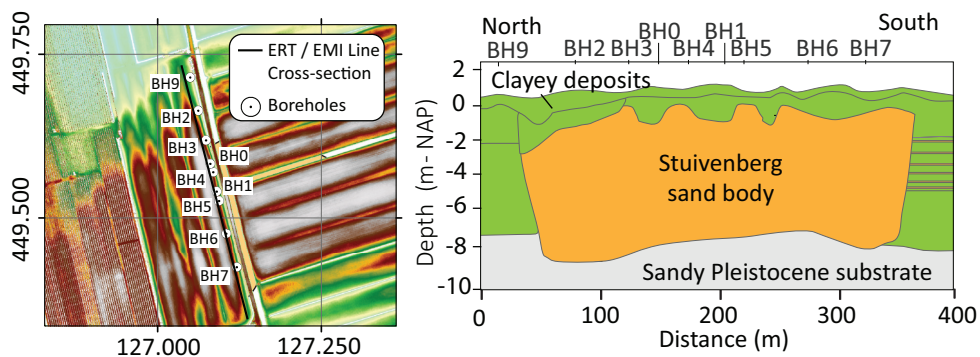
Figure 3.5: Elevation map of the study site (left) and lithological cross-section (right).

Table 3.4: Parameters for ERT and EMI data acquisition at the Montfoort site.

Method	Acquisition parameter	Value
ERT	Electrode separation	1.0 m
	Number of electrodes	72
	Number of electrodes rolled	36
	Number of rolls	11
	Array type	Wenner-alpha
	Total number of measurements	12051
EMI	Frequency	9000 Hz
	Separation from the ground	0.2 m
	Sampling spacing	1.0 m

3.4.2. Edge detection and interpretation: ERT and EMI tomography

Figure 3.6a shows the Laplacian edge detection technique applied to the ERT tomogram. The tomogram was filtered with a Gaussian filter at a standard deviation of 4.0. The value was chosen so that near-surface artefacts were reduced without distorting the tomogram. Due to the variability of the geological setting, multiple soil layers were detected in the Laplacian of the ERT tomogram. The interfaces that correspond to the layer of interest, the bottom of the clay layer in Figure 3.5, were picked from the edges detected in the tomogram. The picked edges showed a large value of gradient magnitude. Figure 3.6b shows the Laplacian edge detection technique applied to the EMI tomogram. The tomogram was filtered with a Gaussian filter at a standard deviation of 10.0. The value was chosen so that near-surface artefacts were reduced without distorting the tomogram. Although the EMI tomogram does not resolve the geological setting in the same detail as the ERT tomogram, similar insights were derived.

The clayey deposits on top of the Stuivenberg sand body (from approximately 60 m to 350 m in Figure 3.5) are thinner than the deposits on the sides of the sand body. On top of the sand body, the thickness of the clay layer varies at a smaller scale due to autogenic processes. For instance, BH1 and BH2 (Table 3.3), which are located on top of the sand body, show a thicker clayey layer than the surrounding boreholes. Small-scale variations are visible in both ERT and EMI tomograms. However, only the Laplacian of the ERT tomogram captures the details of the fine-scale variability. The Laplacian of the EMI tomogram does not capture this variability due to the lack of detail of the tomogram.

The lack of detail in the EMI tomogram is inherent to the device used in this survey, the DUALEM-421. Two factors affected the EMI tomogram. First, the measurements were collected during a dry summer day. Therefore, the electrical resistivity of the shallow portion of the ground was high due to evapotranspiration. Higher electrical resistivity values resulted in lower signal strength and thus lower resolution. Second, the maximum depth of investigation of the DUALEM-421 is approximately 6 m. Meanwhile, the thickness of the clay layer is known to be larger than 6 m on the left-hand side of the sand body. Therefore, the clay-sand interface in the EMI tomogram was only roughly visible on this side. On the right-hand side of the sand body, the thickness of the clay layer is known to be smaller than 4 m. Therefore, the clay-sand interface is more visible on this side.

3.4.3. Potential field: ERT and EMI

Figure 3.6g shows the potential field method applied the ERT data set of the Montfoort site. The estimated geometry of the clay-sand interface corresponds to one of the contour lines of the potential field. The method was applied with borehole data and ERT tomogram. The location of the clay-sand interface was derived from borehole data (Figure 3.6c) and the orientations were derived from ERT tomogram (Figure 3.6e). The estimated interface with the ERT data set captures in great detail the complexity of the lithological cross-section of the Stuivenberg channel belt.
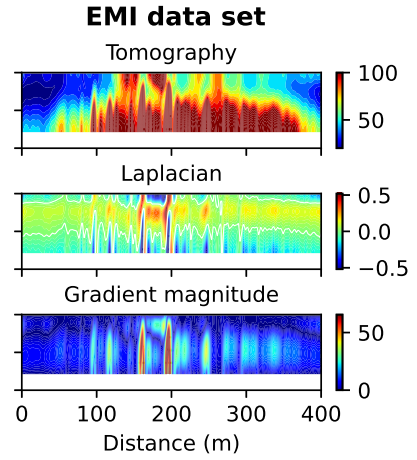
Table 3.5: Average depth of the clay-sand interface calculated with the potential field method applied to ERT and EMI data sets of the Montfoort site.

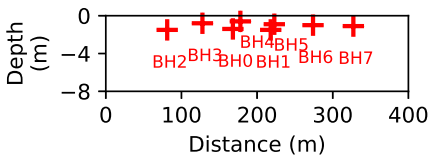| Zone	Initial x	End x	Method	Average
One	0.0	40.0	ERT	6.94
			EMI	5.50
Two	60.0	350.0	ERT	1.09
			EMI	1.26
Three	350.0	400.0	ERT	2.98
			EMI	2.53

The geometry of the clay-sand interface was also estimated with the EMI data set. For that purpose, additional information was manually added regarding the orientation of the clay-sand interface on top of the sand body. Although finer variability is visible in the EMI tomogram, the Laplacian edge detection technique was not successful at detecting variability in this region. Thus, we considered the clay layer on top of the sand body to be horizontal (Figure 3.6f). The orientations were positioned at the minimum depth found in the boreholes from Table 3.3 which is 0.6 m. Additionally, the data from a borehole core which is not listed in Table 3.3 was used (BH9 in Figure 3.6d). In the borehole core, which was drilled at $x = 30$ m, the Pleistocene sand layer was not reached after 5.5 m of drilling. Thus, the location of the clay-sand interface was conservatively estimated at a depth of 5.5 m. Figure 3.6h shows the potential field method applied to the EMI data set. To a lesser detail than the ERT tomography, the clay-sand interface was estimated with the EMI data set. On average, the clay-sand interface estimated with the ERT data set is comparable to that with the EMI data set (Table 3.5).
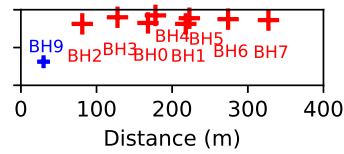
ERT data set

Tomography

EMI data set

Tomography

Laplacian

Laplacian

Gradient magnitude

Gradient magnitude
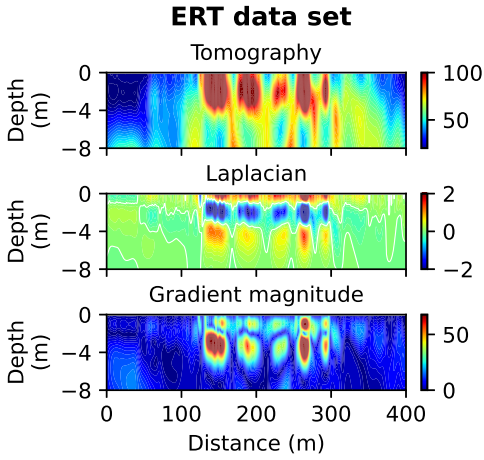
(a) Edge detection (ERT).

(b) Edge detection (EMI).

(c) Contact points.

(d) Contact points.
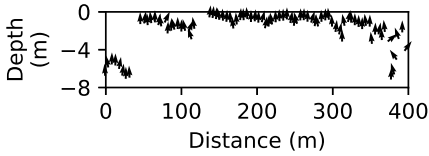
(e) Orientations.

(f) Orientations.

(g) Potential field (colored contour lines) and estimated interface (black line).

(h) Potential field (colored contour lines) and estimated interface (black line).

Figure 3.6: Application of the proposed approach to the data set of the Montfoort site. The white lines in a and b represent the zero-crossings of the Laplacian operator.

Figure 3.7: Elevation map of the study site and lithological cross-section.
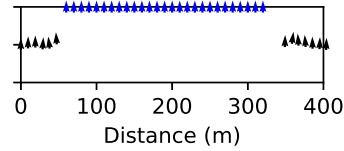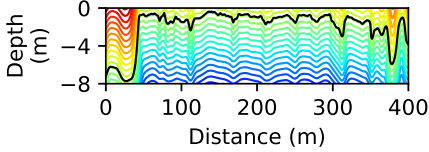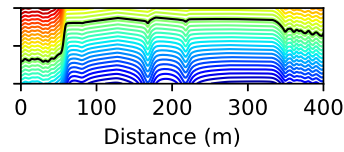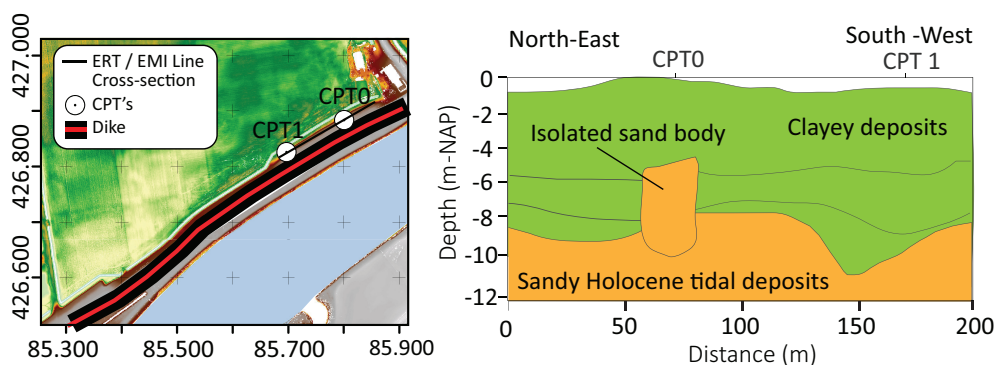
3.5. Application in a tidal environment: Dike 20-3

3.5.1. Study site and data collection

The site is a dike stretch which is part of the dike trajectory 20-3. The trajectory 20-3, which goes along with the Spui river, is part of the dike ring 20 Voorne-Putten in the Netherlands. The site is located in a tidal environment where tidal paleochannels are expected, but not always visible in elevation maps. The study site is a 200 m stretch of dike located in the hinterland of the dike. Figure 3.7 shows the elevation map of the study site and an approximate lithological cross-section. The cross-section shows a roughly homogeneous upper clayey layer underlain by a sandy Holocene layer. An isolated tidal paleochannel crosses both layers. The geometric variability of the clay-sand interface was investigated at the location of the lithological cross-section. As in Section 3.4, the depth of the clay-sand interface also corresponds to the thickness of the clay layer.

Local authorities have carried out extensive CPT investigation along the dike trajectory 20-3. Two CPTs were available at the location of the study site. The depth of the clay-sand interface was obtained from the Soil Behavior Type (SBT) index of the CPTs (Robertson, 2009). The interface between the upper and lower layer was defined the depth were the SBT index reached a value of 2.6 (Robertson, 2009). Tomographic images, coincident with the lithological cross-section, were created with ERT and EMI data. The ERT data were collected with a Wenner-alpha array. The roll-along technique was used to cover the extent of the test site. The EMI data were collected with a DUALEM-421. Table 3.6 summarizes the acquisition parameters for the ERT and EMI data. Clayey and sandy layers were recognized in ERT and EMI tomograms by their value of electrical resistivity. In general, low values of electrical resistivity correspond to clayey layers while high values correspond to sandy layers.

Table 3.6: Parameters for ERT and EMI data acquisition at the dike 20-3 site.

Method	Acquisition parameter	Value
ERT	Electrode separation	1.5 m
	Number of electrodes	72
	Number of electrodes rolled	36
	Number of rolls	2
	Array type	Wenner-alpha
	Total number of measurements	2946
EMI	Frequency	9000 Hz
	Separation from the ground	0.2 m
	Sampling spacing	1.0 m

3.5.2. Edge detection and interpretation: ERT, and EMI tomography

Figure 3.8a shows the Laplacian edge detection applied to the ERT tomogram of the study site. The tomogram was not filtered because small-scale artifacts were not strongly present. Multiple layers were detected in the Laplacian of the ERT tomogram. The tomogram shows a high resistivity top which is the dry part of the upper layer. After the dry part, the upper layer shows low resistivity. The layer after shows higher resistivity values. The variability of the clay-sand interface is visible in the Laplacian of the ERT tomogram (Figure 3.8a). Figure 3.8b shows the Laplacian edge detection applied to the EMI tomogram of the study site. To reduce small-scale artifacts, the tomogram was filtered with a Gaussian filter at a standard deviation of 10.5.

Although the depth of the EMI tomogram is shallower than that of the ERT tomogram, both tomographic images show comparable features. The tidal paleochannel of Figure 3.7, which is located from $x = 50$ m to $x = 100$ m, was captured in the ERT and EMI tomogram. In the ERT tomogram the paleochannel was fully captured while in the EMI tomography only the top was captured. The clay-sand interface is visible in the Laplacian of the ERT tomogram along the entire dike stretch. Meanwhile, the Laplacian of the EMI tomogram shows the clay-sand interface mostly at the location of the paleochannel intrusion. The penetration depth of the EMI survey device, DUALEM-421, was lower than the depth of the clay-sand interface on the sides of the paleochannel.

3.5.3. Potential field method with ERT and EMI

The potential field method was applied to the ERT and EMI data set. The CPTs were located at the top of the sand body intrusion and at the flat portion of clayey layer (Figures 3.8c and 3.8d). The clay-sand interface in CPT0 was located at a distance of 78.0 m and a depth of -1.5 m while the clay-sand interface at CPT1 was located at a distance of 178.0 m and a depth of -6.0 m. A fictitious interface at a distance of 25.0 m and depth of -6.0 m was added to the EMI data set (CPT2 in Figure 3.8d). The interface was added to enforce

Table 3.7: Average depth of the clay-sand interface calculated with the potential field method applied to ERT and EMI data sets of the Dike 20-3 site.

| Zone	Initial x	End x	Method	Average
One	10.0	40.0	ERT	4.82
			EMI	5.95
Two	50.0	90.0	ERT	2.08
			EMI	2.51
Three	125.0	200.0	ERT	5.45
			EMI	5.95

the clay-sand interface at this location to be similar to the interface at 178.0 m. The orientations derived from the ERT and EMI tomograms are shown in Figures 3.8e and 3.8f. Since the depth of the EMI tomogram captures the top of the sand body intrusion, but it does not reach the deeper sand layer. We manually added the orientations of the layer interface based on the interpretation of neighboring CPTs. We considered this layer to be horizontal. The orientations derived from the EMI tomogram and the manually-added orientations are shown in Figure 3.8f in black and blue, respectively. The estimated geometry of the upper clayey layer is shown in Figure 3.8g for the ERT data set and in Figure 3.8h for the EMI data set. The geometric variability of the clay-sand interface is captured by both data sets. On average, the clay-sand interface estimated with the ERT data set is comparable to that estimated with the EMI data set (Table 3.7).
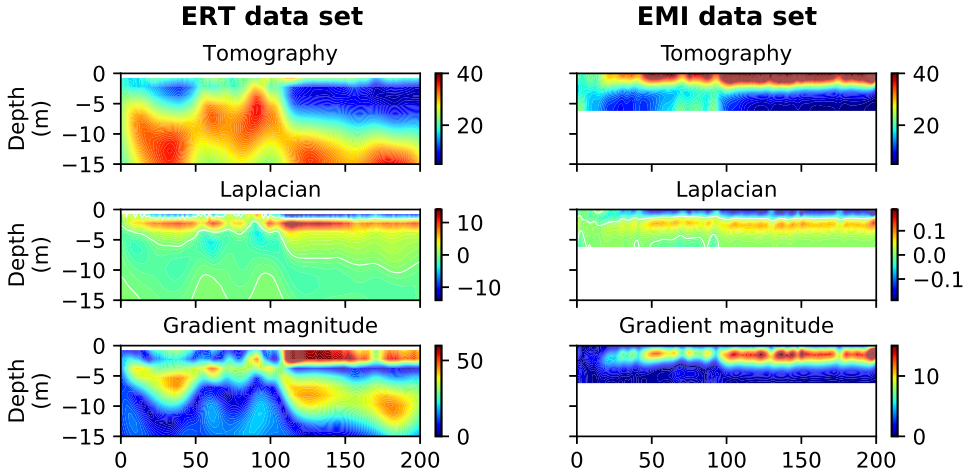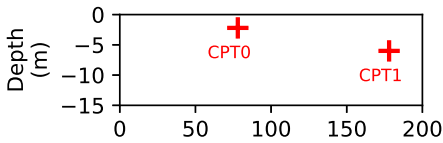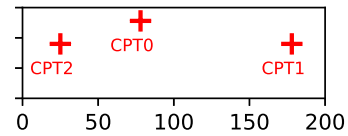
3

ERT data set

Tomography

Laplacian

Gradient magnitude

(a) Edge detection (ERT).

(c) Contact points.

(e) Orientations.

(g) Potential field (colored contour lines) and estimated interface (black line).

EMI data set

Tomography

Laplacian

Gradient magnitude

(b) Edge detection (EMI).
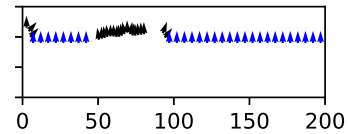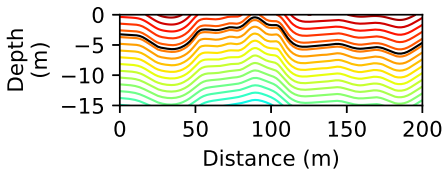
(d) Contact points.
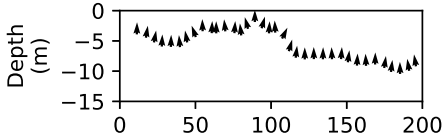
(f) Orientations.
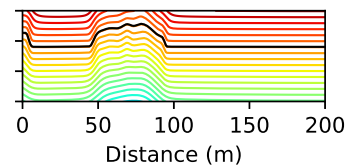
(h) Potential field (colored contour lines) and estimated interface (black line).

Figure 3.8: Application of the proposed approach to the data set of the dike 20-3. The white lines in a and b represent the zero-crossings of the Laplacian operator.

3.6. DISCUSSION

3.6.1. EDGE DETECTION IN A TWO-LAYER MODEL

A synthetic two-layer model is studied in this section with the ERT method. First, the impact of geophysical measurements in a tomographic image is studied. For that purpose, the analytical ERT response for a generic two-layer model is presented. Subsequently, the study is extended to particular cases of soil properties and acquisition designs. The synthetic responses from these particular cases are used to construct one-dimensional tomographic images. Finally, the performance of the Laplacian edge detection on these images is studied.

Figure 3.9 shows the apparent resistivity response for a Wenner-alpha array in a horizontal two-layer model. The apparent resistivity is normalized with respect to the resistivity of the upper layer. The apparent resistivity contour is plotted with respect to the normalized electrode spacing, a/h, and the resistivity contrast

$$k_\rho = \frac{\rho_2 - \rho_1}{\rho_2 + \rho_1}. \qquad (3.9)$$

The normalized electrode spacing, a/h, determines the sensitivity of the measurement in depth. A measurement with a small value of a/h is more sensitive to the resistivity of the upper layer. Meanwhile, a measurement with a large value of a/h is more sensitive to the lower layer. An acquisition array should contain small and large values of a/h so that the upper layer and lower layers are properly detected. The optimum range of a/h values will depend on the resistivity contrast, k_ρ. At a given contrast (white dashed lines in Figure 3.9), the range of a/h values has to be such that the resistivity response is properly sampled. In other words, an acquisition array should cross the contour lines in Figure 3.9 from $\rho_a/\rho_1 = 1$ to $\rho_a/\rho_1 = \rho_2/\rho_1$. Operational limitations regarding data acquisition and lack of geological knowledge, make comprehensive data acquisition difficult to achieve in practice. Thus, the measured data contain incomplete geological information which affects the tomogram.

A particular two-layer model with $h = 1.5\,\text{m}$ and $\rho_1 = 10\,\Omega\,\text{m}$ is further analyzed. Two resistivity contrasts are analyzed, namely $k_\rho = 0.2$ and $k_\rho = 0.6$ which result in $\rho_2 = 15\,\Omega\,\text{m}$ and $\rho_2 = 40\,\Omega\,\text{m}$, respectively. Figure 3.10 shows the noise-free apparent resistivity response for each resistivity contrast. For tomographic inversion, four cases are considered each with 23 measurements. The base electrode spacing, a, for each case is 0.25, 0.5, 1.0, and 3.0 m. Due to the limited number of measurements, the apparent resistivity response is not fully reconstructed in the measurements. The portion of the response that is covered in each case is shown at the bottom of Figure 3.10. At $a = 0.25\,\text{m}$, the response is more sensitive to the upper layer than the lower layer. At $a = 0.5\,\text{m}$ and $a = 1.0\,\text{m}$, the apparent resistivity is sensitive to both layers. Even though the measurements do not reconstruct the complete apparent resistivity response, the trend of the response is well captured. At $a = 3.0\,\text{m}$, most of the measurements are sensitive to the lower layer while few measurements are sensitive to the upper layer.

The synthetic apparent resistivity data were contaminated with Gaussian random

noise of 2% before tomographic inversion. The value follows the guideline of the report for Best Practices in Electrical Resistivity Imaging (Day-Lewis et al., 2008). Figure 3.11 shows the Laplacian edge detection technique applied to the tomographic images obtained for $k_\rho = 0.2$ and $k_\rho = 0.6$. The figure shows the tomographic images and edge detection before and after a Gaussian filter was applied. The chosen standard deviation for the filter was $5.5\,\Omega\,\mathrm{m}$. Most of the inverted models reproduce the trend of variability of the true model. However, the inverted models at low resistivity contrast, $k_\rho = 0.2$, are more affected by the added noise than the inverted models at high resistivity contrast, $k_\rho = 0.6$. This fact is reflected in the undulations of the inverted models which result from over fitting the data during tomographic inversion. In general, a combination of low resistivity contrast and non-optimum data acquisition is detrimental to the reliability of tomograms for geological interpretation. However, no exact limit can be drawn. For example, the inverted model for $k_\rho = 0.6$ and $a = 3.0\,\mathrm{m}$ shows a clear mismatch between the true and inverted resistivity values even though the contrast is high. On the other hand, all the inverted models for $k_\rho = 0.2$ reproduce the trend of electrical resistivity. A sensible criterion to assess the reliability of a tomographic image is that layers that are visible in the tomogram should also be visible in the raw data. In other words, the measured response should match that of a conceptual lithological cross-section.

Figure 3.11 shows Laplacian edge detection technique applied to one-dimensional tomographic images for $k_\rho = 0.2$ and $k_\rho = 0.6$. The automated edge detector finds edges in the tomographic images even when there are no geological interfaces. The so-called fake edges are more often found when small-scale artefacts are present in the tomography. For instance, fake edges are more frequent for $k_\rho = 0.2$ because of the undulated pattern of the inverted models. In Figure 3.11, a smoothing Gaussian filter reduced the undulations of the tomographic images significantly and therefore fake edges. At the same time, the filter kept intact the large-scale trend of resistivity values. Fake edges were further reduced by setting a threshold on the gradient. The tomography and edges detected after filtering, and thresholding agree with the resistivity trend and the interface location of the true model. However, the locations of the tomographic interfaces do not precisely coincide with that of the true model. Hence, the potential field method (Lajaunie, Courrioux, and Manuel, 1997) is essential to calibrate the tomographic data with more accurate information obtained from direct samples of the subsurface.
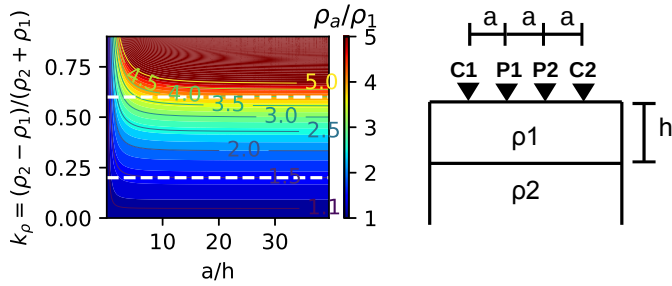
3

Figure 3.9: Generalized apparent resistivity response for a two-layer model and a Wenner-alpha array.
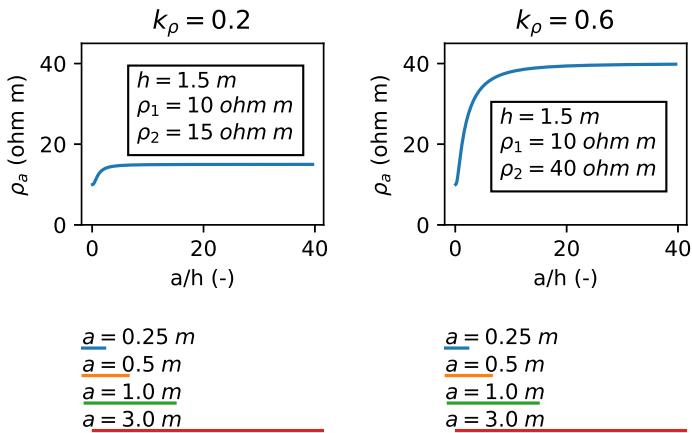

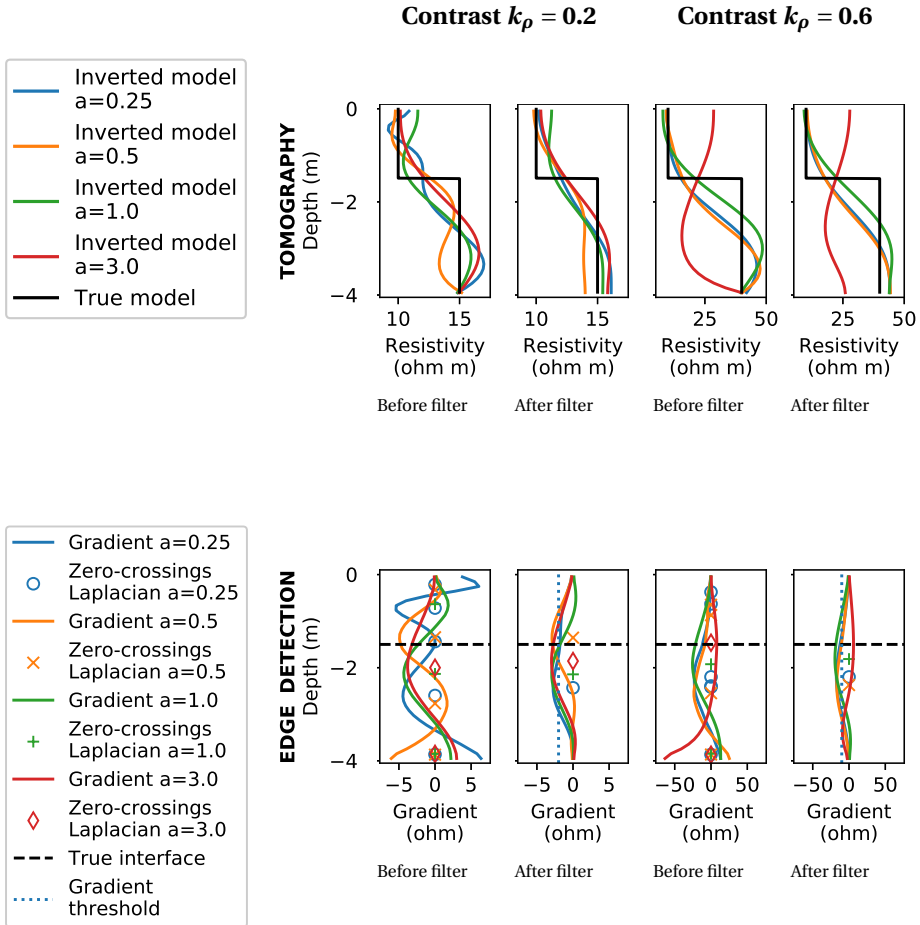Figure 3.10: Particular apparent resistivity response for a two-layer model and a Wenner-alpha array.

Figure 3.11: Edge detection applied to one-dimensional tomographic images before and after a smoothing Gaussian filter was applied.

3.6.2. IMPLICATIONS FOR THE RELIABILITY ASSESSMENT OF DIKES

In the Netherlands, stochastic subsurface models were developed for the reliability assessment of primary dikes (Hijma and Lam, 2015). The models were created based on an extensive database of local point data and geological knowledge of the Rhine-Meuse delta. Despite the large amount of available information in the Netherlands, uncertainties remain in the subsurface models. The main source of uncertainty is the sparsity of the data relative to the geological variability. To account for uncertainty in reliability assessments, geological experience is often used. For instance, a probability of occurrence is assigned to a geological scenario even though that scenario is not found in site investigation data (ENW, 2012). Such geological scenarios could lead to over conservative reliability assessments. To discard or confirm this type of geological scenarios, it is necessary to reduce data sparsity. Geophysical exploration methods are a powerful tool in this regard because they provide a horizontally-continuous view of the subsurface. In this research, the geometric variability of soil layers was studied. The geometry of soil layers is an important part in the reliability assessment of dikes especially for the failure mechanisms of piping and macrostability. The approach presented here aims at improving the characterization of geometric variability in two ways. First, by showing that geophysical exploration can improve the allocation of site investigation efforts. Second, by improving the estimated geometry of soil layers with a reduced amount of local point data.

Geophysical exploration can improve the allocation of site investigation efforts by providing a view of the average composition of the subsurface. For example, the geophysical images in Sections 3.4 and 3.5 (Figures 3.6 and 3.8) show the regions of the subsurface where the geometry of soil layers varies due to the presence of paleochannels. Indeed, anomalies, such as paleochannels, are a large source of uncertainty in reliability assessments because they are easily missed in local point data (ENW, 2012). Elevation maps are a valuable source of information to visually detect paleochannels (Berendsen and Volleberg, 2007). However, small paleochannels, e.g. Section 3.5, are more challenging to detect in elevation maps. Then, geophysical methods can fill the information gap between local point data. A common problem of geophysical exploration is that the data interpretation is often subjective and relies on expert knowledge. Thus, an automatic edge detector was applied to the geophysical images so that the interpretation is objective and reproducible without expert knowledge. The information retrieved from geophysical data is valuable for assisting the allocation of site investigation efforts. For example, by indicating the location and extent of anomalous features, such as paleochannels.

Apart from assisting exploration efforts, geophysical data improves subsurface characterization when combined with local point data. In particular, the estimation of geometric variability is improved. To elaborate, we consider the estimation error of the ERT data set of the Montfoort site. Figure 3.12 shows the estimation error of the Montfoort site. The left-hand side of the plot shows the absolute error per borehole. The right-hand side shows the overall density distribution of the Montfoort site. The absolute error in Figure 3.12 was calculated using the contact points measured in boreholes (Table 3.3)

as the reference truth. Figure 3.12a shows the error incurred when only the Laplacian interface of the ERT tomogram is used for the interface estimation. In this test site, there is a good agreement between the Laplacian and borehole interface. Indeed, the density distribution of the error is narrow with few outliers. Figures 3.12b and 3.12c show that the estimation of geometric variability improves when geophysical and borehole data are combined via the potential field method. The error in Figure 3.12b was calculated by removing one borehole at a time from the estimation procedure and using that borehole for validation, namely cross-validation. The median of the error in Figure 3.12b is reduced significantly and the overall density distribution of the error is narrow. The estimation with a combined data set shows consistency even when the number of boreholes is reduced. Figure 3.12c shows the cross-validation error when half of the boreholes are used in the estimation. The figure shows that the median of the error remains low and the density distribution remains narrow. Figure 3.12c shows more data points because there are several possible combinations to remove four boreholes.
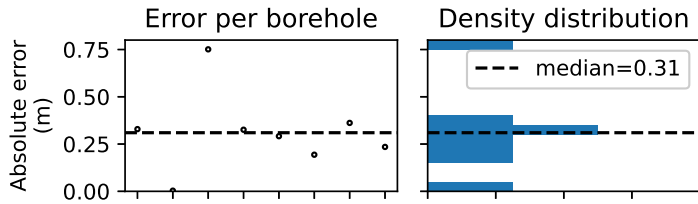
(a) Laplacian (ERT geophysics only).
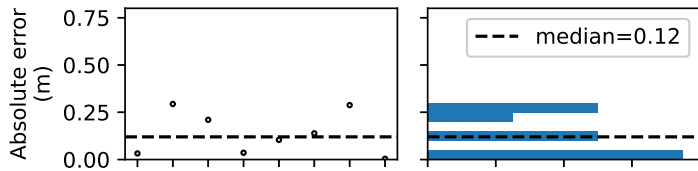
(b) Potential field with seven boreholes (ERT geophysics and boreholes).
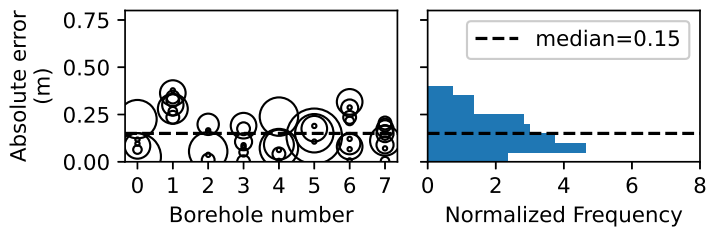
(c) Potential field with four boreholes (ERT geophysics and boreholes).
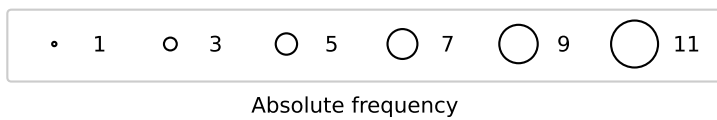
Figure 3.12: Error statistics Montfoort.

3.7. CONCLUSIONS

An approach to estimate the geometry of soil layers with the aid of geophysical tomograms was presented. The approach addresses the sparsity problem existing in the reliability assessment of dikes, i.e, the mismatch between site investigation density and geological variability. The approach provides a two-fold quantitative framework to incorporate geophysical information into geological schematizations. First, an automatic edge detection technique allows for objective and reproducible interpretation of geophysical exploration data. Second, a cokriging framework allows for objective incorporation of geophysical and local point data to estimate the geometric variability of soil layers. The resulting estimation is improved even when a reduced amount of local point data is available. In addition to this, geophysical data showed to be a valuable tool for assisting the allocation of site investigation efforts.

The approach presented in this study compared the data from two geophysical methods, namely ERT and EMI. The ERT method showed a detailed description of the subsurface. To a lesser detail than the ERT method, the EMI method also showed the main features of the subsurface, such as the presence of paleochannels. From an operational point of view; however, the EMI method is a more viable method for exploring the subsurface of dikes, for it can cover wide areas in a fraction of the time required with the ERT method.

Looking at the geophysical data beyond the geometry of soil layers, it is clear that a larger degree of complexity is captured in the geophysical data. The challenge is to retrieve quantitative information from this data for geotechnical applications. Geophysical insights are needed in terms of, for example, the internal correlation structure of soil layers.

4

INTERNAL VARIABILITY OF SOIL LAYERS

In Chapter 4, a method to estimate the horizontal correlation structure of geotechnical properties from geophysical tomograms is presented. In this method, the effectiveness of geophysical properties to make predictions about geotechnical properties is quantified. The uncertainty introduced by tomographic inversion is also quantified. The method was applied in a test site to estimate the correlation structure of the CPT cone resistance from a surface-based ERT tomogram. In this test site, the ERT-based correlogram showed a favorable comparison to the correlogram estimated directly from a dense grid of CPTs. Further analysis suggests that surface-based ERT can be a efficient alternative method to estimate the horizontal correlation structure of geotechnical properties.

The contents of this chapter are going to be submitted to the journal Georisk: Assessment and Management of Risk for Engineered Systems and Geohazards.

4.1. INTRODUCTION

The spatial variability of soil properties plays a significant role in the assessment of structural reliability of geotechnical infrastructure, but it is not routinely accounted for in geotechnical design and assessment. The spatial variability of properties is important as failure occurs along the path of least resistance (Fenton, Naghibi, and Griffiths, 2016). CEN (2004) recommends a cautious estimate of characteristic values to deal with the total uncertainty in soil properties. Inner variability of soil properties is a component of the total uncertainty together with, measurement uncertainty, transformation uncertainty, and statistical uncertainty (Prästings, Spross, and Larsson, 2019). In geotechnical practice, characteristic values of strength are estimated from the underlying distribution of strength. That is, spatial variability is not accounted for in the inner variability of soil properties. A value that accounts for spatial variability should come from the effective distribution of strength along the failure path (Orr, 2017). That is, the inner variability of soil properties should be reduced by a factor that accounts for spatial variability in the geotechnical reliability assessment. A key reason to neglect spatial variability is the difficulty to estimate the spatial correlation structure of the soil, i.e., correlogram. Sample data are scarce in geotechnical projects, and especially in the horizontal direction, rarely enough data are available to make reliable estimates of the correlogram. Geophysical methods are promising site investigation tools to efficiently reduce information scarcity and to facilitate the estimation of the correlogram in the horizontal direction. However, the peculiarities of geophysical data must be considered if geotechnical property estimations are to be made from geophysical data. Regardless, geotechnical practice could benefit from an efficient alternative method to estimate the correlation structure of soil properties.

The spatial variability of strength properties determines the type of failure of a geotechnical structure and influences the selection of characteristic values. Three types of failure are recognized (CEN, 2004; Hicks, 2013), with two extremes being local failure and global failures. Global failure occurs when strength properties are correlated at short distances. Then, the strength along the weakest path is given by the mean material property. Meanwhile, local failure occurs when strength properties are correlated at large distances. Then, the strength along the weakest path is given by the underlying strength distribution. The third failure type is influenced by strength properties correlated at intermediate distances. Thus, the strength along the weakest path is given by an effective strength distribution. As failure is attracted to weak zones, the mean of the effective distribution is reduced with respect to the underlying distribution (Hicks, 2013). In addition, the variance of the effective distribution is also reduced as the strength is averaged along the weakest path (Orr, 2017). It is important to note that the mean and variance reduction of strength is problem-specific (Vanmarcke, 1983; Hicks, 2013), with the correlogram being a key component of the effective distribution. The correlogram can guide the selection of characteristic values so that the behavior of geotechnical structures at failure is more accurately estimated. Studies with the Random Finite Element Method (RFEM), which explicitly incorporate the correlogram, have shown that characteristic values selected from the underlying distribution are overly conservative (Hicks et al., 2019; Varkey et al., 2020). Nevertheless, the benefits of accounting for spatial variability are left behind in

geotechnical practice because of the difficulty to measure the correlation structure.

The correlogram is difficult to estimate because of the highly variable nature of the subsurface and the effort required to obtain data points for the estimation. This difficulty is accentuated in the horizontal direction because typical site data mainly consist of vertical samples. For example, a Cone Penetration Test (CPT) records data with high vertical resolution, but typically due to the limited number of CPTs in a given project, few, low-resolution, data points are available in the horizontal direction. Thus, the correlogram can more reliably be estimated in the vertical direction than in the horizontal direction. Even though the correlation length is expected to be larger in the horizontal direction than the vertical direction, the high variability of the subsurface introduces variation in the estimation of the correlogram even in densely sampled sites. For instance, Gast, Vardon, and Hicks (2021) and Lloret-Cabot, Fenton, and Hicks (2014) show that a major drop in spatial correlation takes place at distances smaller than the minimum separation between horizontal samples. Surface-based geophysical images, i.e. tomograms, are promising tools to improve estimations in the horizontal direction as they map the subsurface in a horizontally-continuous manner with little to no disturbance. However, the use of geophysical methods for the estimation of geotechnical properties presents two main challenges. First, geophysical methods do not map geotechnical properties directly. Thus, the utility of tomographic images largely depends on the strength of the relationship between the geotechnical and the geophysical property. Second, geophysical tomograms are smooth representations of the subsurface (Menke, 2012). Thus, the correlogram of the tomogram is also affected by smoothing (Day-Lewis, 2005). To estimate the correlogram for a geotechnical property from a geophysical tomogram, both aspects must be addressed.

The use of geophysical images introduces transformation uncertainties in the estimation of the correlogram of geotechnical properties. The transformation uncertainty originates from the imperfect relationship between geotechnical and geophysical properties. Thus, the strength of the relationship determines the effectiveness of the estimation of one property from the other (Journel, 1999). In hydrogeology, geophysics has been largely used to quantitatively characterize the spatial variability of hydraulic properties because of the strong relationship between hydraulic conductivity and geophysical properties (see Binley et al. (2015) and references therein). A strong relationship exists because bulk physical properties, such as electrical resistivity and hydraulic conductivity, are related to pore-scale properties, such as porosity (Lesmes and Friedman, 2005). In contrast, in geotechnical applications, geophysical methods have been used mainly to distinguish geological facies (Hermans and Irving, 2017; Olalla et al., 2021), which does not require the formulation of quantitative relationships between geotechnical and geophysical properties. Nevertheless, quantitative relationships could be derived because geotechnical strength properties are also related to pore-scale properties, especially porosity. For example, the cone resistance of a CPT increases with sand content (Robertson, 2009) as well as the electrical resistivity (Singha et al., 2015). The rapid development of sensors for in-situ site investigation (Hicks, Pisano, and Peuchen, 2018) opens up the possibilities for quantitative analysis of geophysical data for geotechnical

purposes. A sensor that has been available for decades in geotechnical site investigation is the electric CPT (Campanella and Weemees, 1990; Daniel et al., 1999) which measures the point-scale electrical resistivity alongside standard CPT values. This type of sensor allows for the efficient development of in-situ relationships of site-specific geophysical and geotechnical properties, and avoid time-consuming laboratory investigations.

Geophysical images introduce uncertainties in the estimation of the correlogram due to tomographic inversion. That is, tomograms average out fine details of the sub-surface (Day-Lewis, 2005). A variety of approaches have been used to overcome this shortcoming of tomographic data. Hubbard, Rubin, and Majer (1999) used a spectral approach to complement the low-frequency content of cross-hole tomograms with the high-frequency content of vertical borehole samples. The combined frequency content resulted in an accurate estimation of the vertical correlation structure. In the horizontal direction, such methodology is not applicable because horizontal samples are collected at a coarser spacing than the tomographic cell size. Another approach to overcome to-mographic smoothness is to incorporate a correlation model in the inversion process (Hermans et al., 2012; Ruggeri et al., 2013). This approach enhances natural heterogene-ity in the tomogram but assumes the correlation structure to be known. In reality, tomo-graphic smoothing removes subsurface details that cannot be traced back with geophys-ical data only. Therefore, the uncertainty introduced by the tomogram in the correlation structure must be estimated. Geostatistical inference has been applied to estimate un-certainty in geophysical problems (Looms et al., 2010; Irving, Knight, and Holliger, 2009; Hansen, Looms, and Nielsen, 2008; Day-Lewis, Lane, and Gorelick, 2006). The method compares the response of different possible scenarios to the actual measured response in the field. In this case, the possible scenarios are defined by the tomographic correl-ograms of the subsurface, and the response is the tomographic correlogram of the field data. By comparing the conceptual and field correlograms, unlikely scenarios are dis-carded. More importantly, overlapping scenarios represent the uncertainty introduced by tomographic inversion.

We present a framework to estimate the horizontal correlation structure, i.e. correl-ogram, of geotechnical properties from surface-based geophysical tomograms. In this framework, we quantify the effectiveness of geophysical properties to make predictions about geotechnical properties. We also quantify the uncertainty introduced by tomo-graphic inversion in the estimation of the correlation structure. The paper starts with a general methodology to estimate a correlogram from experimental data followed by the framework to estimate the horizontal correlogram of geotechnical properties from geophysical tomograms. The framework is then applied in a test site to estimate the hor-izontal correlogram of the CPT cone resistance from an ERT tomogram. The ERT-based correlogram showed a favorable comparison to the correlogram estimated directly from a dense grid of CPTs.

4.2. METHODS

A framework is presented to estimate the horizontal correlation structure, i.e. correlogram, of a geotechnical property, y, using the tomogram of a geophysical property, g. This section starts with a general methodology to estimate the correlagram from experimental data (Section 4.2.1). The methodology is applicable to vector data, such as CPTs, or matrix data, such as tomograms. Afterwards, the effectiveness of g to predict the correlogram of y is quantified (Section 4.2.2). The effectiveness of the prediction is hindered by the imperfect relationship between y and g, i.e. the correlation coefficient r_{yg}. Finally, the uncertainty introduced by tomographic inversion in the estimation of the correlogram is quantified with geostatistical inference (Section 4.2.3).

4.2.1. ESTIMATION OF THE EXPERIMENTAL CORRELOGRAM

Soil properties in natural and antropogenic deposits show spatial correlation over different scales. The experimental correlogram, $\hat{\rho}(\tau)$, describes that correlation as a function of separation lag, τ. For a vector x of equally-spaced samples of a soil property, the experimental correlogram is defined as an expectation (Wackernagel, 2003)

$$\hat{\rho}(\tau_i) = \frac{1}{\hat{\gamma}(0)(k-l)} \sum_{j=1}^{k-l} (x_j - \hat{\mu}(x_j))(x_{j+l} - \hat{\mu}(x_{j+l})), \qquad (4.1)$$

where $\hat{\gamma}(0)$ is the variance of x, k is the number of data points in x, and l is the number of bins that make a lag τ_i. The trend of the data $\hat{\mu}$ is removed from x in Equation 4.1 to ensure stationarity. The experimental covariance, $\hat{\gamma}(\tau)$, is related to the experimental correlogram, $\hat{\rho}(\tau)$, via the experimental variance

$$\hat{\gamma}(\tau) = \hat{\gamma}(0)\hat{\rho}(\tau). \qquad (4.2)$$

The experimental data in this study come from CPTs and surface-based tomograms. A CPT is a vector of vertical samples of the subsurface. Because of the limited number of CPTs available in a given project, the information in the horizontal direction is often scarce and sparse. In this study, a large number of CPTs were available, so the horizontal correlogram could also be estimated from the CPT data. In that case, the CPTs form a matrix of horizontal and vertical samples. Likewise, a surface-based tomogram is a matrix of horizontal and vertical samples. Since tomographic resolution decreases with depth, tomograms were used only to calculate the horizontal correlogram of the uppermost soil layer. In either data set, the experimental correlogram in each direction was calculated as an average of experimental correlograms. For example, the vertical correlogram is the average of the correlograms of each column of the data matrix. Because the correlogram is an expectation, the reliability of the experimental correlogram depends on the number of samples used to build it at a certain lag.

Correlation models are used to describe experimental correlograms so that metrics of spatial variability can be derived. Correlation models are defined by a correlation length that is, loosely speaking, the length within which properties are correlated. Strictly

speaking, the correlation length is an integral property of the correlation model (Vanmarcke, 1983)

$$\theta = 2 \int_0^\infty \rho(\tau).$$

Therefore, the correlation length is a property of the correlation model and not of the experimental correlogram. Thus, the correlation length depends on the choice of correlation model and the fitting procedure of the experimental correlogram to the model. Nevertheless, the correlation length is a useful metric to quantify spatial variability in an experimental data set. We chose a Markov correlation model because it best represented the data presented in this paper. In the Markov correlation model

$$\rho(\tau) = \exp(-2\tau/\theta), \tag{4.3}$$

the correlation length is the length at which the correlation drops to 0.135. Soil deposits show different correlation lengths in the horizontal and vertical directions (Nie et al., 2015). Therefore, Equation 4.3 was applied to model the experimental correlogram in each direction separately.

The correlation model that best fit the data is defined by the value of θ that minimizes the difference between the experimental and model correlogram. Since the number of samples reduces with increasing lag, the stability of the experimental correlogram at large lags becomes an issue in the minimization process. An possible solution to this problem is to limit the bins of the experimental correlogram that are used in minimization. We chose an alternative approach that consists in assigning weights to the minimization function. Therefore, the correlation model was obtained by finding the value of θ that minimizes the cost function

$$\phi = \sum_{i=1}^n w_i(\hat{\rho}(\tau_i) - \rho(\tau_i)) \tag{4.4}$$

where the weight w_i is the number of data points used to build the experimental correlogram at lag τ_i, and n is the number of lags in the experimental correlogram.

4.2.2. EFFECTIVENESS OF GEOPHYSICAL DATA TO PREDICT GEOTECHNICAL PROPERTIES

The strength of the geophysical-geotechnical relationship determines the degree of geotechnical spatial variability that can be explained with geophysical data. The relationship between a geotechnical property, y, and a geophysical property, g, is complex and often non-linear (Rubin, Mavko, and Harris, 1992; Schon, 2015). However, the variance within homogeneous soil deposits is small enough that a linear relationship can be assumed (Hubbard, Rubin, and Majer, 1999). Therefore, to quantify the relationship between correlation structures and the effectiveness of the geophysical data, a linear relationship is assumed between the stationary components of y and g (Figure 4.1 left)

$$y = m_{\text{yg}} g + b \tag{4.5}$$

where m_{yg} and b are the slope and the vertical intercept of the linear relation, respectively. The relationship between the covariances γ_y and γ_g follow from the expectation of Equation 4.5

$$\gamma_y(\tau) = m_{yg}{}^2 \gamma_g(\tau). \tag{4.6}$$

In Equation 4.6, the covariance function of y is proportional to that of g. Equation 4.6 is expanded with Equation 4.2 to quantify the relationship between correlograms

$$\gamma_y(0)\rho_y(\tau) = m_{yg}^2 \gamma_g(0)\rho_g(\tau).$$

The slope of the relationship, m_{yg}, is related to the correlation coefficient, r_{yg}, through the variances of y and g (Rodgers and Nice, 1988)

$$\gamma_y(0)\rho_y(\tau) = r_{yg}^2 \frac{\gamma_y(0)}{\gamma_g(0)} \gamma_g(0)\rho_g(\tau)$$

which results in a Markov cross-correlation model of type 2 (Journel, 1999)

$$\rho_y(\tau) = r_{yg}^2 \rho_g(\tau). \tag{4.7}$$

Equation 4.7 states that the correlogram of g explains only a fraction of the correlogram of y and that fraction is given by the correlation coefficient r_{yg}^2 (Figure 4.1 middle). In sum, the correlogram of y has a component that can be predicted by g and one that cannot because it is not spatially cross-correlated to g

$$\rho_y(\tau) = r_{yg}^2 \rho_g(\tau) + (1 - r_{yg}^2)\rho_r(\tau). \tag{4.8}$$

The correlation coefficient, r_{yg}, and the correlogram, ρ_g in Equation 4.8 need to be estimated from field data. On the other hand, the correlogram of the residual variance, ρ_r, cannot be estimated from the geophysical data. A possibility is to assume that ρ_r has the same correlation structure as ρ_g. Another possibility is to assume that ρ_r is a nugget, which in turn could be estimated from the vertical data which is more abundant. A combination of both possibilities seems to be a sensible choice. In geotechnical projects, r_{yg} could be efficiently estimated from CPT data. For example, the electric CPT measures electric resistivity alongside geotechnical properties (Campanella and Weemees, 1990; Daniel et al., 1999). However, small-scale data, i.e. CPTs, could lead to an underestimation of the relationship between y and g (Shmaryan and Journel, 1999). This point is further elaborated in Section 4.4.4. Finally, to estimate ρ_g, horizontally-continuous samples of g are needed. In this study, we use geophysical tomograms to obtain those samples. Because a tomogram $\bar{g}$ is an approximate representation of g, the correlogram of the tomogram $\rho_{\bar{g}}$ is different from the correlogram ρ_g (Figure 4.1 right). The difference stems from the averaging of fine details that is present in geophysical tomograms which tend to deform the correlogram of tomograms towards larger correlation lengths (Day-Lewis, 2005). The deformation of the tomographic correlogram introduces uncertainties in the estimation of the true correlogram ρ_g. That uncertainty is quantified in the next section in terms of the correlation length.
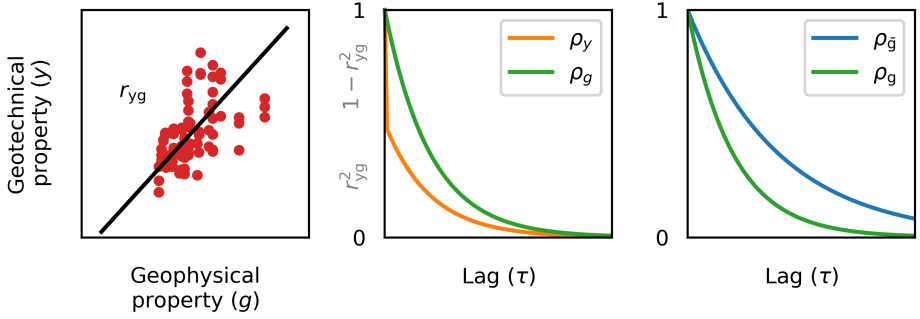
Figure 4.1: Relationship between the correlation structures of y and g. When the variance within homogeneous deposits is small enough, a linear relationship can be assumed between y and g (left plot). Because the relationship is imperfect, the correlogram ρ_g predicts a fraction (r_{yg}^2) of the correlogram ρ_y (middle plot). The correlogram of g cannot be estimated from direct samples of g, but from tomographic data $\bar{g}$ (right plot). The correlogram of the tomogram $\rho_{\bar{g}}$ is deformed with respect to the true correlogram of the geophysical property ρ_g due to tomographic inversion.

4.2.3. UNCERTAINTIES INTRODUCED BY GEOPHYSICAL TOMOGRAMS IN THE CORRELOGRAM

DEFORMATION OF THE CORRELOGRAM OF A TOMOGRAM

A tomogram is an approximate image of the subsurface, which is obtained through inversion. The inversion process for ERT data consists in fitting the measured response of a geophysical survey, d, to the response of the forward model, f, for electrical conduction (ERT) (Rücker, Günther, and Spitzer, 2006). The response of the forward model is a function of the spatial distribution of the geophysical property, $g(x, y, z)$, in the subsurface. The tomogram, $\bar{g}$, is the vector that minimizes the functional

$$\Phi_d(\bar{g}) = (d - f(\bar{g}))^T D^T D(d - f(\bar{g})) + \lambda(\bar{g} - g_{ref})^T C^T C(\bar{g} - g_{ref}). \qquad (4.9)$$

The upper bar on $\bar{g}$ is used to emphasize the fact that $\bar{g}$ is an approximate image of the geophysical property g. In Equation 4.9, D is a weighting matrix that contains the correlation structure of measurement errors (Günther, Rücker, and Spitzer, 2006a; Friedel, 2003). The second term in Equation 4.9, the regularization, is needed because the ERT inverse problem is ill-posed. In this study, smoothness regularization was used to define the regularization term (Rücker, Günther, and Spitzer, 2006) where the matrix C is a constraint matrix of first order derivatives of $\bar{g}$, and g_{ref} is a reference model. The strength of the regularization is given by λ. The minimization of Φ produces a tomogram, $\bar{g}$, which is an approximate and smooth representation of the geophysical property g. Consequently, the correlogram of the tomogram, $\rho_{\bar{g}}$, is deformed with respect to the true correlogram ρ_g (Figure 4.1 right). The deformation of the correlogram tends towards larger correlation lengths due to averaging of the fine-scale details of the subsurface (Day-Lewis, 2005).

GEOSTATISTICAL INFERENCE OF THE UNDEFORMED CORRELOGRAM

We applied geostatistical inference (Looms et al., 2010; Hansen, Looms, and Nielsen, 2008) to estimate the undeformed horizontal correlogram ρ_g and the uncertainty associated to that estimation. Consider a homogeneous soil unit that has a spatially-correlated geophysical property, g, with an unknown correlation structure ρ_g (top of Figure 4.2). The field data consists of a geophysical tomogram, $\bar{g}$, whose correlation structure $\rho_{\bar{g}}$ is deformed with respect to the unknown truth ρ_g. We estimated the unknown correlogram ρ_g from the known correlogram of the tomogram $\rho_{\bar{g}}$ with geostatistical inference. The inference process was divided in four steps that are shown in Figure 4.2. In step 1, a list of possible scenarios is formulated, each of which is defined by a correlation model (Equation 4.3) with theoretical correlation length θ_{gi}. A representative number of random field realizations of the geophysical property, g, are generated for each scenario. In step 2, geophysical tomograms are simulated over those realizations. The geophysical tomogram of each realization, $\bar{g}$, is used to calculate the horizontal correlogram $\rho_{\bar{g}}$ in step 3. In step 4, the tomographic correlograms $\rho_{\bar{g}}$ of the scenarios and the field data are compared in terms of their correlation length, $\theta_{\bar{g}}$. The distribution of $\theta_{\bar{g}}$ of each scenario is shown as a box plot in Figure 4.2 while $\theta_{\bar{g}}$ of the field tomogram is shown as a horizontal line. The estimated undeformed correlogram, ρ_g, is the one whose deformed correlogram, $\rho_{\bar{g}}$, produces the smallest error with respect to the deformed correlogram of the field tomogram. A measure of error was defined as the squared difference between the median correlation length of each box plot and the field correlation length (bottom of Figure 4.2). In Figure 4.2, scenario θ_{g2} shows the lowest error although it is similar to that of θ_{g3}. Therefore, both scenarios are similarly likely to describe the undeformed correlogram ρ_g. This uncertainty in the estimation of ρ_g is caused by tomographic inversion and increases with decreasing tomographic resolution.

4

4
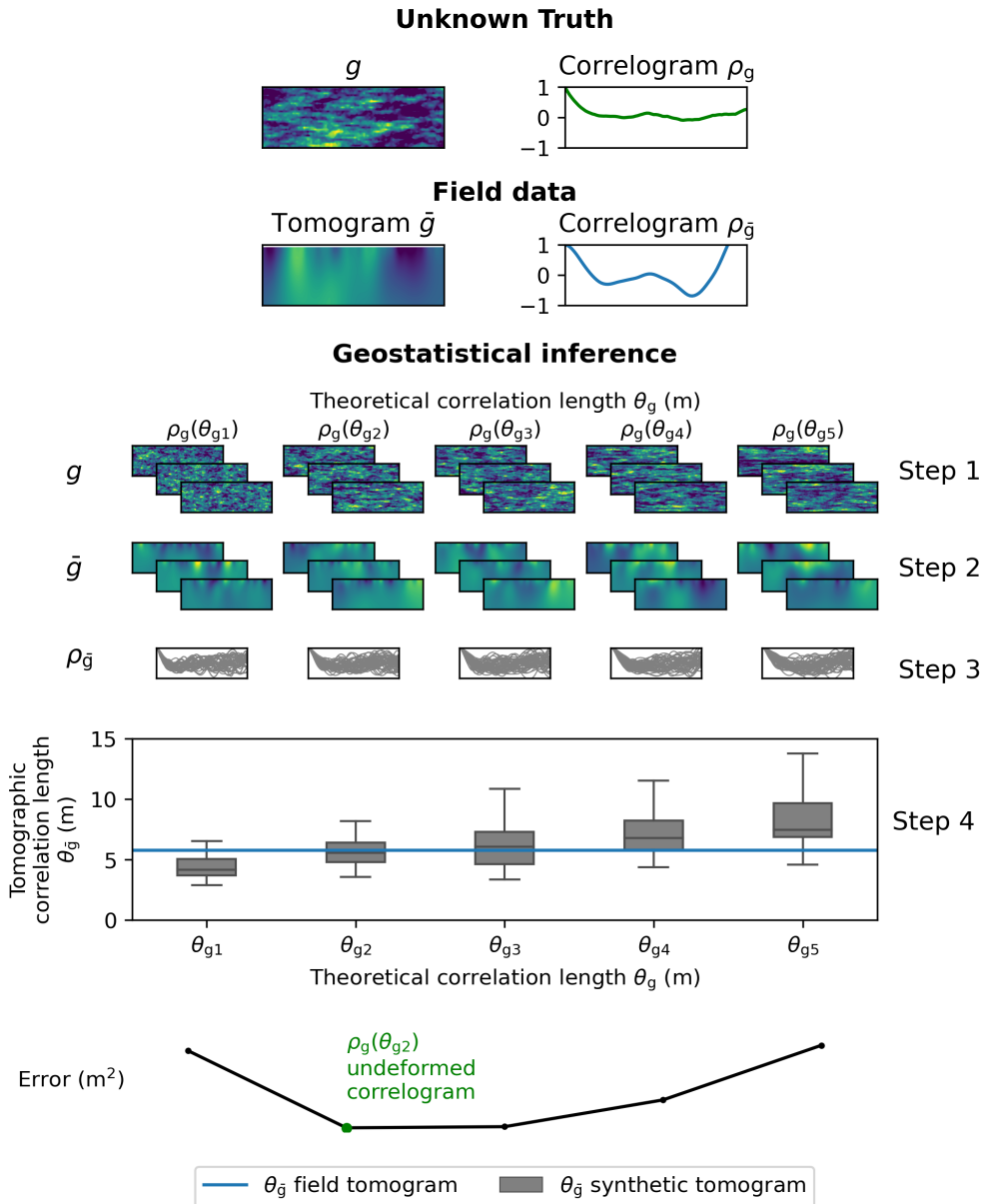
Figure 4.2: Geostatistical inference of the undeformed correlogram of a geophysical property, ρ_g, from the deformed correlogram of a geophysical tomogram, $\rho_{\bar{g}}$. Realizations of the geophysical property, g, with different scenarios of theoretical correlation lengths, θ_{gi}, are generated (step 1). Over these realizations, synthetic geophysical data are simulated, and a tomogram for each realization, $\bar{g}$, is generated (step 2). From the correlogram of each tomogram $\rho_{\bar{g}}$ (step 3), the correlation length is calculated (step 4). The error is calculated between tomographic correlation length of the field tomogram and the scenarios. The most likely undeformed correlogram of the soil unit, ρ_g, is the one associated to the theoretical correlation length with the lowest error ($\rho_g(\theta_{g2})$ in the figure).

4.3. RESULTS: LEINDEERT DE BOERSPOLDER SITE

The horizontal correlogram of a geotechnical property, ρ_y, was estimated from the tomogram of a geophysical property g. We used the notation $\bar{g}$ when referring to the tomogram in order to emphasize the fact that $\bar{g}$ is a smooth representation of the, unknown, true g. The process of estimating the correlogram ρ_y consists in (1) estimating $\rho_{\bar{g}}$ from the field data (Section 4.3.1), (2) estimating ρ_g from $\rho_{\bar{g}}$ with geostatistical inference (Section 4.3.2), and (3) estimating the fraction of ρ_y that can be estimated from ρ_g (Section 4.3.3). The geotechnical property in this test site was the cone resistance of a CPT while the geophysical property was the electrical resistivity of an ERT tomogram. A large number of CPTs were available in this test site. Therefore, the horizontal correlogram ρ_y was also calculated directly from the CPTs and compared to ρ_y estimated from the geophysical tomogram.

4.3.1. EXPERIMENTAL CORRELOGRAMS OF THE FIELD DATA

The Leindeert de Boerspolder site (Ldb) used to be a polder located in the West of the Netherlands, close to the city of Leiden. In 2015, a failure test was carried on a stretch of the dike surrounding the polder (de Gast, 2020). For that purpose, an intensive site investigation campaign was carried out (de Gast, Hicks, and Vardon, 2020). Part of the site investigation consisted of twenty-nine CPTs along the dike crest from which three near-horizontal soil units were identified. From top to bottom, the man-made dike material, which consists of silt, clay, sand and rubble, overlies natural peat deposits followed by clay deposits. Figure 4.3 (left) shows a contour plot of the cone resistance of those CPTs and Table 4.1 summarizes the statistics of the soil units. The cone resistance of each layer showed a vertical trend that was removed to ensure stationarity. A special emphasis was made on the upper layer (black polygon in Figure 4.3) whose experimental (horizontal) correlogram is shown on the right-hand side of Figure 4.3. The experimental correlogram was fitted to a Markov correlation model (Equation 4.3) which resulted in a horizontal correlation length, θ_y, of 5.3 m (Figure 4.3). The vertical correlation length of the CPT data, θ_v, was calculated in a similar fashion and was equal to 0.25 m. The vertical correlation length is used in Section 4.3.2 to constrain the inference of the horizontal correlogram.

A surface-based direct-current ERT data set was collected in summer 2021 (Olalla, 2022). The ERT data were collected along the crest of the dike coincident with the CPT data of Figure 4.3. The data were collected with a dense line of sensors whose acquisition parameters are summarized in Table 4.2. The ERT tomogram was constructed with a regularization strength, $\lambda = 5$. The value of λ was optimally determined with the L-curve method (Günther, Rücker, and Spitzer, 2006a) and it is a trade-off between data fit and regularization fit (Equation 4.9). Data outliers were removed from a first inversion round by comparing the measured response to the inverted ERT response. Data outliers were considered those that did not fit the inverted response within three Mahalanobis distances. The tomogram of the second inversion round, which was carried out without data outliers, is shown in Figure 4.4 (left). The horizontal correlogram of the ERT tomogram was calculated for the upper layer only, and it is shown on the right-hand side of Figure 4.4. The upper layer in the tomogram had a mean of 17.43 Ω m and a standard

deviation of $1.59\,\Omega\,\text{m}$. The correlogram was fitted to a Markov correlation model (Equation 4.3) which resulted in a correlation length, $\theta_{\tilde{g}}$, of $7.0\,\text{m}$ (Figure 4.4). The vertical cell size of the ERT tomogram ($0.25\,\text{m}$) was too large to obtain a meaningful estimation of the correlation length in the vertical direction. Therefore, the vertical correlogram of the ERT tomogram was not calculated.

4.3.2. UNCERTAINTY IN THE CORRELOGRAM OF THE GEOPHYSICAL PROPERTY

In the previous section, the horizontal correlogram of the field ERT tomogram, $\rho_{\tilde{g}}$, was estimated. As mentioned in Section 4.2.3, $\rho_{\tilde{g}}$, is deformed because of tomographic inversion. In this section, we use geostatistical inference (Section 4.2.3) to estimate the undeformed correlogram ρ_g and the associated uncertainty to that estimation. We used the correlation length θ to characterize corrrelograms. The inference process applied to the field data is shown in Figure 4.5 and elaborated next.

In step 1 (not shown in Figure 4.5), a list of possible (undeformed) horizontal correlograms ρ_g was selected. The list of scenarios was narrowed down by considering that the undeformed correlation length θ_g should be in the vicinity of $\theta_{\tilde{g}} = 7.0\,\text{m}$. Therefore, the values of θ_g for each possible scenario were 3, 4, 5, 6, 7, 8, and $9\,\text{m}$. These values of θ_g are denoted as the theoretical correlation length in Figure 4.5. The vertical correlation length of all the scenarios was kept constant at $\theta_v = 0.25\,\text{m}$ which is the same value of θ_v calculated from the CPT data. For each scenario of θ_g, fifty random field realizations of the geophysical property were generated with a mean, $\mu = 20\,\Omega\,\text{m}$, and a standard deviation $\sigma = 2.5\,\Omega\,\text{m}$. The mean and standard deviation are similar to the statistics of the upper layer in the field ERT tomogram.

In step 2 (not shown in Figure 4.5), ERT data were simulated and a tomogram was made for each realization of each scenario of θ_g. Because the scenarios were later compared to the field data, the acquisition and inversion parameters were the same as in the field data. That is, the ERT data was simulated with the acquisition parameters of Table 4.2. The simulated ERT data were contaminated with noise in order to simulate measurement error. The noise levels of the synthetic data were similar to the measurement error of the field data. The noisy data were inverted with a regularization strength $\lambda = 5$.

In step 3 (top of Figure 4.5), the tomographic correlograms of the simulated data, $\rho_{\tilde{g}}$ were calculated. The correlograms were calculated within the same polygon of Figures 4.3 and 4.4, i.e. the upper-most three meters. Even though the realizations of the random fields were meant to be stationary, a linear trend was removed from the tomograms in the horizontal direction prior to the calculation of the correlograms. Though small in all cases, the linear trend appears because of the constrained domain size of the analysis, which is delimited by the top-layer polygon. The tomographic correlation length, $\theta_{\tilde{g}}$, was calculated for each correlogram. The distribution $\theta_{\tilde{g}}$ is shown as box plots in Figure 4.5.

In step 4 (bottom of Figure 4.2), the field data and the possible scenarios are compared in terms of their tomographic correlation length. The box plot in Figure 4.2 shows the experimental value of $\theta_{\bar{g}}$ as a function of theoretical correlation length. A measure of error was defined to compare the fit of the field data to each scenario. The error was defined as the squared distance between the field value of $\theta_{\bar{g}}$ and the median value of the distribution of $\theta_{\bar{g}}$ of each scenario (bottom of Figure 4.5). Therefore, the lower the error, the higher the likelihood that a scenario of theoretical θ_{g} represents the undeformed correlogram ρ_{g}. Unlikely scenarios were considered those whose interquartile range did not contain the field value of $\theta_{\bar{g}}$, i.e. scenarios of theoretical correlation length, θ_{g}, smaller than 4 m. On the other hand, the most likely scenario is that with $\theta_{g} = 6$ m. Nevertheless, larger values of θ_{g} up to 8 m result in a similar error as $\theta_{g} = 6$ m, which is shown in the flat portion of error plot. Therefore, based on a squared-distance error, the true correlation length of the geophysical property in the Ldb site is likely between 6 m and 8 m. The range represents the uncertainty introduced by the ERT tomogram in the estimation of the correlogram.

4.3.3. CORRELOGRAM OF THE GEOTECHNICAL PROPERTY

The horizontal correlogram of the geotechnical property, ρ_{y}, is estimated in this section from ρ_{g}. Figure 4.6 shows the horizontal correlogram ρ_{g} estimated in the previous section. As a reference, we also estimated the horizontal correlogram ρ_{y} directly from the CPT data. The correlograms ρ_{g} and ρ_{y} show a favorable comparison in terms of correlation lengths. This favourable comparison suggests that ERT tomograms can be used as an alternative method to estimate the correlation length of a geotechnical property. However, as demonstrated in Section 4.2.2, the correlogram ρ_{g} can explain only a fraction of ρ_{y}. That fraction is given by the squared correlation coefficient r_{yg}^{2}. Estimating r_{yg}^{2} from high-resolution data, such as CPTs, could lead to an underestimation of the relationship between y and g because the data is more sensitive to nugget effects (Shmaryan and Journel, 1999). Therefore, we approximated r_{yg} by averaging vertically the cone resistance (black polygon in Figure 4.3) and the electrical resistivity (black polygon in Figure 4.4). The scatter plot of the vertical averages is shown in Figure 4.6 (right). The value of $r_{yg} = 0.83$ and $r_{yg}^{2} = 0.69$ show a strong correlation between the geotechnical property y and the geophysical property g. To sum up, in the Ldb test site, the correlogram of the geotechnical property ρ_{y} can be explained to a large extent ($\sim 70\%$) by the correlogram of the geophysical property ρ_{g}. Also the correlogram ρ_{g} can be estimated with small uncertainty (6 m to 8 m) from the correlogram of the ERT tomogram $\rho_{\bar{g}}$ because of the high resolution of the ERT tomogram. The high resolution of the tomogram is a result of the dense grid of ERT sensors and the shallow location of the analyzed soil layer (upper three meters).

Soil Unit	Mean (trend) μ/ MPa	Standard deviation σ/MPa	Elevation z/m
Dike material	$0.8081 + 0.1244z$	0.3346	-0 to -3
Peat	$0.3018 + 0.0157z$	0.0505	-3 to -5
Clay	$0.7592 + 0.1863z + 0.0149z^2$	0.0234	-5 to -11

Table 4.1: Summary statistics of the CPT cone resistance of Figure 4.3 (de Gast, 2020). The standard deviation was calculated with the detrended data.

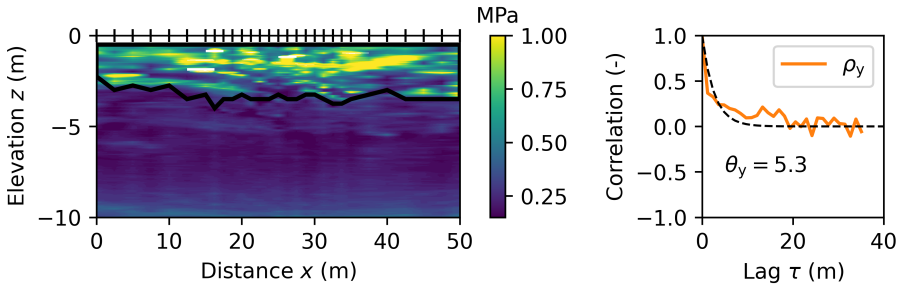| Parameter	Value
Sensor spacing a	0.5 m
Number of sensors	103
Array type	Dipole-dipole
Maximum geometric factor	5000

Table 4.2: ERT acquisition parameters.

Figure 4.3: Field CPT data. Contour plot of the cone resistance (left). Horizontal correlogram of the area inside the black polygon (right). The vertical lines on the left figure indicate the position of the CPTs. The dashed line on the right figure is the best-fit correlation model with a correlation length $\theta_y = 5.3$ m
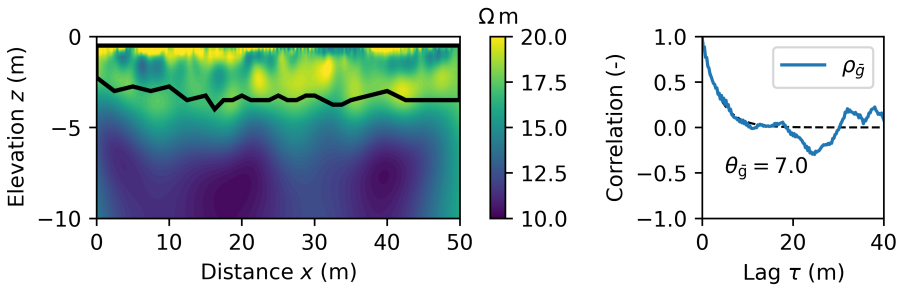

Figure 4.4: Field ERT tomogram. Contour plot of the electrical resistivity (left). Horizontal correlogram of the area inside the black polygon (right). The dashed line on the right figure is the best-fit correlation model with a correlation length $\theta_{\bar{g}} = 7.0$ m
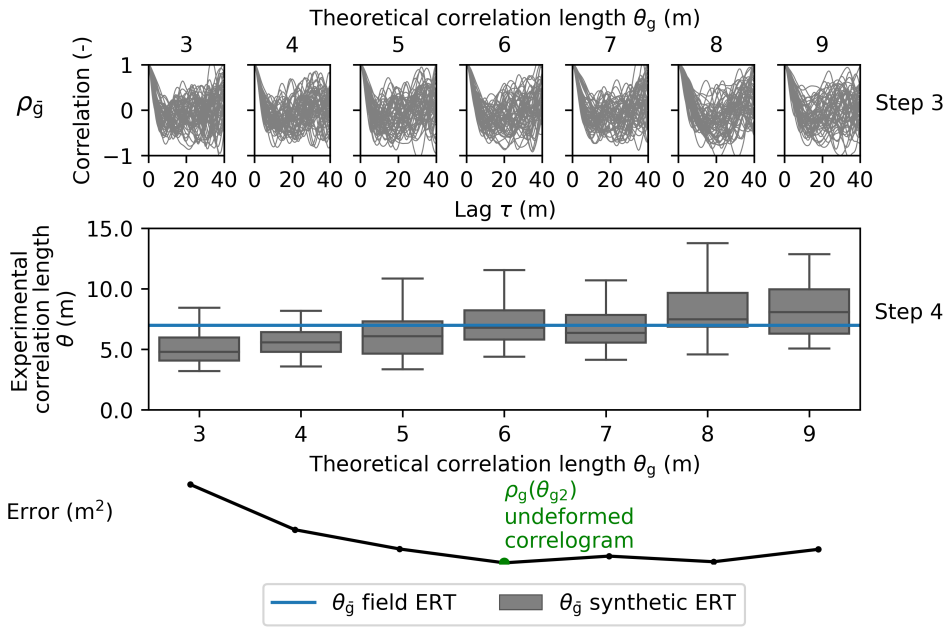
Figure 4.5: Geostatistical inference of the correlogram of the upper soil unit, ρ_g, of the Ldb site from the field tomogram, $\bar{g}$. The upper row shows the correlogram of the tomogram of each scenario of θ_g. The middle row shows the distributions of the correlation length estimated from the realizations of g and $\bar{g}$. The horizontal line is the correlation length of the field ERT tomogram. The bottom row shows the error between the correlation length, $\theta_{\bar{g}}$, of the field data and the tomograms of the realizations. The most likely scenario is given by $\theta_g = \theta_y = 6.0\,\mathrm{m}$.
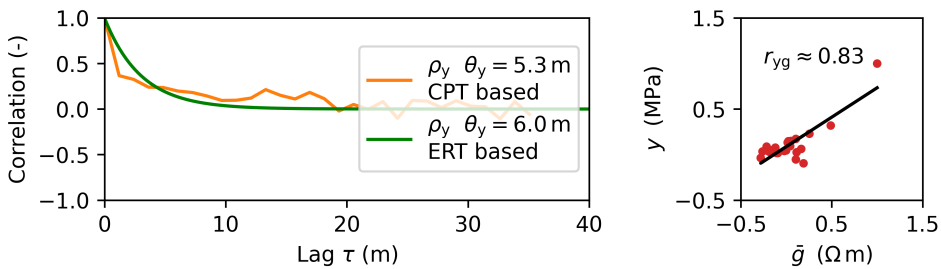

Figure 4.6: Correlogram estimation of the geotechnical property y based on the tomogram of the geophysical property, g. The correlogram of y estimated with ERT data is shown in green, while the correlogram of y estimated with CPT data is shown in orange. The correlogram of the field tomogram, $\rho_{\bar{g}}$, is shown in blue. The estimated correlation lengths are also shown.

4.4. Discussion

4.4.1. Geotechnical data error

A closer look at the correlogram of the CPT data, ρ_y, in Figures 4.3 and 4.6 shows, contrary to the correlogram of the tomogram, $\rho_{\tilde{g}}$, a major drop in correlation over a short lag distance. The drop in correlation could be attributed to outliers and noise in the CPT measurements. A few outliers in the CPT data could largely affect the value of spatial correlation. To illustrate the effect of outliers in the correlogram, Figure 4.7 (left) shows the distribution of the cone resistance obtained by gathering the 29 CPTs of the Ldb site. The vertical lines in Figure 4.7 (left) represent fractiles of the CPT data. Figure 4.7 (right) shows the correlogram of the CPT data after different fractiles were removed. The correlogram estimated with the raw data set, i.e. 0% data removal, shows higher drop in correlation than the correlograms of the fractile-removed CPT data. The correlogram of the CPT data presented in the results section (Figures 4.3 and 4.6) was calculated by removing the 1% fractile of the cone resistance values. The value was chosen because 1% of the data represents a negligible amount of data, as shown in the distribution plot, and at the same time increases the spatial correlation significantly. Even though outliers were removed from the CPT data, the correlogram of y still shows a correlation drop at small lag distances. The drop could be attributed to noise, such as vertical inaccuracies in the CPT measurements. To show this, a random field realization of y was sampled with twenty-nine synthetic CPTs at the same horizontal sample interval of the field CPT data of Figure 4.3. The realization was generated with $\theta_{y(h)} = 6.0\,\text{m}$ in the horizontal direction and $\theta_{y(v)} = 0.25\,\text{m}$ in the vertical direction. Figure 4.8 shows the horizontal correlogram calculated from the synthetic data of y. The noise-free correlogram is well retrieved by the twenty-nine synthetic samples as shown by the value of correlation length, $\theta_{y(h)} = 6.4\,\text{m}$. The effect of vertical inaccuracies in the CPT data was estimated by randomly shifting each CPT one cell up, one cell down or zero cells. The vertical size of the cells in the realization was 0.1 m. The horizontal correlogram estimated from the vertically inaccurate data is shown in Figure 4.8. The correlation at short lag distances shows a large drop similar to the drop visible in the correlograms of the field CPT data (Figures 4.3 and 4.6). In addition, the correlation length estimated from the noisy correlogram is smaller than the noise-free data.

4.4.2. Geophysical data error

In the results section, it was shown that the correlation length estimated with ERT data compared favorably with the correlation length calculated directly from CPT data. The ERT data set used in this study contained a high density of ERT sensors, i.e. one sensor per half a meter. Also, the variance of the ERT and CPT values in the top layer was large because the top layer is of anthropogenic origin. Therefore, the conditions to use ERT for measuring stationary fluctuations were favorable. In this section, we study the sensitivity of the tomographic correlogram, $\rho_{\tilde{g}}$ with respect to measurement error in the ERT data. The measurement error in ERT data is known to increase with increasing geometric factor (Friedel, 2003). In the case of a four-point ERT measurement, the geometric
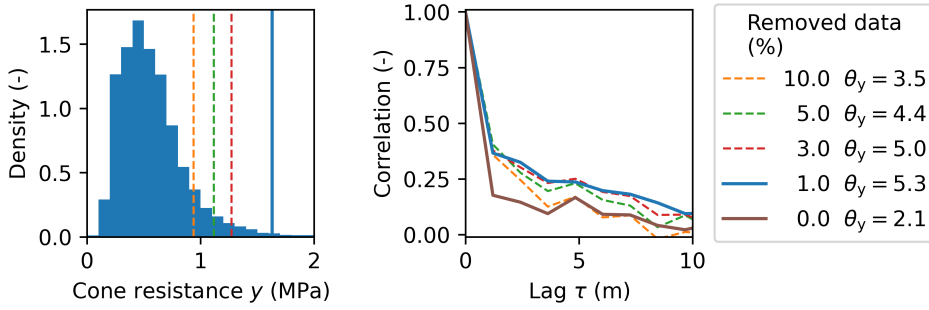
Figure 4.7: Sensitivity of the horizontal correlogram of the field CPT data to outliers. The plot shows the correlogram of the CPT data, ρ_y, estimated after a percentile of the data was removed. The associated correlation lengths are shown also in the plot.
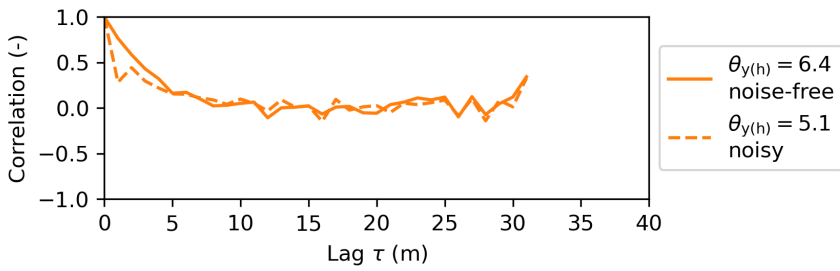
Figure 4.8: Sensitivity of the horizontal correlogram of y to vertical noise in the measurement. A random field realization of y was sampled with twenty-nine synthetic CPTs located at the same horizontal interval of Figure 4.3. The horizontal correlogram is well retrieved by the noise-free CPTs as opposed to the noisy data, which shows a large drop in correlation at short lag distances. Noise was added in the form of a random vertical shift to the synthetic CPTs.

factor is

$$k = \frac{2\pi}{\left(\frac{1}{r_{C_1 P_1}} - \frac{1}{r_{C_2 P_1}} - \frac{1}{r_{C_1 P_2}} + \frac{1}{r_{C_2 P_2}} \right)}$$

where $r_{C_i P_j}$ is the separation between the current electrode C_i and the potential sensor P_j. The geometric factor is measure of separation between the current and potential ERT sensors (Stummer, Maurer, and Green, 2004). Therefore, the larger the geometric factor, the smaller the electric potential, and consequently the higher the measurement error. Figure 4.9 (top) shows the measurement error of the field ERT data of Section 4.3, which was calculated from reciprocal measurements. The mean of the error is centered around zero while the standard deviation shows a linear dependency with the geometric factor. Figure 4.9 (bottom) shows a close-up of the standard deviation and the best-fit line with a y-intercept $b_{err} = 1.1\%$ and a slope $m_{err} = 0.00145$. The y-intercept $b_{err} = 1.1\%$ represents a base level of measurement error. The measurement error increases at a rate of approximately 1.5 % per 1000 m of geometric factor. For comparison, the standard deviation of the field ERT tomogram in the top layer was approximately 10 % (1.59/17.43).

The effect of measurement error on the tomographic correlogram was analyzed with synthetic data. For that purpose, fifty random field realizations of electrical resistivity were generated with similar statistical properties to the field data presented in the results section. That is, the mean of the random fields was 20 Ω m, the standard deviation was 1.5 Ω m, the horizontal correlation length was 6 m, and the vertical correlation length of 0.25 m. Subsequently, surface-based ERT tomograms were simulated over the electrical resistivity realizations with 25, 49, and 97 ERT sensors. The original horizontal correlograms were compared to the tomographic correlograms of the upper three meters. Figure 4.10 shows the ratio of the tomographic correlation length $\theta_{\tilde{g}(h)}$ to the original correlation length $\theta_{g(h)}$ in the horizontal direction. Figure 4.10 shows different combinations of measurement error b_{err} and m_{err}. For comparison, the standard deviation of the random field realizations was 7.5 %. The ratio $\theta_{\tilde{g}(h)}/\theta_{g(h)}$ does not show a clear dependency to the measurement error even at large levels of error. Therefore, the tomographic correlogram is not affected by measurement error in the ERT data. A possible reason is that the ERT measurements are weighted in the inversion process by the measurement error (matrix D in Equation 4.9).

4.4.3. SENSOR DENSITY

This section analyzes the effect of sensor density on the deformation of the tomographic correlogram, $\rho_{\tilde{g}}$, in the horizontal direction. Large deformations of $\rho_{\tilde{g}}$ increase the uncertainty in the estimation of ρ_g and therefore of ρ_Y. The tomographic correlogram deforms as a result of poor tomographic resolution which in turn is highly dependent on sensor density. To analyze the effect of sensor density on the deformation of the tomographic correlogram, a subsurface model was created with a horizontal size of 50 m and a vertical size of 15 m. A set of horizontal, $\theta_{g(h)}$, and vertical, $\theta_{g(v)}$, correlation lengths were assigned to the model. For each pair of correlation lengths, fifty realizations were generated, and for each realization, surface-based tomograms were generated with different sensor densities. The deformation of the tomographic correlograms was quantified by the ratio $\theta_{g(\tilde{h})}/\theta_{g(h)}$. The sensor density was defined as the ratio θ_g/a where a is the sep-
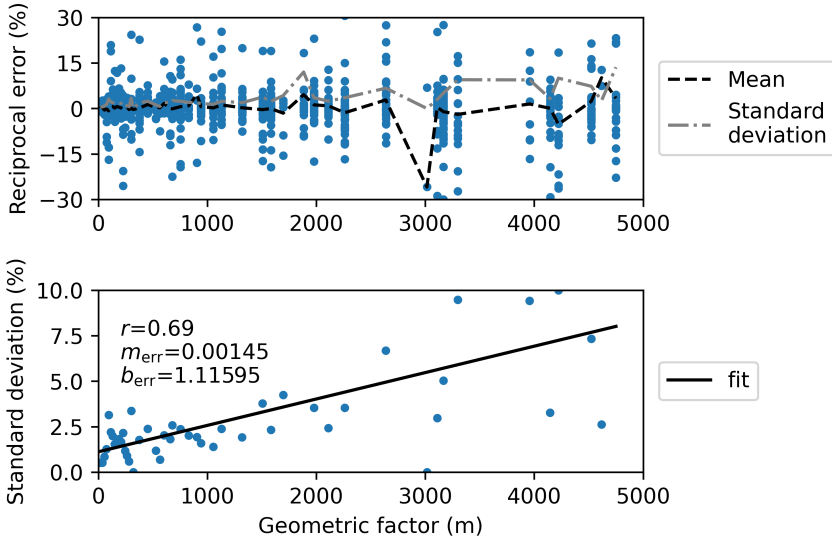
Figure 4.9: Reciprocal error of the field data as a function of geometric factor. The top figure shows the reciprocal error. The bottom figure shows the standard of the reciprocal error and the best-fit line.
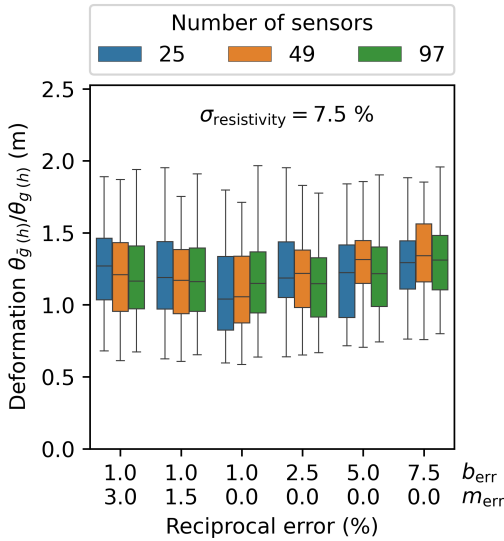

Figure 4.10: Horizontal deformation of the tomographic correlogram, $\theta_{\bar{g}(h)}/\theta_{g(h)}$, as a function of ERT measurement error.

aration between sensors.

Figure 4.11 (left) shows the deformation of the tomographic correlogram, $\theta_{g(\bar{h})}/\theta_{g(h)}$, as a function of sensor density, $\theta_{g(h)}/a$. The subscript h refers to the horizontal direction of the analysis. The figure shows that the deformation of the tomographic correlogram decreases with increasing sensor density. To illustrate, the distribution of the deformation, $\theta_{\bar{g}(h)}/\theta_{g(h)}$, shortens and the median decreases for increasing values of $\theta_{g(h)}/a$. Figure 4.11 (left) shows several color-coded boxplots for each sensor density. The colors indicate the anisotropy in the correlation length of the original model, $\theta_{g(h)}/\theta_{g(v)}$. The anisotropy of the original model does not show any significant effect on the deformation of the correlogram. Figure 4.11 (right) shows, similar to the left plot, the deformation of the tomographic correlogram, $\theta_{g(\bar{h})}/\theta_{g(h)}$ as a function of sensor density. As opposed to the left plot, the sensor density is plotted as the ratio $\theta_{g(v)}/a$ where $\theta_{g(v)}$ is the vertical correlation length of the original model. The vertical correlation length, $\theta_{g(v)}$, shows no significant influence in the deformation of the tomographic correlogram, $\theta_{g(\bar{h})}/\theta_{g(h)}$. That is, the distribution and median of $\theta_{\bar{g}(h)}/\theta_{g(h)}$ remain similar at varying values of $\theta_{g(v)}/a$.

In sum, to reduce the deformation of the tomographic correlogram and therefore the uncertainty in the estimation of the correlogram of y, the sensor density has to be as large as operationally possible. Figure 4.11 (left) can be seen as an experimental guide to choose a value of sensor spacing, a. The figure shows that for sensor densities smaller than four, the median and the width of the tomographic deformation, $\theta_{\bar{g}(h)}/\theta_{g(h)}$, increase at a higher rate than for sensor densities larger than four. Finally, the chosen value of sensor spacing should be a trade-off between the estimation uncertainty required and operational limitations. The estimation uncertainty is given by the width and median of the distribution of $\theta_{\bar{g}(h)}/\theta_{g(h)}$. Meanwhile, operational limitations are given by the ERT equipment and survey time.

4.4.4. IN-SITU GEOTECHNICAL-GEOPHYSICAL RELATIONSHIP

The correlation coefficient, r_{yg}, between the geotechnical property y and the geophysical property g determines the effectiveness of the geophysical data to characterize a geotechnical property. In geotechnical applications, the correlation coefficient can be efficiently determined from electric CPTs. Electric CPTs have been available for decades (Campanella and Weemees, 1990; Daniel et al., 1999) and are standard practice in many geotechnical projects. In this section, we address some practical aspects of using electric CPTs to derive point-scale relationships. The first aspect is the trend removal. The calculations made in this study are based on the correlation between the stationary fluctuations between the geotechnical and geophysical properties. Therefore, the geotechnical and geophysical data have to be detrended. The second practical aspect is related to the specifics of the electric resistivity sensors in a CPT. The electric resistivity sensors are shifted with respect to the cone and sleeve friction sensors (Daniel et al., 1999). Therefore, the electrical resistivity measurements are also shifted. Moreover, an electric CPT measures the electrical resistivity over an average volume of soil that is larger than the
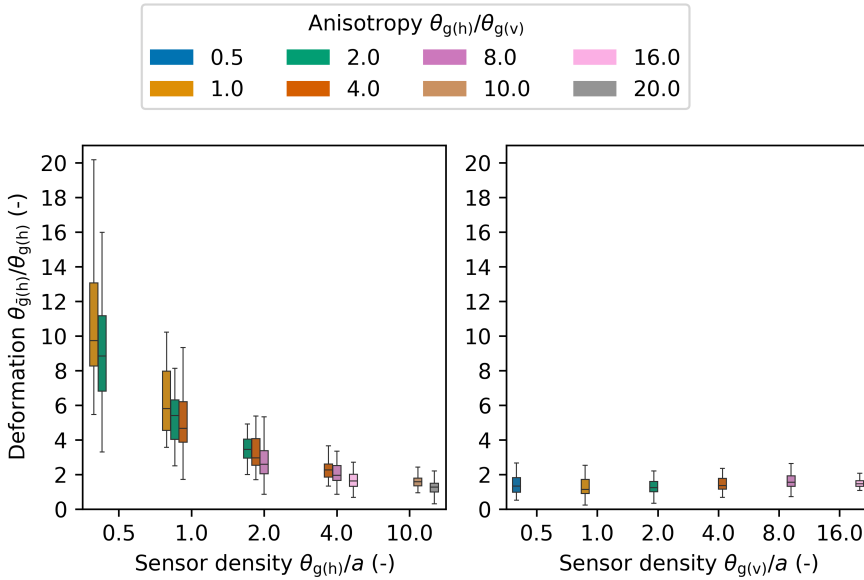
Figure 4.11: Horizontal deformation of the tomographic correlogram, $\theta_{\tilde{g}(h)}/\theta_{g(h)}$, as a function of sensor density, θ_g/a. The left plot shows the horizontal sensor density while the right plot shows the vertical sensor density. The ratio $\theta_{g(h)}/a$ on the right figure was kept constant and equal to sixteen.

cone and sleeve friction volume. These aspects have to be accounted for in order to not underestimate the relationship between the geotechnical and geophysical properties.

An actual electric CPT, not from the Ldb site, was analyzed in order to address the practical aspects mentioned above and calculate the correlation coefficient, r_{yg}, between geotechnical and geophysical properties. The raw data of the electric CPT are shown in Figure 4.12 (top left). The properties of the clay layer that is located between $-1.0\,\mathrm{m}$ and $-3.5\,\mathrm{m}$ are further analyzed. The Figure shows that the stationary fluctuations of the cone resistance and the electrical resistivity follow the same pattern. The scatter plot of the detrended CPT data is shown in Figure 4.12 (bottom left). The shift between y and g was calculated as the shift that maximizes the correlation coefficient. The value of that shift was 6 cm. The shift-corrected scatter plot is show in Figure 4.12 (bottom middle). Clearly, the correlation coefficient, $r_{yg} = 0.59$ of the raw detrended data underestimates the relationship between y and g. The correlation coefficient significantly increases by a small correction in the shift from $r_{yg} = 0.59$ to $r_{yg} = 0.72$. The raw CPT data (top left of Figure 4.12) shows more jitter in the geotechnical measurements y than in the geophysical measurements g. The jitter in g is smaller because g is measured over a larger volume than y. A boxcar filter was applied to the raw data in order to reduce the jitter. Figure 4.12 (top right) shows the CPT data after the trend was removed, the shift was corrected, and the jitter was reduced. The correlation coefficient r_{yg} increased from a value of 0.72 to a value of 0.76 by correcting the jitter (bottom right of Figure 4.12). In
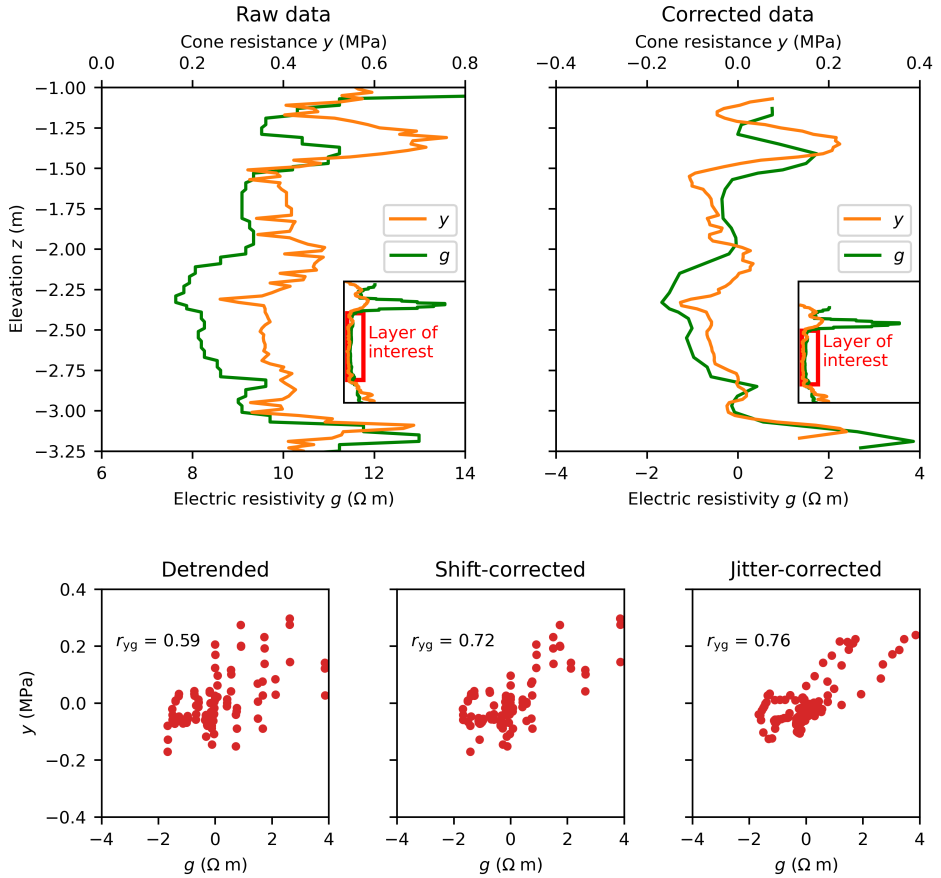
Figure 4.12: An example of a raw electric CPT. The fluctuations of the cone resistance, y, resemble the fluctuations of the electric resistivity, g.

sum, the correlation coefficient r_{yg} can be derived efficiently from CPT data. However, the correlation coefficient can underestimate the strength of the relationship between geotechnical and geophysical properties if the raw data is not corrected.

4.4.5. IMPLICATIONS FOR THE ANALYSIS OF GEOTECHNICAL INFRASTRUCTURE

The spatial variability of soil properties is a crucial component in the design and assessment of geotechnical infrastructure. It determines whether a geotechnical structure reaches the limit state by local or global failure (CEN, 2004). To illustrate, the limit state of geotechnical structures is governed by local failure when soil properties are correlated at large distances. Meanwhile, the limit state is governed by global failure when soil properties are correlated at short distances. Therefore, the type of failure is deter-

mined by the correlation structure of strength properties (Frank et al., 2004). CEN (2004) deals with uncertainties in geotechnical properties through the cautious selection of values, the so-called characteristic values. In quantitative terms, the characteristic value is the 5% fractile of the total uncertainty in a geotechnical property (Prästings, Spross, and Larsson, 2019). In Coefficient Of Variation (COV) notation, the total uncertainty is

$$COV_{\text{total}}^2 = \Gamma^2 \cdot COV_{\text{inherent}}^2 + COV_{\text{measurement}}^2 + COV_{\text{transformation}}^2 + COV_{\text{statistical}}^2 \quad (4.10)$$

where COV_{inherent} is the uncertainty due to inherent variability, $COV_{\text{measurement}}$ is the uncertainty due to measurement error, $COV_{\text{transformation}}$ is the transformation uncertainty, and $COV_{\text{statistical}}$ is the statistical uncertainty. Spatial variability is accounted for in Equation 4.10 through the factor Γ (Orr, 2017). The value of Γ equals 0 when properties are correlated over short distances. Meanwhile, the value of Γ equals 1 when properties are correlated over long distances. In most cases, the value of Γ lies between 0 and 1. The exact value of Γ depends not only on the correlation structure, but also on the specific geotechnical problem under analysis. Variance reduction techniques consist in finding a value of Γ that accounts for the geotechnical problem and the correlation structure of strength. In that case, COV_{total}^2 represents the effective strength distribution. In practice, it is difficult to apply variance reduction techniques because it is difficult to measure the correlation structure with conventional geotechnical site investigation data. Therefore, Γ is cautiously chosen to be 1 (Prästings, Spross, and Larsson, 2019) in which case COV_{total}^2 represents the underlying strength distribution. A cautious approach to choose characteristic values could result in overly conservative estimations of structural stability. For example, in the stability analysis of dikes, it has been shown that characteristic values chosen in this fashion, i.e. not accounting for spatial variability, result in overly conservative estimates of stability (Hicks et al., 2019; Varkey et al., 2020). Surface-based ERT tomograms could be an efficient alternative to measure the spatial variability and therefore aid in the selection of characteristic values that are not overly conservative.

4

4.5. CONCLUSIONS

A workflow to estimate the horizontal correlation structure, i.e. correlogram, of a geotechnical property from a geophysical tomogram was presented. The workflow was applied in a test site to estimate the correlogram of the CPT cone resistance from a surface-based ERT tomogram. The horizontal correlogram estimated with the ERT tomogram compared favorably to the correlogram estimated with a large number of CPTs. The favorable comparison and synthetic data analysis suggest that surface-based ERT can be an efficient alternative method to estimate the horizontal correlation structure of geotechnical properties, especially for the shallow-most layers. However, the effectiveness of the geophysical data to predict geotechnical variability is limited by the strength of the geophysical-geotechnical relationship and the density of ERT sensors in relation to the horizontal correlation length. The geotechnical-geophysical relationship, which is site specific, can also be efficiently estimated in-situ with electric CPTs. Synthetic data analysis suggest that ERT tomograms estimate the correlation structure with small uncertainty when the the spacing between ERT sensors is at least four times smaller than the correlation length of the soil property. ERT measurement error and the vertical correlation length of soil properties appear to have minor effect on the estimation of the ERT-based correlogram.

Surface-based geophysical tomograms show major advantages over direct samples to estimate the correlation structure of geotechnical properties. The major advantages are that tomograms are less susceptible to nugget effects, less destructive, and require less operational effort for a reliable estimate of the correlation structure. Although the methods presented in this study are applicable to any geophysical method, surface-based ERT is especially suitable for geotechnical applications because the density of sensors can be fine-tuned for specific applications and the stationary fluctuations of electrical resistivity correlate strongly to the stationary fluctuations of strength properties.

5

CONCLUSIONS

5.1. RESTATING THE RESEARCH PROBLEM

Climate change poses significant challenges in terms of flood risk management in low-lying countries. In order to climate-proof low-lying territories, the reliability of water defenses has to meet up-to-date safety standards. However, improving the reliability of water defenses requires an enormous financial effort. Therefore, it is crucial to carefully assess the reliability of water defenses such that reinforcement efforts are allocated optimally. A problem in the reliability assessment is the difficulty to characterize subsurface heterogeneity. There is a mismatch between subsurface heterogeneity and site investigation sampling, especially in the horizontal direction. Traditional site investigation methods sample the subsurface at scales that often miss important subsurface information. In the past decades, the use of geophysical methods has significantly increased for the site investigation of dikes. Electromagnetic (EM) methods have been especially popular in the exploration of dikes due to their ease of deployment and high acquisition speed. Nevertheless, two problems have limited their large-scale adoption in the water defense sector:

- Uncertainty in the Performance of EM Geophysical Methods: There has been a lack of clarity in the literature regarding the capability of EM geophysical methods to accurately map common subsurface features that are relevant for the stability analysis of dikes. To shed light on this problem, the thesis undertakes a comparative analysis of tomographic images derived from various EM devices within a controlled, synthetic subsurface environment.

- Qualitative Interpretation of Geophysical Data: The interpretation of geophysical data has traditionally been subjective and reliant on expert knowledge. To tackle this limitation, the thesis employs statistical methods to obtain quantitative insights into subsurface heterogeneity, particularly in terms of geometry and internal structure.

The research presented in this thesis aims at improving the understanding of electromagnetic methods in the exploration of dikes and their subsurface, such that, EM methods can be chosen adequately for reducing specific subsurface uncertainties in the reliability assessment of dikes. That is, this research aims at giving geophysical inputs for the geotechnical schematization of dikes. The geotechnical schematization of dikes is a complex process which is carried out by experienced geotechnical practitioners. The inputs provided in this research do not intend to replace expert geotechnical knowledge or automate the geotechnical schematization process. Instead, the research gives guidelines for geotechnical practitioners to reduce uncertainties related to the presence, absence, or composition of specific adverse subsurface features.

5.2. INPUTS FOR THE GEOTECHNICAL SCHEMATIZATION OF DIKES

Table 5.1 summarizes the EM inputs provided by this research for the geotechnical schematization of dikes. In the following sections, a description of the findings are given.

5.2.1. PERFORMANCE OF EM METHODS TO MAP HETEROGENEITY IN DIKES

Input 1: This research investigated the performance of EM methods in mapping subsurface heterogeneity in dikes. EM methods offer various possibilities for subsurface exploration (Ward and Hohmann, 1988). In dike assessment, EM exploration commonly relies on magnetic-dipole induction, referred to as EMI in this study, and direct-current Electrical Resistivity Tomography (ERT). However, the existing literature on EMI exploration in dikes lacks clarity regarding the actual performance of EMI devices. Some studies have indicated inferior results compared to ERT (Niederleithinger, Weller, and Lewis, 2012), but the reasons for such results are unclear due to the absence of modeling studies. This research modeled two types of commonly used EMI devices in engineering applications: frequency sounders and distance sounders. An important insight of this modeling study is that distance sounders outperform frequency sounders in mapping subsurface heterogeneity. Although this insight was suggested by the theoretical principles of each device, this research elaborates on this matter in the context of dikes. To explain further, for the range of electrical conductivity values found in geological deposits, the signal-to-noise ratio in frequency sounders is weaker than in distance sounders. To increase the signal magnitude in frequency sounders, higher frequencies are required which also results in shallower penetration depths. As a consequence, frequency sounders map subsurface heterogeneity ambiguously which could increase the likelihood of false negatives in EM exploration. In contrast, distance sounders achieve high signal-to-noise ratios without compromising penetration depth, making them a more reliable option for mapping subsurface heterogeneity in dikes.

Inputs 2 and 3: The most effective, yet not the fastest, EM method to explore water defenses is direct-current Electrical Resistivity Tomography (ERT). This method requires an operational effort that makes it unfeasible for large-scale deployment. The method can only be used for a detailed analysis of small areas. Interestingly, this research shows with synthetic (Chapter 2) and field data (Chapter 3) that EMI distance sounders can map geotechnically-relevant geological architecture to a comparable level as direct-current ERT. This finding is specially relevant for the detection of paleochannels, which are a large source of geological uncertainty in the reliability assessment of dikes. Moreover, EMI methods can survey large distances in a fraction of the time required by ERT, with significantly lower setup efforts for the acquisition systems. This presents an excellent opportunity to explore the subsurface more efficiently and identify the presence or absence of adverse subsurface features. A potential limitation of EMI methods is the presence of metalic objects, such as pipes, which can disturb the EM response. Additionally, both ERT and EMI show reduced performance in the presence of saline groundwater due to the reduced contrast in electrical resistivity. Therefore, EM exploration proves to be a cost-effective solution in low-salinity environments, such as river areas.

5.2.2. GEOMETRIC VARIABILITY

Input 4: EMI tomograms offer an approximate description of subsurface topology, which indicates large-scale changes in subsurface composition. That information can serve

two primary purposes. First, EMI tomograms can be leveraged to enhance the efficiency of intrusive site investigation efforts. By identifying large-scale changes in subsurface composition, site investigation activities can be planned and prioritized to ensure a more targeted and cost-effective subsurface exploration. Second, information about large-scale variations in subsurface composition aids in the definition and refinement of dike sections for geotechnical analysis.

Input 5: When dealing with certain subsurface features, accurately quantifying geometric characteristics, such as horizontal size and depth, becomes essential. For instance, in piping analysis of dikes, the thickness of the cover layer is crucial for safeguarding against internal erosion. Similarly, new bio-based dike reinforcement solutions (Zhou, Laumann, and Heimovaara, 2019) require a precise delineation of subsurface layers to optimize injection strategies and prevent potential instabilities. However, relying solely on tomograms for geometric dimensions often results in inaccuracies. To achieve accurate estimations, it is imperative to combine tomographic topology with ground-truth data from sources like boreholes. This research demonstrates that geometric characterization of subsurface features can be significantly improved even with a reduced number of ground-truth data points. This research uses an objective framework to interpret topological features from geophysical tomograms and to incorporate those features in the geometric characterization of the subsurface. This framework makes intermediate assumptions explicit and the data interpretation repeatable.

5.2.3. INTERNAL VARIABILITY

Input 6: The internal variability of soil properties is a crucial component in the stability of geotechnical infrastructure. It directly influences whether a geotechnical structure reaches the limit state by local or global failure (CEN, 2004). In other words, the type of failure is determined by the correlation structure of soil properties. This research shows that surface-based ERT is an efficient alternative method to estimate the horizontal correlation structure of geotechnical properties, especially for the shallow-most layers. Surface-based geophysical tomograms show major advantages over direct samples, as ERT tomograms are less susceptible to nugget effects, less destructive, and require less operational effort for a reliable estimate of the correlation structure. However, the effectiveness of the geophysical data to predict geotechnical variability in shallow layers is limited by the strength of the geophysical-geotechnical relationship and the density of ERT sensors in relation to the horizontal correlation length. The geotechnical-geophysical relationship, which is site-specific, can also be efficiently estimated in-situ with electric CPTs. Although the methods presented in this study apply to any geophysical method, surface-based ERT is especially suitable for geotechnical applications because the density of sensors can be fine-tuned for specific applications and the stationary fluctuations of electrical resistivity tend to correlate strongly to the stationary fluctuations of strength properties. By proposing an efficient and non-destructive method to estimate internal variability, this research contributes to the informed selection of characteristic values for geotechnical design and assessment. This contribution is crucial for the reliability assessment of dikes, as it has been shown that an uninformed selection of

characteristic values results in overly conservative estimations of reliability (Hicks et al., 2019; Varkey et al., 2020).

Table 5.1: Electromagnetic Exploration Inputs for the Geotechnical Schematization of Dikes

	Input Provided	EM Method	Key Findings for geotechnical schematization
1.	Distance sounders versus frequency sounders	EMI	Distance sounders outperform frequency sounders in mapping subsurface heterogeneity.
2.	ERT versus EMI	ERT/ EMI	ERT maps subsurface heterogeneity in higher detail than EMI. However, EMI distance sounders can achieve a comparable performance for mapping subsurface features, such as paleochannels.
3.	Poor performance in saline environments	ERT/ EMI	EM exploration performs poorly in saline environments due to the reduced contrast in electrical properties.
4.	Subsurface topology	EMI	Chapter 3 shows that EMI tomograms provide an approximate description of subsurface topology which could 1) aid the allocation of site investigation resources 2) aid the definition and refinement of dike sections for geotechnical analysis.
5.	Geometric characterization of soil layers	EMI/ ERT	Chapter 3 shows that geometric characterization of subsurface features can be significantly improved even with a reduced number of ground-truth data points.
6.	Small-scale horizontal composition	ERT	Chapter 4 presents a methodology to estimate the horizontal correlation structure for soil properties. Previously, such estimation required a large number of soil samples.

5.2.4. Uncertainty reduction

This research is part of the All-risk program, which to a large extent is concerned with the reduction of uncertainties in the reliability assessment of water defenses. The research on this thesis was concerned with the uncertainties related to subsurface heterogeneity. This section gives some insights as to how much subsurface uncertainty can be reduced with EM exploration. Two types of uncertainties can be reduced with EM exploration. First, the uncertainties related to the detection of adverse subsurface features. Second, uncertainties related to the inherent variability of geotechnical properties.

Chapters 2 and 3 explore the performance of EM methods for the detection of adverse subsurface features. The uncertainty regarding the presence of adverse features can be assessed, for the purpose of this analysis, as a probability. In geotechnical practice, these probabilities are assigned heuristically, based on site investigation and expert

geological knowledge. To illustrate, in the schematization of a dike a probability will be given to a subsurface scenario even though that particular scenario was not found in the site investigation campaign. The uncertainty related to the presence of that subsurface scenario propagates to the stability calculation making the safety assessment potentially overconservative. By introducing EM exploration, the presence of subsurface features can be better characterized. The clearest example in this thesis is the characterization of paleochannels, which can be confirmed or discarded effectively with EM exploration. In quantitative terms, validating the presence and extent of paleochannels using EM exploration allows for defining the probability of their occurrence as a proportion relative to the dike section they encompass. In this regard, EMI is a cost-effective method for the characterization of paleochannels, as this method can survey the length of a dike at walking speed or faster. If presence of a paleochannel scenario is discarded with EM exploration, the probability of such scenario can be reduced to virtually zero although not zero, as false negatives are physically possible. Further research is needed to characterize false negatives. The challenge of this type of research is the validation of the EM data against hard geological data and knowledge.

Chapter 4 demonstrates how ERT tomograms enable the estimation of the horizontal correlation structure of material properties. Traditional methods for determining the horizontal correlation length demand exhaustive subsurface sampling at closely spaced intervals, often just a few meters apart. However, this extensive sampling is unfeasible in geotechnical practice due to its substantial operational demands and the potential adverse impact on dike stability. By deriving the correlation structure with ERT, it becomes possible to reduce the uncertainty associated with the inherent variability of material properties (refer to Equation 4.10). The extent of this reduction depends not only on the correlation structure but also on the model used for stability calculations. In essence, this estimation minimizes uncertainty by allowing for a more accurate assessment of the effective distribution of strength properties.

5.3. RECOMMENDATIONS FOR FUTURE RESEARCH

The research carried out in this thesis makes it evident that EM methods are powerful and efficient tools to reduce uncertainties related to subsurface heterogeneity. While the study cases highlighted here demonstrate the capabilities of EM methods, they represent only a small sample of potential subsurface scenarios. The interpretation of geophysical tomograms can be challenging, often requiring collaboration among various experts, including geophysicists and geologists, to derive geotechnically meaningful insights. This limitation restricts the practical applicability of geophysical exploration in day-to-day geotechnical practice. To overcome this limitation, the next crucial step in geophysical research for dike exploration is the establishment of a comprehensive library of subsurface patterns alongside their corresponding geophysical tomograms. This ambitious endeavor demands ample test locations with extensive sample data and a deep understanding of sedimentary processes. Modeling studies, similar to the one presented in Chapter 2, are also essential to interpret the data quantitatively. By creating such a library, geotechnical practitioners can seamlessly incorporate geophysical data into the

early stages of design and assessment. Moreover, it would facilitate the adoption of data-driven methods to automate the interpretation of geological features from geophysical data. One potential challenge that may emerge in these modeling studies is the presence of topographic features, such as roads and water ditches.

The EM methods discussed in this research show certain limitations in terms of detection and imaging capabilities. Notably, tomographic inversion tends to smooth out fine subsurface features, potentially leaving hazardous subsurface elements undetected. For instance, undetected pockets of sand could reduce the stability of dikes due to increased pore-water pressures. From a physics perspective, wave-field methods emerge as the most powerful geophysical tool for mapping subsurface heterogeneity. The waveform itself carries rich information about the medium it traverses which could potentially offer unprecedented insights into subsurface heterogeneity. However, the scientific and technological challenge lies in developing acquisition systems and processing algorithms capable of distinguishing geologically-relevant information from coherent and environmental noise. Scientific and technological advancements in this direction would profoundly impact geotechnical practice. It would enable the detection of small and adverse subsurface features that are currently beyond the realm of possibility. Furthermore, it would facilitate the comprehensive characterization of both deep and shallow geological deposits in terms of internal variability.

5

REFERENCES

Archie, G.E. 1942. "The Electrical Resistivity Log as an Aid in Determining Some Reservoir Characteristics." *Transactions of the AIME* 146: 54–62. https://doi.org/10.2118/942054-G.

Aug, Christophe. 2004. "Modélisation géologique 3D et caractérisation des incertitudes par la méthode du champ de potentiel." 12.

Auken, Esben, and Anders Vest Christiansen. 2004. "Layered and laterally constrained 2D inversion of resistivity data." *GEOPHYSICS* 69: 752–761. https://doi.org/10.1190/1.1759461.

Berendsen, H. J.A., and K. P. Volleberg. 2007. "New prospects in geomorphological and geological mapping of the Rhine-Meuse delta - Application of detailed digital elevation maps based on laser altimetry." Vol. 86, 15–22. Stichting Netherlands Journal of Geosciences. https://doi.org/10.1017/S0016774600021296.

Berendsen, Henk J.A. 1982. "De genese van het landschap in het zuiden van de provincie Utrecht, een fysisch-geografische studie." .

Bierkens, M. F.P. 1994. "Complex confining layers: a stochastic analysis of hydraulic properties at various scales." 3.

Binley, Andrew, Susan S. Hubbard, Johan A. Huisman, André Revil, David A. Robinson, Kamini Singha, and Lee D. Slater. 2015. "The emergence of hydrogeophysics for improved understanding of subsurface processes over multiple scales." 6. https://doi.org/10.1002/2015WR017016.

Bishop, Alan W. 1955. "The use of the Slip Circle in the Stability Analysis of Slopes." *Géotechnique* 5: 7–17. https://doi.org/10.1680/geot.1955.5.1.7.

Boaga, Jacopo. 2017. "The use of FDEM in hydrogeophysics: A review." *Journal of Applied Geophysics* 139: 36–46. https://doi.org/10.1016/j.jappgeo.2017.02.011.

Campanella, R. G., and I. Weemees. 1990. "Development and use of an electrical resistivity cone for groundwater contamination studies." *Canadian Geotechnical Journal* 27: 557–567. https://doi.org/10.1139/t90-071.

CEN. 2004. "EN 1997-1:2004 Eurocode 7: geotechnical design – part 1: general rules." .

Chambers, J. E., P. B. Wilkinson, D. Wardrop, A. Hameed, I. Hill, C. Jeffrey, M. H. Loke, et al. 2012. "Bedrock detection beneath river terrace deposits using three-dimensional electrical resistivity tomography." *Geomorphology* 177-178: 17–25. https://doi.org/10.1016/j.geomorph.2012.03.034.

Chiles, J. P., C Aug, A Guillen, and T Lees. 2004. "Modelling the geometry of geological units and its uncertainty in 3D from structural data - The potential-field method." 355–362.

Constantine, Paul. 2020. "Random Field Simulation, MATLAB Central File Exchange." .

Daniel, Chris R., John A. Howie, Richard G. (Dick) Campanella, and Heraldo L. Giacheti. 1999. "The Resistivity Piezocone Penetration Test (RCPTU) for Quality Control of Geotechnical Ground Densification." 1, 133–142. Society of Exploration Geophysicists. https://doi.org/10.4133/1.2922599.

Day-Lewis, Frederick D. 2005. "Applying petrophysical models to radar travel time and electrical resistivity tomograms: Resolution-dependent limitations." *Journal of Geophysical Research* 110: B08206. https://doi.org/10.1029/2004JB003569.

Day-Lewis, Frederick D, Carole D Johnson, Kamini Singha, and John W Jr Lane. 2008. "Best practices in electrical resistivity imaging: Data collection and processing, and application to data from Corinna, Maine." .

Day-Lewis, Frederick D., John W. Lane, and Steven M. Gorelick. 2006. "Combined interpretation of radar, hydraulic, and tracer data from a fractured-rock aquifer near Mirror Lake, New Hampshire, USA." *Hydrogeology Journal* 14: 1–14. https://doi.org/10.1007/s10040-004-0372-y.

de Gast. 2020. "Dykes and Embankments: a Geostatistical Analysis of Soft Terrain." . https://doi.org/10.4233/uuid:4ce3b4ec-0a6a-4886-9a82-5945a1f9ea50.

de Gast, Tom, Michael A. Hicks, and Philip Vardon. 2020. "Cone Penetration Test (CPT) dataset to study soil heterogeneity." . https://doi.org/https://doi.org/10.4121/uuid:0a9b77bc-3f6d-40e2-846c-ddb992dd78a6.

de Pasquale, G, N Linde, J Doetsch, and W S Holbrook. 2019. "Probabilistic inference of subsurface heterogeneity and interface geometry using geophysical data." *Geophysical Journal International* 217: 816–831. https://doi.org/10.1093/gji/ggz055.

Delefortrie, Samuël, Daan Hanssens, Timothy Saey, Ellen Van De Vijver, Marthe Smetryns, Christin Bobe, and Philippe De Smedt. 2019. "Validating land-based FDEM data and derived conductivity maps: Assessment of signal calibration, signal attenuation and the impact of heterogeneity." *Journal of Applied Geophysics* 164: 179–190. https://doi.org/10.1016/j.jappgeo.2019.03.001.

Dezert, Théo, Yannick Fargier, Sérgio Palma Lopes, and Philippe Côte. 2019. "Geophysical and geotechnical methods for fluvial levee investigation: A review." *Engineering Geology* 260: 105206. https://doi.org/10.1016/j.enggeo.2019.105206.

ENW. 2012. "Technisch Rapport Grondmechanisch Schematiseren bij Dijken." .

Fauchard, Cyrille, and Patrice Mériaux. 2007. *Geophysical and Geotechnical Methods for Diagnosing Flood Protection Dikes*. éditions Quae. https://doi.org/10.35690/978-2-7592-0035-1.

Fenton, Gordon A, Farzaneh Naghibi, and D V Griffiths. 2016. "On a unified theory for reliability-based geotechnical design." *Computers and Geotechnics* 78: 110–122. https://doi.org/10.1016/j.compgeo.2016.04.013.

Frank, R, C Bauduin, R Driscoll, M Kavvadas, N Krebs Ovesen, T Orr, B Schuppener, and H Gulvanessian. 2004. *Designers' Guide to EN 1997-1 Eurocode 7: Geotechnical Design - General Rules.* Thomas Telford Ltd. https://doi.org/10.1680/dgte7.31548.

Friedel, Sven. 2003. "Resolution, stability and efficiency of resistivity tomography estimated from a generalized inverse approach." *Geophysical Journal International* 153: 305–316. https://doi.org/10.1046/j.1365-246X.2003.01890.x.

Gast, Tom De, Philip J. Vardon, and Michael A. Hicks. 2021. "Assessment of soil spatial variability for linear infrastructure using cone penetration tests." *Geotechnique* 71: 999–1013. https://doi.org/10.1680/jgeot.19.SiP.002.

Goovaerts, Pierre. 1997. *Geostatistics for Natural Resources and Evaluation.* Oxford University Press.

Griffiths, D. V., and P. A. Lane. 1999. "Slope stability analysis by finite elements." *Géotechnique* 49: 387–403. https://doi.org/10.1680/geot.1999.49.3.387.

Günther, Thomas, Carsten Rücker, and Klaus Spitzer. 2006a. "Three-dimensional modelling and inversion of dc resistivity data incorporating topography - II. Inversion." *Geophysical Journal International* 166: 506–517. https://doi.org/10.1111/j.1365-246X.2006.03011.x.

Günther, Thomas, Carsten Rücker, and Klaus Spitzer. 2006b. "Three-dimensional modelling and inversion of dc resistivity data incorporating topography - II. Inversion." *Geophysical Journal International* 166: 506–517. https://doi.org/10.1111/j.1365-246X.2006.03011.x.

Hansen, Thomas M, Majken C Looms, and Lars Nielsen. 2008. "Inferring the Subsurface Structural Covariance Model Using Cross-Borehole Ground Penetrating Radar Tomography." *Vadose Zone Journal* 7: 249–262. https://doi.org/10.2136/vzj2006.0144.

Hermans, Thomas, and James Irving. 2017. "Facies discrimination with electrical resistivity tomography using a probabilistic methodology: effect of sensitivity and regularisation." *Near Surface Geophysics* 15: 13–25. https://doi.org/10.3997/1873-0604.2016047.

Hermans, Thomas, Alexander Vandenbohede, Luc Lebbe, Roland Martin, Andreas Kemna, Jean Beaujean, and Frederic Nguyen. 2012. "Imaging artificial salt water infiltration using electrical resistivity tomography constrained by geostatistical data." *Journal of Hydrology* 438-439: 168–180. https://doi.org/10.1016/j.jhydrol.2012.03.021.

Hickey, Craig J., Mathias J. M. Römkens, Robert R. Wells, and Leti Wodajo. 2015. "Geophysical Methods for the Assessment of Earthen Dams." . https://doi.org/10.1007/978-3-319-11023-3_7.

Hicks, M. A., and W. A. Spencer. 2010. "Influence of heterogeneity on the reliability and failure of a long 3D slope." *Computers and Geotechnics* 37: 948–955. https://doi.org/10.1016/j.compgeo.2010.08.001.

Hicks, M.A. 2013. "An Explanation of Characteristic Values of Soil Properties in Eurocode 7." . https://doi.org/10.3233/978-1-61499-163-2-36.

Hicks, Michael, Federico Pisano, and Joek Peuchen. 2018. *Cone Penetration Testing IV*. CRC Press. https://doi.org/10.1201/9780429505980.

Hicks, Michael A., Divya Varkey, Abraham P. van den Eijnden, Tom de Gast, and Philip J. Vardon. 2019. "On characteristic values and the reliability-based assessment of dykes." *Georisk* 13: 313–319. https://doi.org/10.1080/17499518.2019.1652918.

Hijma, M. P., and K. M. Cohen. 2011. "Holocene transgression of the Rhine river mouth area, The Netherlands/Southern North Sea: palaeogeography and sequence stratigraphy." *Sedimentology* 58: 1453–1485. https://doi.org/10.1111/j.1365-3091.2010.01222.x.

Hijma, M.P., and K.S. Lam. 2015. "Globale stochastische ondergrondschematisatie (WTI-SOS) voor de primaire waterkeringen." .

Hsu, Han-Lun, Brian J. Yanites, Chien chih Chen, and Yue-Gau Chen. 2010. "Bedrock detection using 2D electrical resistivity imaging along the Peikang River, central Taiwan." *Geomorphology* 114: 406–414. https://doi.org/10.1016/j.geomorph.2009.08.004.

Huang, Haoping. 2005. "Depth of investigation for small broadband electromagnetic sensors." *Geophysics* 70. https://doi.org/10.1190/1.2122412.

Huang, Haoping, and I. J. Won. 2000. "Conductivity and Susceptibility Mapping Using Broadband Electromagnetic Sensors." *Journal of Environmental and Engineering Geophysics* 5: 31–41. https://doi.org/10.4133/jeeg5.4.31.

Hubbard, Susan S., Yoram Rubin, and Ernie Majer. 1999. "Spatial correlation structure estimation using geophysical and hydrogeological data." *Water Resources Research* 35: 1809–1825. https://doi.org/10.1029/1999WR900040.

Inazaki, Tomio. 2007. "Integrated geophysical investigation for the vulnerability assessment of earthen levee." Vol. 1, 90–97. https://doi.org/10.4133/1.2924605.

IPCC. 2014. "Climate Change 2014: Synthesis Report. Contribution of Working Groups I, II and III to the Fifth Assessment Report of the Intergovernmental Panel on Climate Change." .

Irving, James, Rosemary Knight, and Klaus Holliger. 2009. "Estimation of the lateral correlation structure of subsurface water content from surface-based ground-penetrating radar reflection images." *Water Resources Research* 45. https://doi.org/10.1029/2008WR007471.

Jongejan, Ruben, Matthijs Kok, and Ilka Tanckzos. 2017. "Fundamentals of Flood Protection." 4.

Journel, A. G. 1999. "Markov Models for Cross-Covariances." *Mathematical Geology* 31: 955–964. https://doi.org/10.1023/A:1007553013388.

5

Kanning, W. 2012. "The Weakest Link: Spatial Variability in the Piping Failure Mechanism of Dikes." 1. https://doi.org/10.4233/uuid:5fb7b121-dc00-48aa-bda2-b163f10513bf.

Kemna, Andreas, Andrew Binley, Giorgio Cassiani, Ernst Niederleithinger, André Revil, Lee Slater, Kenneth H. Williams, et al. 2012. "An overview of the spectral induced polarization method for near-surface applications." Vol. 10, 12, 453–468. EAGE Publishing BV. https://doi.org/10.3997/1873-0604.2012027.

Koelewijn, André R, Gijs J C M Hoffmans, and Meindert A Van. 2004. "Lessons Learned from a Full-Scale Dyke Failure Test." Vol. 33. University of Missouri–Rolla.

Kok, Matthijs, Juliette Cortes Arevalo, and Martijn Vos. 2022. *Towards Improved Flood Defences.* TU Delft OPEN. https://doi.org/10.34641/MG.31.

Kruse, G., and M. Hijma. 2015. "Handleiding lokaal schematiseren met WTI-SOS." .

Lajaunie, Christian, Gabriel Courrioux, and Laurent Manuel. 1997. "Foliation fields and 3D cartography in geology: Principles of a method based on potential interpolation." *Mathematical Geology* 29: 571–584. https://doi.org/10.1007/bf02775087.

Lavoué, F., J. Van Der Kruk, J. Rings, F. André, D. Moghadas, J. A. Huisman, S. Lambot, LWeihermüller, J. Vanderborght, and H. Vereecken. 2010. "Electromagnetic induction calibration using apparent electrical conductivity modelling based on electrical resistivity tomography." *Near Surface Geophysics* 8: 553–561. https://doi.org/10.3997/1873-0604.2010037.

Lesmes, David P., and Shmulik P. Friedman. 2005. "Relationships between the Electrical and Hydrogeological Properties of Rocks and Soils." . https://doi.org/10.1007/1-4020-3102-5_4.

Lloret-Cabot, M., G. A. Fenton, and M. A. Hicks. 2014. "On the estimation of scale of fluctuation in geostatistics." *Georisk* 8: 129–140. https://doi.org/10.1080/17499518.2013.871189.

Loke, M. H. 1995. "Least-squares deconvolution of apparent resistivity pseudosections." *Geophysics* 60: 1682. https://doi.org/10.1190/1.1443900.

Loke, M H. 2013. "Tutorial : 2-D and 3-D electrical imaging surveys." *Geotomo Software Malaysia* 127.

Looms, Majken C., Thomas M. Hansen, Knud S. Cordua, Lars Nielsen, Karsten H. Jensen, and Andrew Binley. 2010. "Geostatistical inference using crosshole ground-penetrating radar." *Geophysics* 75. https://doi.org/10.1190/1.3496001.

Menke, William. 2012. "Applications of Inverse Theory to Solid Earth Geophysics." . https://doi.org/10.1016/B978-0-12-397160-9.00013-8.

Menke, William. 2018. *Geophysical Data Analysis: Discrete Inverse Theory*. 4th ed. Elsevier. https://doi.org/10.1016/C2016-0-05203-8.

MinIM. 2016. "Achtergronden bij de normering van de primaire waterkeringen in Nederland. Hoofdrapport." .

Minsley, Burke J., Bruce D. Smith, Richard Hammack, James I. Sams, and Garret Veloski. 2012. "Calibration and filtering strategies for frequency domain electromagnetic data." *Journal of Applied Geophysics* 80: 56–66. https://doi.org/10.1016/j.jappgeo.2012.01.008.

Mlsna, Phillip A., and Jeffrey J. Rodríguez. 2009. "Gradient and Laplacian Edge Detection." 1. https://doi.org/10.1016/B978-0-12-374457-9.00019-6.

Mulder, Wim A. 2006. "A multigrid solver for 3D electromagnetic diffusion." *Geophysical Prospecting* 54: 633–649. https://doi.org/10.1111/j.1365-2478.2006.00558.x.

Nie, Xinyao, Hong wei Huang, Z Q Liu, and Suzanne Lacasse. 2015. "Scale of Fluctuation for Geotechnical Probabilistic Analysis." 816–821. https://doi.org/10.3233/978-1-61499-580-7-834.

Niederleithinger, E. 2015. "3G - Geophysical Methods Delivering Input to Geostatistical Methods for Geotechnical Site Characterization." 889–897. IOS Press BV. https://doi.org/10.3233/978-1-61499-580-7-889.

Niederleithinger, Ernst, Andreas Weller, and Ronald Lewis. 2012. "Evaluation of Geophysical Techniques for Dike Inspection." *Journal of Environmental and Engineering Geophysics* 17: 185–195. https://doi.org/10.2113/jeeg17.4.185.

Olalla, J. Chavez, T. G. Winkels, D. J.M. Ngan-Tillard, and T. J. Heimovaara. 2021. "Geophysical tomography as a tool to estimate the geometry of soil layers: relevance for the reliability assessment of dikes." *Georisk* . https://doi.org/10.1080/17499518.2021.1971252.

Olalla, Juan Chavez. 2022. "Data set for journal paper "Horizontal correlation structure of geotechnical properties from surface-based geophysical tomograms"." . https://doi.org/10.4121/17710832.

Orr, Trevor L.L. 2017. "Defining and selecting characteristic values of geotechnical parameters for designs to Eurocode 7." *Georisk* 11: 103–115. https://doi.org/10.1080/17499518.2016.1235711.

Prästings, Anders, Johan Spross, and Stefan Larsson. 2019. "Characteristic values of geotechnical parameters in Eurocode 7." *Proceedings of the Institution of Civil Engineers: Geotechnical Engineering* 172: 301–311. https://doi.org/10.1680/jgeen.18.00057.

Revil, André, Magnus Skold, Susan S. Hubbard, Yuxin Wu, David B. Watson, and Marios Karaouli. 2013. "Petrophysical properties of saprolites from the Oak Ridge Integrated Field Research Challenge site, Tennessee." *Geophysics* 78: D21–D40. https://doi.org/10.1190/GEO2012-0176.1.

5

Rijkswaterstaat. 2015. "The national flood risk analysis for the Netherlands." *Rijkswaterstaat VNK Project Office* .

Robertson, P. K. 2009. "Interpretation of cone penetration tests - A unified approach." *Canadian Geotechnical Journal* 46: 1337–1355. https://doi.org/10.1139/T09-065.

Rodgers, Joseph Lee, and Wander Alan Nice. 1988. "Thirteen ways to look at the correlation coefficient." *American Statistician* 42: 59–66. https://doi.org/10.1080/00031305.1988.10475524.

Royet, P., S. Palma Lopes, C. Fauchard, P. Mériaux, and L. Auriau. 2013. "Rapid and cost-effective dike condition assessment methods: geophysics and remote sensing." .

Rubin, Yoram, Gary Mavko, and Jerry Harris. 1992. "Mapping permeability in heterogeneous aquifers using hydrologic and seismic data." *Water Resources Research* 28: 1809–1816. https://doi.org/10.1029/92WR00154.

Ruggeri, Paolo, James Irving, Erwan Gloaguen, and Klaus Holliger. 2013. "Regional-scale integration of multiresolution hydrological and geophysical data using a two-step Bayesian sequential simulation approach." *Geophysical Journal International* 194: 289–303. https://doi.org/10.1093/gji/ggt067.

Rücker, Carsten, Thomas Günther, and Klaus Spitzer. 2006. "Three-dimensional modelling and inversion of dc resistivity data incorporating topography - I. Modelling." *Geophysical Journal International* 166: 495–505. https://doi.org/10.1111/j.1365-246X.2006.03010.x.

Santos, Fernando Acácio Monteiro, John Triantafilis, and Kira Bruzgulis. 2011. "A spatially constrained 1D inversion algorithm for quasi-3D conductivity imaging: Application to DUALEM-421 data collected in a riverine plain." *Geophysics* 76. https://doi.org/10.1190/1.3537834.

Schon, Jurgen T A T T. 2015. *Physical properties of rocks : fundamentals and principles of petrophysics*. Nv - 1 onl ed. Elsevier.

Schön, Jürgen H. 2015. "Physical properties of rocks." . https://doi.org/10.1017/CBO9781107415324.004.

Sellmeijer, Hans, Juliana López de la Cruz, Vera M. van Beek, and Han Knoeff. 2011. "Fine-tuning of the backward erosion piping model through small-scale, medium-scale and IJkdijk experiments." *European Journal of Environmental and Civil Engineering* 15: 1139–1154. https://doi.org/10.1080/19648189.2011.9714845.

Sellmeijer, J. B. 1988. "On the mechanism of piping under impervious structures." .

Sellmeijer, J.B., and M.A. Koenders. 1991. "A mathematical model for piping." *Applied Mathematical Modelling* 15: 646–651. https://doi.org/10.1016/S0307-904X(09)81011-1.

Shmaryan, L. E., and A. G. Journel. 1999. "Two Markov Models and Their Application." *Mathematical Geology* 31: 965–988. https://doi.org/10.1023/A:1007505130226.

Singha, K, F D Day-Lewis, T Johnson, and L D Slater. 2015. "Advances in interpretation of subsurface processes with time-lapse electrical imaging." *Hydrological Processes* 29: 1549–1576. https://doi.org/10.1002/hyp.10280.

Smith, I. M., D. V. Griffiths, and M. Lee. 2014. *Programming the finite element method.* 5th ed. John Wiley & Sons.

Spencer, E. 1967. "A Method of analysis of the Stability of Embankments Assuming Parallel Inter-Slice Forces." *Géotechnique* 17: 11–26. https://doi.org/10.1680/geot.1967.17.1.11.

Stafleu, J., D. Maljers, J.L. Gunnink, A. Menkovic, and F.S. Busschers. 2011. "3D modelling of the shallow subsurface of Zeeland, the Netherlands." *Netherlands Journal of Geosciences - Geologie en Mijnbouw* 90: 293–310. https://doi.org/10.1017/S0016774600000597.

Stummer, Peter, Hansruedi Maurer, and Alan G Green. 2004. "Experimental design: Electrical resistivity data sets that provide optimum subsurface information." *GEOPHYSICS* 69: 120–139. https://doi.org/10.1190/1.1649381.

UNFCCC. 1997. "Kyoto Protocol to the United Nations Framework Convention on Climate Change." *Kyoto Climate Change Conference* 24.

UNFCCC. 2015. "Paris Agreement, United Nations Framework Convention on Climate Change." *21st Conference of the Parties* 25.

Van, M. A., A. R. Koelewijn, and F. B. Barends. 2005. "Uplift Phenomenon: Model, Validation, and Design." *International Journal of Geomechanics* 5: 98–106. https://doi.org/10.1061/(ASCE)1532-3641(2005)5:2(98).

van der Meulen, M.J., J.C. Doornenbal, J.L. Gunnink, J. Stafleu, J. Schokker, R.W. Vernes, F.C. van Geer, et al. 2013. "3D geology in a 2D country: perspectives for geological surveying in the Netherlands." *Netherlands Journal of Geosciences - Geologie en Mijnbouw* 92: 217–241. https://doi.org/10.1017/S0016774600000184.

Vanmarcke, Erik. 1983. *Random fields, analysis and synthesis.* MIT Press.

Varga, Miguel De La, Alexander Schaaf, and Florian Wellmann. 2019. "GemPy 1.0: Open-source stochastic geological modeling and inversion." *Geoscientific Model Development* 12: 1–32. https://doi.org/10.5194/gmd-12-1-2019.

Varkey, D., M. A. Hicks, A. P. Van Den Eijnden, and P. J. Vardon. 2020. "On characteristic values for calculating factors of safety for dyke stability." *Geotechnique Letters* 10: 353–359. https://doi.org/10.1680/jgele.19.00034.

Veerman, C.P., and M.J. Stive. 2008. "Working together with water: A living land builds for its future." .

5

Waal, Hans De. 2018. "Basisrapport WBI 2017." .

Wackernagel, Hans. 2003. *Multivariate geostatistics : an introduction with applications.* 3rd ed. Springer.

Wait, James R. 1982. *Geo-electromagnetism.* Academic Press. https://doi.org/10.1016/b978-0-12-730880-7.x5001-7.

Ward, Stanley H., and Gerald W. Hohmann. 1988. "4. Electromagnetic Theory for Geophysical Applications." 1. https://doi.org/10.1190/1.9781560802631.ch4.

Water, Helpdesk. 2017. "Beoordelingsinstrumentarium (WBI2017)." .

Weerts, H. J.T. 1996. "Complex confining layers. Architecture and hydraulic properties of Holocene and late Weichselian deposits in the fluvial Rhine-Meuse Delta, the Netherlands." .

Weller, Andreas, Lee Slater, and Sven Nordsiek. 2013. "On the relationship between induced polarization and surface conductivity: Implications for petrophysical interpretation of electrical measurements." *GEOPHYSICS* 78: D315–D325. https://doi.org/10.1190/geo2013-0076.1.

Werthmüller, Dieter, Wim Mulder, and Evert Slob. 2019. "emg3d: A multigrid solver for 3D electromagnetic diffusion." *Journal of Open Source Software* 4: 1463. https://doi.org/10.21105/JOSS.01463.

Winkels, T.G., K.M. Cohen, S.M. Knaake, H. Middelkoop, and E. Stouthamer. 2021. "Geological framework for assessing variability in subsurface piping parameters underneath dikes in the Rhine-Meuse delta, the Netherlands." *Engineering Geology* 294: 106362. https://doi.org/10.1016/j.enggeo.2021.106362.

Zhdanov, Michael S (Mikhail Semenovich), and George V (George Vernon) Keller. 1994. *The geoelectrical methods in geophysical exploration.* Elsevier.

Zhou, J., S. Laumann, and T.J. Heimovaara. 2019. "Applying aluminum-organic matter precipitates to reduce soil permeability in-situ: A field and modeling study." *Science of The Total Environment* 662: 99–109. https://doi.org/10.1016/j.scitotenv.2019.01.109.

CURRICULUM VITÆ

Juan CHAVEZ OLALLA

09-03-1991   Born in Quito, Ecuador.

EDUCATION

2017–2023   PhD. Geoscience
                 Delft University of Technology
                 Thesis: Electromagnetic Exploration Inputs for the Geotech-
                                  nical Schematization of Dikes
                 Promotor: Prof. dr. T.J. Heimovaara

2015–2017   MSc. in Geo-Engineering
                 Delft Univerity of Technology

2008–2014   BSc. in Civil Engineering
                 National Polytechnic School of Ecuador

ACKNOWLEDGEMENTS

LIST OF PUBLICATIONS

1. **Chavez Olalla, J., Winkels, T.G., Ngan-Tillard, D.J.M., Heimovaara, T.J.**, *Geophysical tomography as a tool to estimate the geometry of soil layers: relevance for the reliability assessment of dikes,* Georisk: Assessment and Management of Risk for Engineered Systems and Geohazards **18**, 639 (2021).